Modeling friction and wear using an adaptive discrete-continuum coupling

Acknowledgement of Support

Acknowledgements

I would like to express my sincere gratitude to my supervisor Prof. Jean-François Molinari for his constant support and for always ensuring a positive atmosphere within the laboratory. I am also grateful to my co-supervisor, Dr. Guillaume Anciaux, for his invaluable guidance throughout my Ph.D. journey. I was fortunate to have two supervisors whose expertise complemented each other, enriching my experience. I am thankful Dr. Joaquin Garcia-Suarez, who has always been available to help. I also want to thank the members of my thesis committee, Prof. Marie Violay, Prof. Brice Lecampion, Prof. Ken Kamrin, and Dr. Guilhem Mollon, for reviewing my work and for the stimulating discussions during the oral examination.

I would also like to thank every member of the LSMS laboratory for the wonderful moments we shared together, particularly during our lunch conversations. Finally, I want to thank my family and friends for their constant support, with special gratitude to my mum and my partner.

Abstract

When two objects slide against each other, wear and friction occur at their interface. The accumulation of wear forms what is commonly referred to as a "third-body". Understanding third-body evolution has significant applications in industry, where controlling and measuring friction and wear is essential, notably to minimize energy losses. In the geomechanics community, the granular material localized in a fault, is known as "gouge" and understanding its frictional properties is crucial in the study of earthquake nucleation. The goal of this thesis is to develop a numerical tool that models the third-body and its surrounding regions to improve our understanding of its evolution.

The third-body is a localized amorphous region subject to severe deformation, while the regions surrounding the third-body, experience moderate strain and damage. We showed that the loading conditions applied on the surrounding regions and their distance from the contact interface have an impact on the third-body thickness evolution and frictional properties. Thus, to accurately capture the third-body behavior the surrounding regions should be represented which requires modeling large domains. To do so, a multiscale approach is developed in this thesis. The Discrete Element Method (DEM) is used to model the third-body where discretization is required, while the Finite Element Method (FEM) is utilized to model the surrounding regions, as continuum domains. In our model, both the FEM and DEM represent the same material.

To couple FEM and DEM, we generalized the *bridging* method [97] originally used for regular lattices, to amorphous materials. This approach considers an overlapping region, where both continuum and discrete domain are linked by means of Lagrange multipliers. Two different types of formulations are considered: strong and weak. To test this approach, we considered a granular system without any cohesion, subject to confinement pressure. Several DEM sample sizes are tested to establish the minimum sample size at which constant elastic properties are obtained. This determines the material properties to use in the FEM and the minimum mesh size needed at the FEM/DEM interface to match material properties across both domains. The imposed pre-stress of the FE elements results in spurious forces, that we corrected. Then, this coupling method is used to model crack propagation and wear formation using an adhesive contact law.

To facilitate the growth of the third-body without being restricted by the finite size of the discrete domain, we implemented an adaptive coupling strategy. This strategy enables regions modeled with FEM to transition to discrete regions, thereby increasing

the size of the discrete domain. The discrete expansion occurs if a criterion based on the average change of neighbors for each particle is satisfied. Implementing this approach requires several steps: first, adjusting coupling geometries, then, inserting a new particle layer, and finally, deactivating a FE element layer. The efficacy of this approach is demonstrated for both amorphous system, and a crystalline one. Lastly, we used this method to model the evolution of a third-body involving the insertion of elliptical rigid bodies at the contact interface.

Résumé

Lorsque deux objets sont frottés l'un contre l'autre, des débris peuvent se former à l'interface de contact. Cette accumulation de débris est désignée sous le terme de "troisième corps". Comprendre l'évolution de ce troisième corps présente un intérêt certain dans l'industrie, où il est important de mesurer et controler le frottement et l'usure, notamment dans l'objectif de réduire les pertes d'énergie. En géomécanique, le milieu granulaire situé à l'interface d'une faille, appelé "gouge", joue un rôle significatif dans la compréhension de la friction lors des séismes. L'objectif de cette thèse est de développer un model numérique qui représente le troisième corps et ses régions environnantes afin d'améliorer notre compréhension de son comportement.

Le troisième corps est une matière amorphe, localisée et sujette à des déformations non uniformes, tandis que les régions qui l'entourent sont sujettes à des déformations uniformes. Dans une première partie de cette thèse, nous avons démontré que la distance des conditions limites à l'interface influence l'évolution frictionnelle du troisième corps. Ainsi, pour capturer avec précision le comportement du troisième corps il est important de représenter les régions environnantes ce qui nécessite de modéliser des systèmes larges. Pour ce faire, une approche multi-échelle est implémentée : la méthode des éléments discrets (DEM) est utilisée pour modéliser le troisième corps, tandis que la méthode des éléments finis (FEM) est employée pour les régions environnantes. Dans notre étude, la FEM et la DEM représentent le même matériau.

Pour le couplage entre la FEM et la DEM, nous avons généralisé la méthode *bridging* [97], conçue à l'origine pour des réseaux cristallins, aux matériaux amorphes et granulaires. Deux types de formulations pour le couplage ont été considérés : une forme forte et une forme faible. Afin de tester cette approche, nous avons considéré un milieu granulaire sans cohésion et soumis à une pression externe. Plusieurs échantillons de DEM ont été testés pour déterminer leurs propriétés élastiques et la taille d'échantillon à partir de laquelle nous obtenons des propriétés constantes. Cela permet de définir les propriétés du milieu continu et la taille minimale de maillage nécessaire pour modéliser le même matériau dans les deux domaines. Le couplage est validé par des tests de propagation d'ondes compressives et de cisaillements. Cette méthode est ensuite utilisée pour simuler la propagation de fissures et la formation de débris en utilisant des particules cohésives.

Afin de permettre l'évolution naturelle du troisième corps, indépendamment des ré-

gions continues, nous avons développé un couplage adaptatif. Cette méthode permet d'étendre dynamiquement la région discrète en fonction des variations de voisinage des particules. Lorsque le critère est satisfait, une région initialement continue devient discrète, un processus qui se déroule en trois étapes : d'abord l'ajustement des régions de couplage, ensuite l'ajout de nouvelles particules, et finalement, la désactivation d'une couche d'éléments discrets. Cette méthode a été testée pour un milieu discret/amorphe, mais aussi avec une lattice régulière. Enfin, nous avons utilisé cette méthode pour modéliser l'évolution d'un troisième corps, impliquant l'insertion de corps rigides elliptiques à l'interface de contact.

Mots clés: troisième corps, gouge, amorphe, multi-échelle, méthode des éléments discrets, méthode des éléments finis, couplage adaptatif

Contents

CONTENTS

CONTENTS

12

List of Figures

16

18

LIST OF FIGURES

List of Tables

LIST OF TABLES

Chapter 1

Introduction

1.1 Motivation

Wear and friction are ubiquitous to everyday life and many industrial processes. In some cases, they need to be minimized to improve reliability, prolong lifespan, and minimize energy losses, such as for gears or bearings. However, there are also instances where systems intentionally use friction and wear to their advantage, as seen in brakes requiring high friction, machining relying on wear formation, or even a lighter benefiting from both friction and wear. The science of interacting surfaces in relative motion, and their relative phenomena such as friction, wear, and lubrication is called *tribology*. Investigations [52, 59] have shown that developments in tribology could lead to a saving of the UK gross national product between 1.3% to 1.6%. While energy losses impact economic costs, they also contribute to environmental concerns through CO2 emissions, becoming an urgent matter. Holmberg and Erdemir [52] state that advancements in tribology could lead to a worldwide reduction of global CO_2 emissions by 1,460 $MtCO_2$ in the short term (8 years) and 3,140 $MtCO_2$ in the long term (15 years). For context, the CO_2 emissions of the EU in 2010 were approximately 4,000 $MtCO_2$ [28].

The first documented study of friction was conducted by Leonardo da Vinci, who discovered through his experiments that the frictional force F_t between two bodies in contact is proportional to the normal force F_n, and is independent of the apparent contact area [53]. Later, Amontons [9] and Coulomb [31] formulated this relationship as $F_t = \mu F_n$, introducing the concept of the coefficient of friction μ. Two coefficients of friction are distinguished: the static coefficient of friction and the dynamic one. The static coefficient is the ratio F_t/F_n required to initiate a motion between two bodies, while the dynamic coefficient is the ratio F_t/F_n when the two bodies are in motion. The fact that the friction coefficient is independent of the apparent, or nominal, contact area remained a mystery for centuries, which was solved by Bowden and Tabor [21]. They demonstrated that the key factor for determining friction is the real contact area between two solids, which is only a small portion of the apparent contact area, due to the roughness of surfaces. The real contact area is made of a the assembly of micro-

contacts, at places where protruding asperities make junctions. While these theories are effective in many engineering cases, they do not capture ageing mechanisms and the complex transient dynamics of frictional systems that appear for instance during stick-slip events. Slip weakening friction was introduced to better describe the non-instantaneous transition from static to dynamic friction over a critical slip distance [54, 79]. In its simplest form, the coefficient of friction linearly weakens from a static to a dynamic state as function of slip. Then, rate-and-state friction laws were introduced to bring a dependency on slip rate of the friction coefficient, which could be either velocity weakening or velocity strengthening, and a dependency on state, via a state parameter representing the age of micro-contacts that captures the logarithmic ageing of the static friction coefficient with time [35, 37, 38, 62, 82]. Rate-and-state friction laws are not only popular in the geomechanics community but also find applications in engineering [96].

We now shift our focus to wear. Archard was one of the first to explain the wear process [15]. He stated that the volume of the detached material is proportional to the product of the normal force and the sliding distance over the material's hardness. The value of the coefficient of proportionality is specific to every setup, and should be determined experimentally. Rabinowicz [78] reported that wear coefficient values vary from 10^{-2} to 10^{-9}, and are influenced by the wear type. He distinguished two principal forms: adhesive wear, happening between materials of similar hardness, and abrasive wear, occurring between surfaces of differing hardness. The empirical determination of the coefficient of proportionality makes the application of such laws non-trivial. A limitation of Archard's law is that it assumes newly created particles disappear from the contact area. However, it has been demonstrated that when two objects slide against each other, an interfacial layer can form at the interface, due to the accumulation of wear debris. This interfacial layer is referred to as the third-body, while the original contacting objects are termed the first bodies. The concept of the third-body was first introduced by Godet [48, 49]. Notably, Godet [49] showed that friction is influenced by the third-body. The concept of third-body is similar to the gouge in geomechanics. Experimental Studies have demonstrated that the gouge influences the triggering and amplitude of seismic events [66]. Hence, understanding the evolution of the third-body is crucial across different scales, from the micron scale of a mechanical actuator in a engineering application to the large scale of an earthquake occurring along a fault.

While the existence of the third-body is evident in many cases [18, 48, 49], its evolution and behavior are still not fully understood. Pham-Ba and Molinari [74] conducted pin-on-disc experiments to investigate the development of a third-body, as depicted in Figure 1.1. This figure illustrates the chronological sequence of wear debris formation on the flat discs: initial particle formation (a), accumulation into cylinders (b), and agglomeration into larger particles forming a third-body (c). Panels (d) and (e) provide a closer view of the third-body, while panel (f) depicts wear debris that fell outside the wear track. These experiments demonstrate the complexity behind the wear formation

and the amorphous nature of the third-body that is formed.

(a) 1s: formation of first wear particles

(b) 30s: cylinders and aggregates

(c) 1h: large flakes on the disc forming the wear track

(d) 1h: detail: aggregates forming a large flake

(e) 1h: detail: cylinders and aggregates on top of a flake

(f) 1h: detail: aggregated wear particle fallen outside the wear track
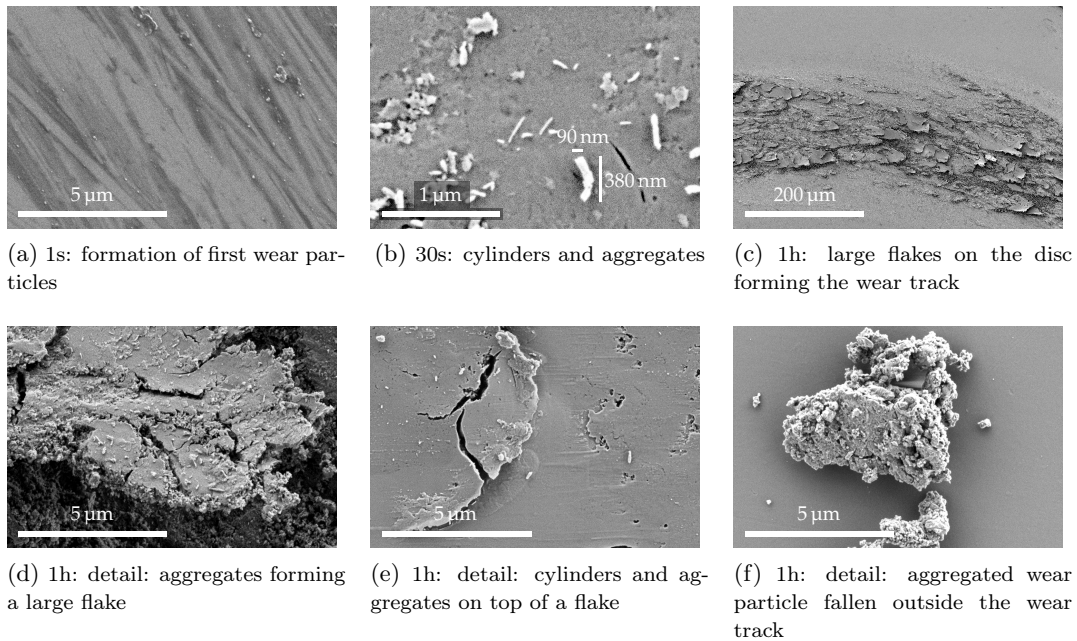
Figure 1.1: Third-body evolution in pin-on-disc experiments. Image taken from [74], with authors' permission.

Dieterich [36] compared experiments considering a gouge and planar surfaces, from which the rate and state friction law is derived. It was demonstrated that the displacement required to achieve a stable strength is greater for gouge than for planar surfaces, influenced by both particle sizes and surface roughness. Moreover, they demonstrated a localized deformation in the gouge. Biegel et al. [19] experimentally studied the frictional properties of Westerly granite gouge, demonstrating that particle size distribution affects the coefficient of friction, especially on rough surfaces. Additionally, they explored two gouge sizes, finding that the smaller gouge exhibited a higher coefficient of friction. These experimental results demonstrate how gouge properties significantly impact the coefficient of friction.

The third-body/gouge, being an amorphous material, is commonly modeled using the Discrete Element Method (DEM), which was initially developed by Cundall and Strack [32] for modeling granular materials. This method has been applied in both geomechanics [1, 43, 46, 77, 93] and in engineering contexts [55, 75]. Other approaches, such as the multibody meshfree method, can model the third-body with grain deformation [70, 102], but at a higher computational cost compared to DEM. While these models offer valuable insights into the third-body evolution, they are generally conducted on relatively small DEM systems, focusing solely on the third-body. The representation of the first bodies is limited to a thin layer of particles at the border of the third-

body. However, the characteristics of the first body, including its deformation and its thickness, may significantly influence the formation of the third-body. Therefore, these aspects should be accurately represented to achieve a more realistic model.

1.2 Objectives

The main objective of this thesis is to develop a numerical tool to gain a better understanding of the third-body evolution, by modeling both the third-body and its surrounding regions (first bodies). In this thesis, we will use the term third-body interchangeably with gouge.

The third-body will be modeled using the DEM, as it is commonly used to model the third-body/gouge, as previously described. The first part of this thesis aims to evaluate the impact of the surrounding regions on the third-body evolution.

- **Understand the impact of the surrounding regions**: How does the thickness of the surrounding regions impact the third-body frictional properties?

Due to the high computational cost associated with DEM, modeling the third-body and surrounding regions exclusively with DEM is computationally expensive. Thus, a multiscale approach is necessary, allowing DEM to model the third-body evolution where discretization is essential, while the Finite Element Method (FEM) can be employed in the surrounding regions to model the continuum domain subject only to linear deformation. The coupling method used is the *bridging* method [97], originally derived to couple Molecular Dynamics (MD) with FEM, which we have expanded to amorphous materials. While such FEM-DEM coupling method offers a reduction in computational cost, it still has a limitation. The evolution of the third-body, in fact, is constrained by the size of the discrete domain. To address this challenge, an adaptive coupling approach, which expands the discrete domain based on a physical criterion, will be employed. This adaptive bridging coupling approach raises several concerns:

- **Multiscale approach**: How can material properties be matched between FEM and DEM, given the amorphous nature of the third-body? Which coupling formulation is most appropriate? Is this coupling method effective for discontinuous events, including crack propagation, and wear debris formation?

- **Adaptive approach**: What criterion should be used to determine when to extend the discrete region? Can this approach capture complex gouge evolution and lead to new insights regarding friction?

1.3 Outline

The thesis manuscript is structured into seven chapters, briefly described:

- **Chapter 2: Numerical methods**

In this chapter, a state-of-the-art review of the numerical methods is provided. The discrete element method, along with the contact laws that will be employed in this thesis, are described. Different coupling approaches, including the one used in this thesis, are also reviewed.

- **Chapter 3: Boundary conditions impact on the third-body evolution**

In this chapter, the impact of boundary conditions and the domain size on the third-body is studied, showing the importance of proper boundary conditions. This study is conducted with a pure DEM system.

- **Chapter 4: Bridging coupling: application to amorphous materials**

In this chapter, we extend the bridging method, originally developed for MD/FEM coupling, to DEM/FEM. No adhesion between particles are considered, and a confinement pressure is applied. Initial tests on the DEM are conducted to identify its effective elastic properties and determine the minimum size of DEM for consistent elastic behavior. The coupling is implemented using the bridging method, exploring both weak and strong formulations. The impact of the confining pressure in the FEM, leading to ghost forces, is also investigated. To validate the coupling, transmission tests with small-amplitude waves are performed. We demonstrate that the strong coupling, incorporating a force subtraction at the interface to mitigate ghost forces, is the best coupling option for this application.

- **Chapter 5: Two-scale concurrent simulations for crack propagation using FEM-DEM bridging coupling**

In this chapter, we utilize the FEM-DEM bridging coupling described earlier to model crack propagation and wear formation. A DEM contact law that takes into account the attachment and reattachment of particles is employed. We validate the ability of the coupling to model crack propagation and wear formation, by comparing the coupled simulations with pure DEM simulations.

- **Chapter 6: Adaptive FEM-DEM bridging coupling**

In this final chapter, we discuss the implementation of the adaptive FEM-DEM coupling. The criteria used to determine when the discrete domain must expand is based on the average change of number of neighbors. The adaptive coupling is validated for a FEM-DEM coupling but also on MD/FEM coupling. A final study, including elliptic rigid bodies at the DEM interface, is conducted.

- **Chapter 7: Conclusion**

A summary of the main results is provided, along with a discussion on future work.

Chapter 2

Numerical methods

Contents

2.1   Discrete Element Method

The Discrete Element Method (DEM), was developed by Cundall and Strack [32], for the modelling of granular material. While both DEM and Molecular Dynamics (MD) involve calculating interaction forces, velocities, and particle positions, they differ in their applications and scale of operation. MD is tailored for studying atomic interactions at the nano-scale, employing interatomic potentials such as the Lennard Jones potential, with atoms considered as point particles resulting in three degrees of freedom. Consequently, MD is not suitable for analyzing granular materials represented by particles at larger scales. In contrast, DEM operates on a broader scale, ranging from nano to macro, and utilizes contact laws to describe interactions among particles. DEM considers particles with defined radii, allowing for rotational degrees of freedom, totaling six degrees of freedom. This capability is crucial for accurately modeling the behavior of granular materials.

2.1.1 Interaction force

The contact force between two particles depends on a normal component F_n, a tangential component F_t, and velocity damping terms:

$$\boldsymbol{F} = \left(-F_n - c_n v_n\right)\boldsymbol{n} + \left(-F_t - c_t v_t\right)\boldsymbol{t} \tag{2.1}$$

where $\boldsymbol{n}$ and $\boldsymbol{t}$ are unit vectors in the normal and tangential directions, v_n and v_t are the relative velocities between two particles in these directions, and c_n, c_t are damping factors.

One fundamental characteristic of DEM lies in the modeling of particles as non-deformable spheres. The contact force between these particles is determined by their overlap δ_n defined as:

$$\delta_n = d_{ij} - r_i - r_j, \tag{2.2}$$

with d_{ij} the distance between the two particle's center i and j, and r_i, r_j their respective radii. In Figure 2.1 is represented the overlap between two particles. When $\delta_n < 0$, particles are in contact, while when, $\delta_n > 0$, they are not. This assumption is valid for model involving small deformations, i.e., small overlap δ_n.
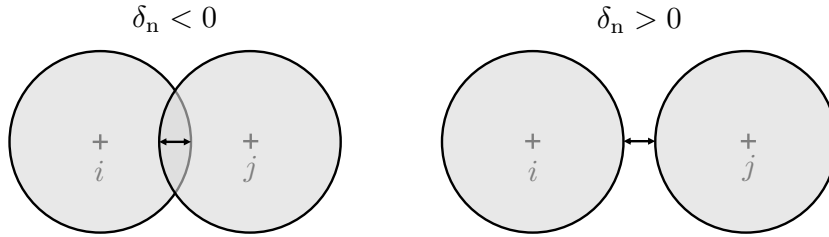
Figure 2.1: Schematic illustrating the overlap between two particles. When $\delta_n < 0$, particles are in contact, conversely, when $\delta_n > 0$, they are not in contact.

Hookean interaction

In the case of a Hookean interaction, the normal component term F_n is a linear function of the overlap between the particles δ_n and is expressed as $k_n \delta_n$, where k_n is the normal stiffness of the grains. The normal damping factor c_n is expressed as $\gamma_n m_{\text{eff}}$, where γ_n is the normal viscoelastic damping constant and $m_{\text{eff}} = m_i m_j / (m_i + m_j)$ is an effective mass. Similarly, the tangential component F_t is a linear spring term, expressed as $k_t \delta_t$, where k_t represents the tangential stiffness of the grains, and δ_t the sliding distance. The tangential damping factor is $c_t = \gamma_t m_{\text{eff}}$, with γ_t, the tangential viscoelastic damping constant. Consequently, the formula for a Hookean interaction is:

$$\boldsymbol{F} = (-k_{\mathrm{n}}\delta_{\mathrm{n}} - \gamma_{\mathrm{n}}m_{\mathrm{eff}}v_{\mathrm{n}})\,\boldsymbol{n} + (-k_{\mathrm{t}}\delta_{\mathrm{t}} - \gamma_{\mathrm{t}}m_{\mathrm{eff}}v_{\mathrm{t}})\,\boldsymbol{t} \tag{2.3}$$

The units of k_{n}, k_{t} are expressed in N/m, and the units of γ_{n}, γ_{t} are in s^{-1}.

Hertzian interaction

In the case of an Hertzian-Minldin interaction, the normal component F_{n} is a non-linear function of the overlap between the particles. The general contact law is:

$$\boldsymbol{F} = \sqrt{\delta_{\mathrm{n}}}\sqrt{\frac{r_i r_j}{r_i + r_j}}\left((-K_{\mathrm{n}}\delta_{\mathrm{n}} - \Gamma_{\mathrm{n}}m_{\mathrm{eff}}v_{\mathrm{n}})\,\boldsymbol{n} + (-K_{\mathrm{t}}\delta_{\mathrm{t}} - \Gamma_{\mathrm{t}}m_{\mathrm{eff}}v_{\mathrm{t}})\,\boldsymbol{t}\right) \tag{2.4}$$

where r_i, and r_j are the radii of the particle i and j. K_{n} and K_{t} are the stiffnesses expressed in N/m^2, while Γ_{n} and Γ_{t} are the viscoelastic damping constants, in units of (m·s)$^{-1}$, for normal and tangential directions, respectively. The parameter K_{n} is computed using Hertz model [57, 101] and K_{t} using Mindlin model [65]:

$$K_{\mathrm{n}} = \frac{(2/3)E}{1 - \nu^2}, \quad K_{\mathrm{t}} = \frac{2E}{(1 + \nu)(2 - \nu)}. \tag{2.5}$$

Hence, the Hertzian contact law should be employed for accurately modeling the non-linear elastic contact between two spheres, while the Hookean model can be used when a simpler, linear approximation is sufficient.

2.1.2   Coarse-grained contact law

Aghababaei et al. [2] investigated wear mechanisms between two half-spherical asperities using two-dimensional MD simulations. They showed that if the junction size between the two asperities is larger than a critical length scale d^*, a wear particle forms from the two asperities, while if the junction size is smaller than the critical length scale the asperities deform plastically, and exchange superficial atoms. The critical length scale d^* is derived by evaluating the balance between the adhesive energy required to create new surfaces E_{surface} and the elastic energy stored by shearing the system E_{elastic}, similarly to Griffith theory [50]. The order of the critical length scale is given by:

$$d^* \sim \frac{\gamma E}{\sigma_{\mathrm{n}}^2}, \tag{2.6}$$

with γ the surface energy, E the Young's modulus, and σ_{n} the tensile strength.

Pham-Ba and Molinari [75] developed a coarse-grained DEM contact law with cohesive forces that reproduce the material length scale d^* observed in MD while significantly reducing computational time by using particles that are ten times larger. The interaction forces between particles are tuned to ensure that an assembly of multiple particles demonstrates specific material properties, including Young's modulus E, Poisson's ratio

ν, tensile strength σ_n, shear strength σ_t, surface energy γ, restitution coefficient η, and density ρ. Pham-Ba and Molinari's simple coarse-grained contact law differs from other DEM contact laws, such as those derived from Johnson-Kendall-Roberts theory [58] or Derjaguin-Mullar-Toporov [33], which also integrate adhesion, but do not characterize the material properties of an assembly of particles.

In the following paragraphs, the coarse-grained DEM law developed by Pham-Ba and Molinari will be detailed. For further information, refer to their original paper [75]. Similar to Section 2.1.1, the force between two particles is expressed by Eq. 2.1.

Normal force

The normal component F_n depends on the overlap between the particles δ_n, and their relation is illustrated in Figure 2.2. When the particles are overlapping ($\delta_n \leq 0$), the normal component is expressed as a repulsive Hookean force $k_{n,mat}\delta_n$. Here, $k_{n,mat}$ is the normal stiffness chosen to match desired macroscopic elastic properties, with the expression provided in the Material properties section. When the particles are not in contact ($\delta_n > 0$), the Hookean force is maintained until the overlap reaches the maximum elastic distance δ_e. After δ_e, the normal force decreases linearly until reaching the fracture distance δ_f. Finally, if the overlap is superior to the fracture distance ($\delta_n > \delta_f$), the normal component is null.
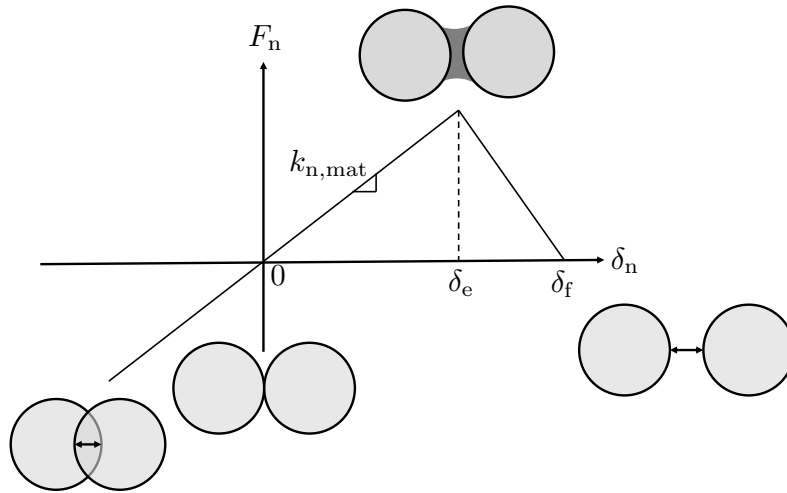
Figure 2.2: Normal force as a function of the overlap δ_n between two particles, based on the DEM coarse-grained law from Pham-Ba and Molinari [75]. Image partially reproduced from their paper, with the authors' permission.

Thus, the expression for the normal force is:

$$F_{\mathrm{n}} = \begin{cases} k_{\mathrm{n,mat}}\delta_{\mathrm{n}} & \text{if } \delta_{\mathrm{n}} \leq \delta_{\mathrm{e}}, \\ -\dfrac{k_{\mathrm{n,mat}}\delta_{\mathrm{e}}}{\delta_{\mathrm{f}} - \delta_{\mathrm{e}}}(\delta_{\mathrm{n}} - \delta_{\mathrm{f}}) & \text{if } \delta_{\mathrm{e}} < \delta_{\mathrm{n}} \leq \delta_{\mathrm{f}}, \\ 0 & \text{if } \delta_{\mathrm{n}} > \delta_{\mathrm{f}}, \end{cases} \tag{2.7}$$

It should be noted that the normal force does not depend on the history of δ_{n}; hence, the particles can detach and reattach without any weakening of the bond.

Tangential force
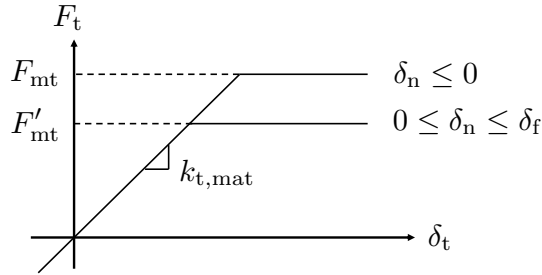
Figure 2.3: Tangential force as a function of the sliding distance δ_{t} between two particles, based on the DEM coarse-grained law from Pham-Ba and Molinari [75]. Image reproduced from their paper with the author's permission.

The tangential force depends on the overlap between particles δ_{n} and the sliding distance δ_{t}. The tangential force pattern is given in Figure 2.3. When the particles are overlapping ($\delta_{\mathrm{n}} \leq 0$), the tangential force is expressed as $k_{\mathrm{t,mat}}\delta_{\mathrm{t}}$, with a maximum reachable value F_{mt}. Here $k_{\mathrm{t,mat}}$ is the tangential stiffness chosen to match desire macroscopic properties; the expression is provided in the Material properties section. When the particles are not in contact ($\delta_{\mathrm{n}} > 0$) but the overlap is inferior to the fracture distance ($\delta_{\mathrm{n}} < \delta_{\mathrm{f}}$), the tangential force is expressed as $k_{\mathrm{t,mat}}\delta_{\mathrm{t}}$ with a maximum achievable value of F'_{mt}, a lower value than F_{mt}. Finally, if $\delta_{\mathrm{n}} > \delta_{\mathrm{f}}$, no tangential force is applied. The specific expressions for F_{mt} and F'_{mt} are detailed in the Material properties section.

Material properties

A specificity of the Pham-Ba and Molinari contact law is that it calculates force parameters between particles to achieve specific macroscopic properties of a particle assembly. With this consideration, they defined the inter-particle force parameters as:

$$m_{\text{eff}} = \frac{m_i m_j}{m_i + m_j}, \qquad\qquad r_{\text{eff}} = \min(r_i, r_j) \tag{2.8}$$

$$A_{\text{n}} = \sqrt{2} r_{\text{eff}}^2 \frac{1}{1 - 2\nu}, \qquad\qquad A_{\text{t}} = \sqrt{2} r_{\text{eff}}^2 \frac{1 - 4\nu}{(1 - 2\nu)(1 + \nu)}, \tag{2.9}$$

$$k_{\text{n,mat}} = \frac{A_{\text{n}} E}{r_i + r_j}, \qquad\qquad k_{\text{t,mat}} = \frac{A_{\text{t}} E}{r_i + r_j}, \tag{2.10}$$

$$c_{\text{n}} = \frac{2(1 - \eta)}{\pi} \sqrt{k_{\text{n,mat}} m_{\text{eff}}}, \qquad\qquad c_{\text{t}} = \frac{2(1 - \eta)}{\pi} \sqrt{k_{\text{t,mat}} m_{\text{eff}}}, \tag{2.11}$$

$$\delta_{\text{e}} = \frac{(r_i + r_j)\sigma_{\text{n}}}{E}, \qquad\qquad \delta_{\text{f}} = \frac{4\gamma}{\sigma_{\text{n}}}, \tag{2.12}$$

$$F_{\text{mt}} = A_{\text{t}} \sigma_t, \qquad\qquad F'_{\text{mt}} = \min\left(\frac{\delta_{\text{f}} - \delta_{\text{n}}}{\delta_{\text{f}}}, 1\right) F_{\text{mt}} \tag{2.13}$$

$$F_{\text{t}} = \min(k_{\text{t}} \delta_{\text{t}}, F'_{\text{mt}}), \tag{2.14}$$

$$\tag{2.15}$$

with r_i and r_j the radii of the interacting particles, and m_i, m_j their masses. The effective cross-sectional areas in the normal and tangential directions are indicated by A_{n} and A_{t}. Here, E is the targeted Young's modulus, σ_{n} the targeted tensile strength, σ_{t} the targeted shear strength, γ the targeted surface energy, and η the targeted restitution coefficient. The expression of δ_{f}, and the matching of all material properties is valid for particles which respect:

$$r_i + r_j \leq d_{\text{c}}, \text{ with the critical diameter } d_{\text{c}} = \frac{4\gamma E}{\sigma_{\text{n}}^2}. \tag{2.16}$$

For more details, refer to [75]. Additionally, if a particle is smaller than the neighbor size δ_{f}, it will interact with particles beyond its closest neighbors, extending the interaction range. Therefore, to avoid an important increase in computational cost, the minimum particle size should be greater than the value of δ_{f}:

$$d_{\text{min}} = \frac{4\gamma}{\sigma_{\text{n}}} \tag{2.17}$$

Hence, the particle sizes should be chosen such that $d_{\text{min}} \leq r_i + r_j \leq d_{\text{c}}$ to ensure matching all material properties and avoid unnecessary increases in computational cost. Following this general overview of interaction forces in the Discrete Element Method (DEM), the next section will now explore specific instances of their application.

2.1.3 Third-body modeling

Elastic properties

The mechanical behavior of granular materials is influenced by their heterogeneity. Hence measuring their elastic properties has proven to be non-trivial and dependent on multiple parameters. H. A. Makse et al. [61] conducted numerical simulations to determine the bulk modulus and shear modulus of granular assemblies, with particles interacting through Hertz-Mindlin contact forces in a confined system. They compared their results with experimental data and elastic medium theory [39, 92]. Their findings underscore the importance of considering pressure when evaluating the elastic properties of granular materials, along with the need to account for relaxation effects following an infinitesimal strain transformation. I. Agnolin [5] also reports the importance of pressure when evaluating the elastic properties of granular materials. E. Somfai et al. [86] explored wave propagation in granular media through simulations using Hertzian-Mindlin contact law, revealing the influence of packing. H. Cheng et al. [26] performed static and dynamic probing with an Hertzian-Mindlin contact law, measuring elastic moduli and emphasizing the dependence on various parameters, including stress/strain history. Additional studies, such as the work by Schöpfer et al. [83], have explored the impact of porosity on the macroscopic properties of three-dimensional cohesive granular media using bonded spheres.

Third-body modeling

DEM has been employed to model the gouge and study its behavior, including aspects such as friction, stability, stick-slip events, and gouge fluidization [1, 43, 46, 56, 77, 93]. These studies generally consider spherical particles interacting via an Hertzian contact without cohesion. To provide a representation of the gouge that includes different grain fragment shape, Abe and Mair [1] model each particle as an agglomerate of smaller spherical particles. This approach allows the agglomerate of particles to break into different fragment shape. Using this model to explore granular fault gouge friction, they demonstrated that gouge fragment angularity is an important parameter to control the macroscopic friction. Consequently, their study underscores the limitations of using non-adhesive spherical particles, which cannot break into smaller fragments, in modeling fault gouge behavior.

Other approaches consider a more complex representation of the third-body. Mollon modeled the third-body using cohesion between particles, but also considering deformable grains via a multibody meshfree strategy [67–69]. Notably, this approach allowed him to model the flow regime of a deformable third-body and investigate the influence of grain properties, friction, and energy dissipation [70]. Several flow regimes were simulated: a shear band regime, a debris forming regime, and mixed regimes. The mixed regime, being an intermediate case, where particles detach, reattach, agglomerate, without forming a complete debris. It was demonstrated that the third-body's flow regime is linked to the macroscopic friction through its ability to form mesostructures like force chains and agglomerates. Zhang et al. [102] also used the multibody meshfree method to explore the influence of the cohesion between particles on the third-

body rheology and friction. A soft discrete element method has also been developed to model deformable grains while reducing computational time compared to the multibody meshfree strategy [71].

Pham-Ba and Molinari [76] utilized their contact law (Section 2.1.2) to study the influence of the macroscopic material properties (tensile strength, adhesion) on the third-body regimes. Adjusting material properties, they simulated the three distinct regimes for the third-body: debris rolling regime, a shear band regime, and a mixed regime.

2.2 Coupling Methods

Considering a DEM box with a length of 10 cm, one million particles with a diameter of 1 mm are required to fill the entire cube in a square lattice arrangement, resulting in 6 million degrees of freedom. Consequently, to model large domain, there arises a need for a methodology that strikes a balance between accuracy and cost efficiency. One effective approach is to couple continuous and discrete domains. Coupling methods, originally developed to couple MD and FEM, are categorized in two classes: the edge-to-edge method, which involves two distinct domains connected by mutual boundary conditions, and the overlapping method, where the two domains coexist within a "mixed" region.

2.2.1 Edge-to-edge coupling

The edge-to-edge coupling method involves two separate domains – the continuous domain and the atomic domain – without any overlap. To illustrate this coupling for MD, we consider the schematic of Figure 2.4. The mesh is refined until reaching the atomic scale at the boundary in such a way that each node is associated to an atom.

In this method, pad atoms are introduced at the nodes of the mesh (depicted as green atoms in Figure 2.4). The pad atoms serve as a boundary condition for the atomic domain, ensuring equilibrium of atoms in the B' regions. Without the introduction of pad atoms, a surface effect would occur, as the atoms in the B' regions would not be equilibrated. This surface effect would lead to an undesirable displacement of the atoms near the coupling (B'). Consequently, the potential cutoff radius R_{cut} determines the size of the different regions.

Similarly to the atomic domain, the first layer of atoms ahead of the continuum domain is considered as pad nodes for the mesh, acting as boundary condition (depicted as black atoms in Figure 2.4). The continuum domain is divided into two regions: C and Ω'. Region C corresponds to elements of the continuum domain included in the coupling interface, while region Ω' corresponds to the remaining part. Examples of this method applied in MD-FEM are the Macroscopic, Atomistic, *ab initio* Dynamics (MAAD) Method [23], the Quasi Continuum Method (QC) [88], and the Coarse
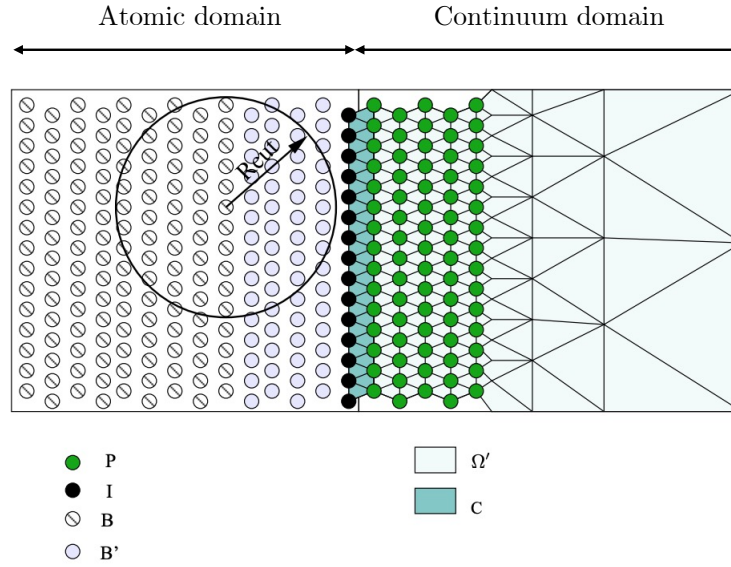
Figure 2.4: Schematic of an edge-to-edge coupling between MD and FEM. Image from the thesis of Dr. Anciaux [11], with the author's permission.

Grained Molecular dynamics method (CGMD) [81]. An edge-to-edge approach can also be used to couple atomistic and discrete dislocation in two dimensions [85] and in three dimensions [14, 27, 51].

In FEM-DEM coupling, certain studies have adopted an edge-to-edge approach [47, 68], with an implementation that differs from MD. Both studies consider a granular material between two surrounding plates, considered as continuum. Gao et al. [47] used the combined finite-discrete element method (FDEM) to discretize both the particles and the surrounding plates. Consequently, no pad particles are required, and reciprocal boundary conditions are determined by the interaction forces between the particles and the plates. Mollon's model [68] utilized a multibody meshfree to model the surrounding regions as rigid bodies and the particles as either rigid or compliant bodies. Similarly, to the previous approach [47] a fine discretization of the particles is required, which should be considered in the computation time. Olivier et al. [20] used the approach from Mollon to model a deformable third-body localized between a rigid top body and an elastic bottom body. This strategy enabled them to assess large systems and determine how third-body flow impacts the first bodies. They found minimal damage with plastic flow, but significant damage with agglomerated granular flow.

2.2.2   Overlapping/Bridging coupling

Disclaimer

This section is in part reproduced from the article: Manon Voisin-Leprince, Joaquin Garcia-Suarez, Guillaume Anciaux, Jean-François Molinari, "Finite element method–discrete element method bridging coupling for the modeling of gouge" (2022), *International Journal for Numerical Methods in Engineering* [91]. All authors have granted their permission.

At the opposite of the edge-to-edge method which considers two disjoint domains, the overlapping method considers a reconciliation zone where the two models are "mixed" together. H. B. Dhia is a pioneer in this field with the Arlequin method [34] which glues physical domains together by means of Lagrange multipliers. The *bridging* method [17, 97] is a classical overlapping method based on the Arlequin method which couples atomistic and continuum domains. In this thesis, we considered two different overlapping method formulations. The first method imposes strong coupling through a Lagrange constraint, where each particle position is constrained to the equivalent position derived from the FEM interpolation (*bridging* method). The second method is a weak coupling that enforces such a constraint in an average sense within the volume of each element. Figure 2.5 represents the atomic and continuum with the bridging region in red, and a boundary/pad region for the atomic domain in purple. In the following sections, the coupling formulation occuring in the bridging region is expressed in matrix form.
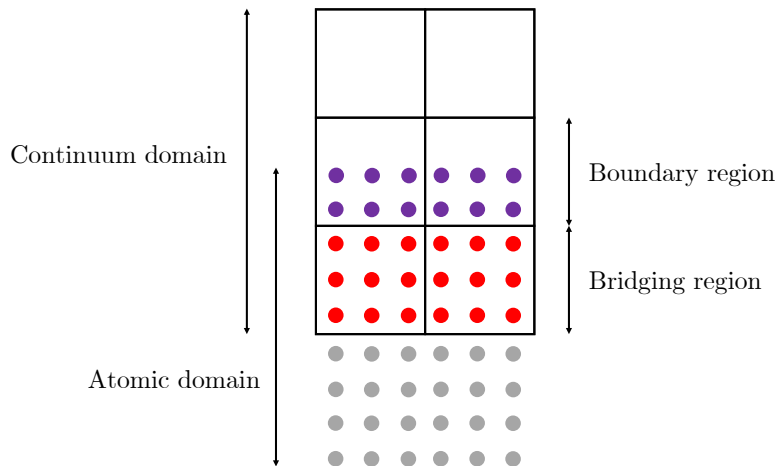
Figure 2.5: Schematic of an overlapping coupling between MD and FEM. The atomic domain is depicted with circles, and the continuum with a black mesh. The bridging region is shown in red, and the boundary/pad region in purple.

The first step of Arlequin couplings consists in defining an energy weighting, which permits to control the relative influence of each model. Thus, the global energy in the system is defined using the Hamiltonian

$$H = \int_\Omega \alpha(X)E^{\mathrm{C}}(X) + (1 - \alpha(X))E^{\mathrm{D}}(X) \quad dX, \tag{2.18}$$

where E^{C} and E^{D} are the energy densities in the continuum and discrete regions. These are weighted in the bridging zone using a scaling function α which defines the influence of the continuum domain $\alpha(X)$ for a given spatial location X.

However, kinematic consistency between the coupled models cannot be enforced by the energy weighting. Therefore, the two models are tied together by means of Lagrange constraints. The energy weighting and the Lagrange constraint ($\mathbf{g} = \mathbf{0}$) lead to a Lagrangian problem which can be summarized as:

$$H_{\mathrm{L}} = H + \boldsymbol{\lambda}^{\mathrm{T}} \mathbf{g}, \tag{2.19}$$

where H is the original Hamiltonian, H_{L} its expanded version including the coupling restrictions and $\boldsymbol{\lambda}$ the Lagrange multiplier matrix. This leads to new equations of motion:

$$\begin{cases} \overline{\boldsymbol{M}} \ddot{\boldsymbol{u}} = \boldsymbol{F} + \boldsymbol{\lambda} \cdot \frac{\partial \mathbf{g}}{\partial \boldsymbol{u}} \\[2mm] \overline{\boldsymbol{m}} \ddot{\boldsymbol{d}} = \boldsymbol{f} + \boldsymbol{\lambda} \cdot \frac{\partial \mathbf{g}}{\partial \boldsymbol{d}} \end{cases} \tag{2.20}$$

where $\boldsymbol{u}, \boldsymbol{F}$ and $\boldsymbol{M}$ are displacements, forces and masses of the FEM domain, and $\boldsymbol{d}, \boldsymbol{f}$ and $\boldsymbol{m}$ are the displacements, forces and masses of the particles. The energy weighting leads to the altered masses $\overline{\boldsymbol{m}}$ and $\overline{\boldsymbol{M}}$, which are defined such that $\overline{m}_i = (1 - \alpha(\mathbf{X}_i))m_i$ and $\overline{M}_I = \alpha(\mathbf{X}_I)M_I$ with $\mathbf{X}_i$ and $\mathbf{X}_I$ the initial positions of particles and continuum FEM nodes. The *Verlet* [8] scheme is employed to perform the time integration of the uncoupled domains, which produces test velocities $(\dot{\boldsymbol{u}}^{\star}, \dot{\boldsymbol{d}}^{\star})$ not respecting the coupling constraint.

$$\left| \begin{array}{l} \dot{\boldsymbol{u}}^{\star,n+1/2} = \dot{\boldsymbol{u}}^{\star,n} + \frac{\Delta t}{2} \boldsymbol{M}^{-1} \boldsymbol{F}^{n} \\ \boldsymbol{u}^{n+1} = \boldsymbol{u}^{\star,n} + \Delta t \dot{\boldsymbol{u}}^{\star,n+1/2} \\ \text{Computation of } \boldsymbol{F}^{n+1} \\ \dot{\boldsymbol{u}}^{\star,n+1} = \dot{\boldsymbol{u}}^{\star,n+1/2} + \frac{\Delta t}{2} \boldsymbol{M}^{-1} \boldsymbol{F}^{n+1} \end{array} \right. \qquad \left| \begin{array}{l} \dot{\boldsymbol{d}}^{\star,n+1/2} = \dot{\boldsymbol{d}}^{\star,n} + \frac{\Delta t}{2} \boldsymbol{m}^{-1} \boldsymbol{f}^{n} \\ \boldsymbol{d}^{n+1} = \boldsymbol{d}^{\star,n} + \Delta t \dot{\boldsymbol{d}}^{\star,n+1/2} \\ \text{Computation of } \boldsymbol{f}^{n+1} \\ \dot{\boldsymbol{d}}^{\star,n+1} = \dot{\boldsymbol{d}}^{\star,n+1/2} + \frac{\Delta t}{2} \boldsymbol{m}^{-1} \boldsymbol{f}^{n+1} \end{array} \right.$$
$$\tag{2.21}$$

The correction of the test velocities needs to be done within the reconciliation zone thanks to the Lagrange multipliers, which gives at the n-th step the following form [97]:

$$\left| \begin{array}{l} \dot{\boldsymbol{u}}^{n+1} = \dot{\boldsymbol{u}}^{\star,n+1} - \overline{\boldsymbol{M}}^{-1} \frac{\partial \mathbf{g}}{\partial \boldsymbol{u}}^{\mathrm{T}} \cdot \boldsymbol{\lambda} \\[3mm] \dot{\boldsymbol{d}}^{n+1} = \dot{\boldsymbol{d}}^{\star,n+1} - \overline{\boldsymbol{m}}^{-1} \frac{\partial \mathbf{g}}{\partial \boldsymbol{d}}^{\mathrm{T}} \cdot \boldsymbol{\lambda} \end{array} \right. \tag{2.22}$$

The velocities produced by Eq. 2.22 are chosen to satisfy the time derivative of the Lagrange constraint $\dot{\mathbf{g}} = \mathbf{0}$. This choice imposes that the Lagrange multipliers $\boldsymbol{\lambda}$ are obtained by solving:

$$\dot{\mathbf{g}} = \mathbf{A}\boldsymbol{\lambda}, \tag{2.23}$$

where $\mathbf{A}$ is the constraint matrix, which depends on the constraint function $\mathbf{g}$ and can deliver distinct formulations of the coupling, such as the strong and weak coupling detailed in sections 2.2.2.1 and 2.2.2.2.

In addition to the coupling region, a boundary/pad region, sets the boundary conditions for the discrete domain (purple region in Figure 2.5). Here, the displacement of particles $\boldsymbol{d}$ are constrained by the displacement of the FEM node $\boldsymbol{u}$,

$$\boldsymbol{d} = \boldsymbol{N}^{\mathrm{T}}\boldsymbol{u}, \tag{2.24}$$

with $\boldsymbol{N}$ the standard finite-element shape function.

2.2.2.1   Strong coupling

The strong coupling considers a Lagrange constraint, where each particle is constrained to the position interpolated from the FEM displacement field. Therefore, the constraint applied to the particles is expressed as:

$$\mathbf{g} = \boldsymbol{N}^{\mathrm{T}}\mathbf{u} - \boldsymbol{d} = \mathbf{0}, \tag{2.25}$$

where $\boldsymbol{N}^{\mathrm{T}}\boldsymbol{u}$ is the interpolated displacement for all coupled particles, computed with the standard finite-element shape functions evaluated at each of the particles' positions (X_i) :

$$\mathbf{N} = \begin{bmatrix} \varphi_1(X_1) & \cdots & \varphi_1(X_i) \\ \vdots & \cdots & \vdots \\ \varphi_I(X_1) & \cdots & \varphi_I(X_i) \end{bmatrix} \tag{2.26}$$

where φ_I is the FEM shape function for node I employed to discretize the continuum domain. The expression of corrected velocities from Eq. 2.22 together with the time derivative of Eq. 2.25 allows to identify the particular form of Eq. 2.23 specific to the strong coupling:

$$\underbrace{\boldsymbol{N}^{\mathrm{T}}\dot{\boldsymbol{u}}^{\star,n+1} - \dot{\boldsymbol{d}}^{\star,n+1}}_{\dot{\mathbf{g}}} = \underbrace{\left(\boldsymbol{N}^{\mathrm{T}}\overline{\boldsymbol{M}}^{-1}\boldsymbol{N} - \overline{\boldsymbol{m}}^{-1}\right)}_{\boldsymbol{A}}\boldsymbol{\lambda}, \tag{2.27}$$

Additionally, to reduce the computational cost and provide a dissipative treatment of wave reflections [11], the constraint matrix $\mathbf{A}$ can be lumped. Therefore, the Lagrange multipliers can be obtained by solving Eq. 2.27. Finally, the velocities can be corrected using the computed Lagrange multipliers, which leads to the following algorithm to be applied in the reconciliation zone:

$$\left|\begin{aligned}
&\dot{\mathbf{g}} = \boldsymbol{N}^{\mathrm{T}}\dot{\boldsymbol{u}}^{\star,n+1} - \dot{\boldsymbol{d}}^{\star,n+1} \\
&\boldsymbol{A} = \boldsymbol{N}^{\mathrm{T}}\overline{\boldsymbol{M}}^{-1}\boldsymbol{N} - \overline{\boldsymbol{m}}^{-1} \\
&\textit{Optional lumping of } \boldsymbol{A} \\
&\boldsymbol{\lambda} = \boldsymbol{A}^{-1}\dot{\mathbf{g}} \\
&\dot{\boldsymbol{u}}^{n+1} = \dot{\boldsymbol{u}}^{\star,n+1} - \overline{\boldsymbol{M}}^{-1}\boldsymbol{N}\boldsymbol{\lambda} \\
&\dot{\boldsymbol{d}}^{n+1} = \dot{\boldsymbol{d}}^{\star,n+1} + \overline{\boldsymbol{m}}^{-1}\boldsymbol{\lambda}
\end{aligned}\right. \tag{2.28}$$

2.2.2.2 Weak coupling

The idea behind the weak coupling is to relax the constraint so that it is respected in an integral sense. The intended effect is that the constraint is imposed in average over each element and not anymore point wise over the particles. For this, the standard collocation method taken from finite elements is employed, leading to the following weak constraint:

$$\mathbf{g}_I^{\mathrm{W}} = \int_\Omega \varphi_I(X)\mathbf{G}(X)dX = \sum_i \varphi_I(X_i)\mathbf{g}_i = \mathbf{0} \tag{2.29}$$

where the integral becomes a discrete sum due to the discrete nature of the constraint, which can be formally written by defining the continuous constraint $\mathbf{G}(X) = \sum_i \delta(X - X_i)\mathbf{g}_i$ with Dirac δ distributions. Therefore, there are as many Lagrange constraints as the number of coupled FEM nodes, and it takes the following matricial form:

$$\mathbf{g}^{\mathrm{W}} = N\left(N^{\mathrm{T}}\boldsymbol{u} - \boldsymbol{d}\right) = \mathbf{0} \tag{2.30}$$

This leads to the weak formulation of Eq. 2.23:

$$\underbrace{\boldsymbol{N}\left(\boldsymbol{N}^{\mathrm{T}}\dot{\boldsymbol{u}}^{\star,n+1} - \dot{\boldsymbol{d}}^{\star,n+1}\right)}_{\dot{\mathbf{g}}^{\mathrm{W}}} = \underbrace{\boldsymbol{N}\overbrace{\left(\boldsymbol{N}^{\mathrm{T}}\overline{\boldsymbol{M}}^{-1}\boldsymbol{N} + \overline{\boldsymbol{m}}^{-1}\right)}^{\boldsymbol{A}}\boldsymbol{N}^{\mathrm{T}}}_{\boldsymbol{A}^{\mathrm{W}}}\boldsymbol{\lambda}^{\mathrm{W}} \tag{2.31}$$

In the case of weak coupling, the constraint matrix $\mathbf{A}^{\mathrm{W}}$ cannot be lumped as it would introduce too important approximations in the resolution of the Lagrange multipliers, a poor control of the influence of each coupled model and a spurious time evolution. Considering the previous developments, the algorithm employed to correct weakly for the velocities in the reconciliation zone becomes:

$$\left|\begin{aligned}
&\dot{\mathbf{g}}^{\mathrm{W}} = \boldsymbol{N}\left(\boldsymbol{N}^{\mathrm{T}}\dot{\boldsymbol{u}}^{\star,n+1} - \dot{\boldsymbol{d}}^{\star,n+1}\right) \\
&\boldsymbol{A} = \boldsymbol{N}^{\mathrm{T}}\overline{\boldsymbol{M}}^{-1}\boldsymbol{N} - \overline{\boldsymbol{m}}^{-1} \\
&\boldsymbol{A}^{\mathrm{W}} = \boldsymbol{N}\boldsymbol{A}\boldsymbol{N}^{\mathrm{T}} \\
&\boldsymbol{\lambda}^{\mathrm{W}} = [\boldsymbol{A}^{\mathrm{W}}]^{-1}\dot{\mathbf{g}} \\
&\dot{\boldsymbol{u}}^{n+1} = \dot{\boldsymbol{u}}^{\star,n+1} - \overline{\boldsymbol{M}}\boldsymbol{N}\boldsymbol{N}^{\mathrm{T}}\boldsymbol{\lambda}^{\mathrm{W}} \\
&\dot{\boldsymbol{d}}^{n+1} = \dot{\boldsymbol{d}}^{\star,n+1} + \overline{\boldsymbol{m}}\boldsymbol{N}\boldsymbol{\lambda}^{\mathrm{W}}
\end{aligned}\right. \tag{2.32}$$

The bridging method, originally developed for MD-FEM, has been used to couple continuum and amorphous domain. Wellmann and Wriggers [94] employed an overlapping approach to couple FEM and DEM in three-dimension, while considering various grain shapes. Yue et al. [98] used an overlapping approach to couple discrete and continuum domains in three dimensions, employing the Material Point Method (MPM) for the continuum. This approach allows for the modeling of large deformations compared to methods that use FEM for the continuum, making it suitable for particle flow simulations. However, it should be noted that MPM is computationally more expensive than FEM.

Chapter 3

Boundary conditions impact on the third-body evolution

Contents

3.1 Introduction

The evolution of the third-body over time is influenced by various factors. Mollon employed a deformable discrete element particle method [71] to investigate the impact of the grain properties on the third-body's flow regime, friction, and energy dissipation [70]. He demonstrated that the third-body's flow regime is linked to the macroscopic friction through its ability to form mesostructures like force chains and agglomerates. Zhang et al. [102] also used the method developed by Mollon to explore the influence of the cohesion between particles on the third-body rheology and friction. These simulations [71, 102] depict a mixed regime of the third-body, where particles can detach, reattach, and agglomerate without forming complete debris.

    The coarse-grained contact law developed by Pham-Ba and Molinari [76], summarized in section 2.1.2, allows the determination of the interparticle force parameters

based on the desired macroscopic material properties. This contact law enables the replication of key wear mechanisms observed in MD simulations while significantly reducing computational costs. Pham-Ba and Molinari [75] utilized this law to study the influence of the macroscopic material properties (tensile strength, adhesion) on the third-body regimes. Adjusting material properties, they simulated three distinct regimes for the third-body: mixed regime, debris rolling, and shear band.

These previous studies were conducted using a relatively small DEM system, limiting the ability of the third-body to evolve beyond a certain point. Additionally, the evolution of the third-body may have been influenced by the DEM height and the imposed boundary conditions. Therefore, in this chapter, we modeled two material blocks to investigate how their heights and boundary conditions affect the third-body created at their interface during shearing. Both force control (external force applied) and displacement control (rollers) boundary conditions were examined. Section 3.3 presents results on the influence of the DEM height and the boundary condition on the evolution of the third-body. By adjusting the material properties, we replicated the three regimes observed in a third-body (mixed regime, debris rolling, and shear band) and examined the impact of the boundary conditions and the DEM height on these regimes. Additionally, this section presents the boundary conditions of a subsystem. Finally, Section 3.4 offers concluding remarks.

3.2 Method

3.2.1 Discrete Domain

We employed the discrete element method, utilizing the coarse-grained contact law developed by Pham-Ba and Molinari [76] and summarized in section 2.1.2. In this chapter the materials properties are chosen such that the Young's modulus E, the density ρ, and the restitution coefficient η, correspond to the material properties of SiO_2. The Poisson's ratio ν is set to 0.25, limiting the interaction force to its normal component (Eq. 2.9). Macroscopic shear force still exists due to the long-range property of the normal spring force. The length of the system in the shearing direction is set to be $L_x = 100d_0$, with d_0 the mean particle diameter. The critical length scale, denoted as d^* and responsible for defining the minimum size of wear debris [2] (refer to Eq. 2.6), is set as $d^* = 0.1L$. The minimum and maximum particle sizes, as determined by the DEM coarse-grained law (details in Section 2.1.2), are $d_{\text{theory,max}} = 1.6$nm (Eq. 2.16) and $d_{\text{theory,min}} = 0.16$nm (Eq. 2.17). Based on these values, we selected a log-normal distribution of particle sizes with a mean grain diameter of $d_0 = 1.3$nm, a maximum grain diameter of $d_{\max} = 1.2d_0$, a minimum grain diameter of $d_{\min} = 0.8d_0$, and a variance of $0.2(d_{\max} - d_{\min})$nm. The tensile strength will be varied during this study, with the values set as $0.1E$, $0.11E$, and $0.2E$. The surface energy is set consequently, taking into account the expression for d^*, resulting in the formula $\gamma = \frac{d^* \sigma_{\text{n}}^2}{32E}$. Table 3.1

summarizes the material properties used in this chapter.

Table 3.1: Material properties and particle size parameters.

Young's modulus, E	73 GPa
Grain density, ρ	2200 kg/m^3
Poisson's ratio, ν	0.25
Critical length scale d^*	$0.1L_x$ nm
Restitution coefficient, η	0.9
Tensile strength, σ_n	$[0.1, 0.11, 0.2]E$ GPa
Surface energy, γ	$d^*\sigma_n^2/(32E)$ N/m
Mean grain diameter, d_0	1.3 nm
Maximimum diameter, d_{max}	$1.2d_0$ nm
Minimimum diameter, d_{min}	$0.8d_0$ nm
Variance, σ_p	$0.2(d_{max} - d_{min})$ nm

3.2.2 Geometries

Multiple DEM samples were examined, all characterized by a consistent length in the x direction ($L_x = 100d_0$) and uniform thickness in the z-direction ($L_z = 3d_0$). Various DEM heights L were explored, ranging from $50d_0$ to $600d_0$. Initially, two distinct blocks of DEM were positioned without any interaction. The simulations proceeded through two phases: a compression and a shearing phase. In the compression phase, an external force is applied to bring the two DEM blocks into contact, while in the shearing phase, a constant velocity is applied at the top of the DEM. During the shearing phase, a vertical boundary condition was imposed, while the bottom of the DEM remained fixed. Figure 3.1 illustrates the system's geometry, with pressure control on the left and displacement control on the right. The system was sheared at a constant velocity of $v = 0.01c$, with c the wave celerity in one-dimension, and various external pressures are considered. All simulations in this chapter were conducted using LAMMPS software [89], and visualized with OVITO software [87].
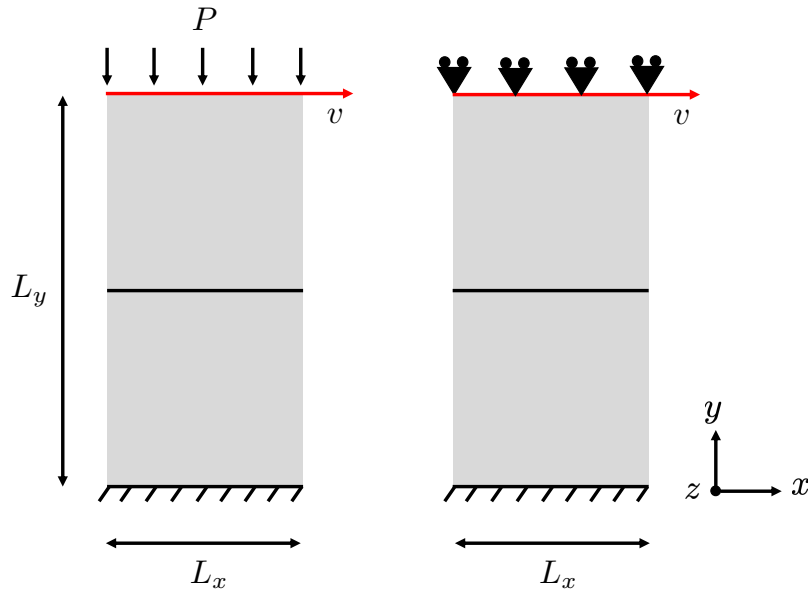
Figure 3.1: Schematic of the DEM system under pressure control on the left and displacement control on the right.

3.3 Results

To assess the influence of boundary conditions on the evolution of the third-body, we examine both the shear stress σ_{xy} resulting from the third-body movement, and the evolution of the third-body thickness. The shear stress is measured at the top particles of the system. The concept of a third-body can be defined in two ways. The first way consists of determining the third-body as the region where voids exist, due to the wear process. We consider that if the density drops below 5%, it signifies the presence of a void and, consequently, defines the third-body. The thickness of the third-body is then determined, based on the lower and upper position of the voids. We refer to this approach as the *Density* based third-body measurement. The second approach involves determining the third-body based on the rearrangement of particles. This concept is illustrated in Figure 3.2, where boundary particles are represented in gray, bottom particles in purple, and top particles in orange. The height of the third-body is determined by identifying the lower position of the top (orange) region and the higher position of the bottom (purple) region. We refer to this method as the *Migration* based third-body measurement.

(a)   (b)
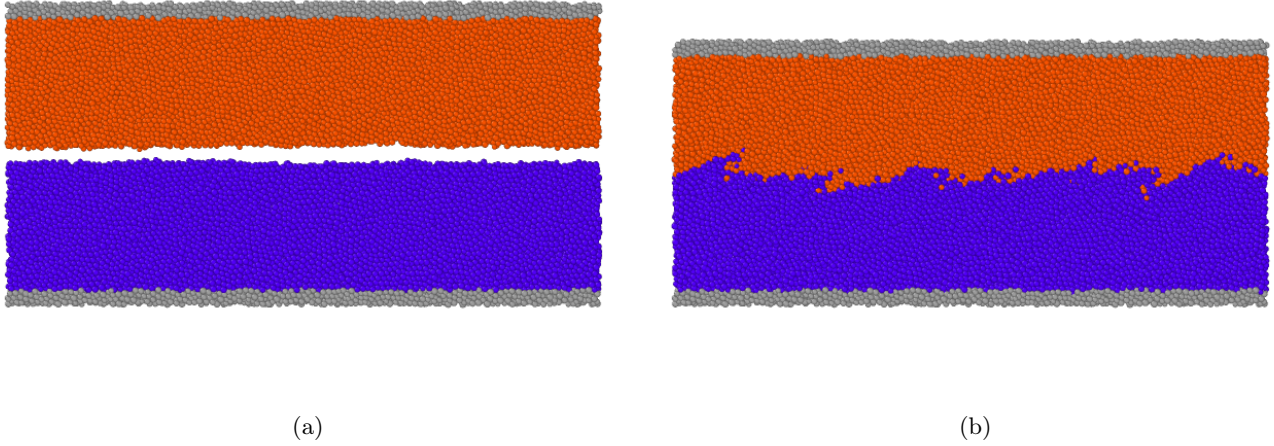
Figure 3.2: In both images, the particles are color-coded by type. Boundary conditions are shown in gray, bottom particles in purple, and top particles in orange. The left side represents an initial step, while the right side represents a final step.

3.3.1   Pressure control

3.3.1.1   Influence of tensile strength at a given pressure

A constant pressure of 100MPa is maintained on the top of the DEM while shearing at a steady velocity v. By adjusting the tensile strength parameter, we modeled three distinct third-body regimes as observed by Mollon [70] and Pham-Ba and Molinari [75]: a mixed regime at a tensile strength of $0.1E$ (Figure 3.3 - top), a debris-rolling regime at a tensile strength of $0.11E$ (Figure 3.3 - middle), and a shear-band regime at a tensile strength of $0.2E$ (Figure 3.3 - bottom).

$$\sigma_{\mathrm{n}} = 0.1E$$

(a)

$$\sigma_{\mathrm{n}} = 0.11E$$

(b)

$$\sigma_{\mathrm{n}} = 0.2E$$

(c)
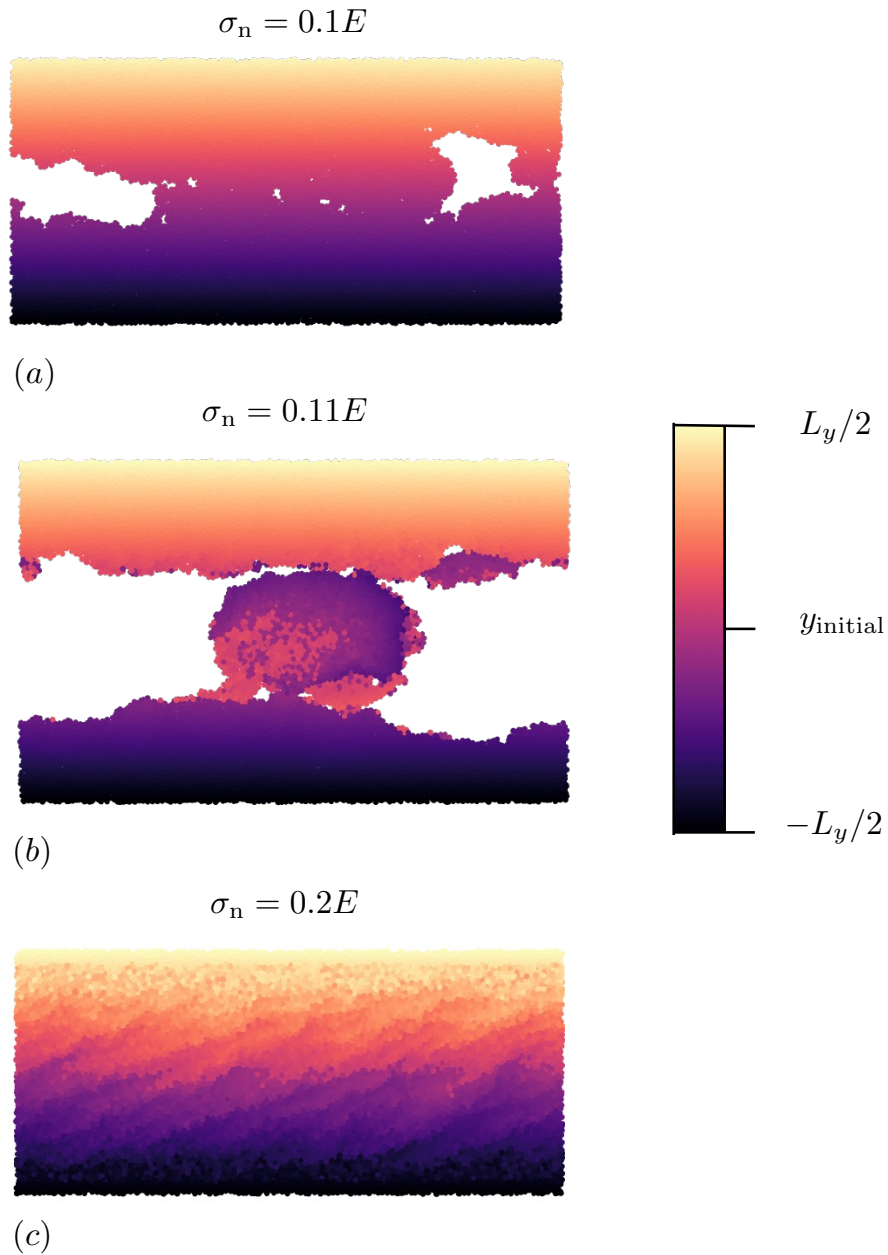
Figure 3.3: Initial position of the particles in the y-direction for a DEM box of height $50d_0$. (a) shows a mixed regime at a tensile strength of $0.1E$, (b) depicts a wear debris regime at a tensile strength of $0.11E$, and (c) illustrates a shear band regime at a tensile strength of $0.2E$.

In Figures 3.4a, 3.4b, and 3.4c, are represented the shear stress σ_{xy} resulting from the third-body movement for tensile strengths of $0.1E$, $0.11E$, and $0.2E$ respectively. Notably, the peak stress σ_{xy} increases with the tensile strength σ_{n} in all cases. These

plots show distinct stages: the initial compression phase before the vertical black line, followed by an elastic load. Analyzing the last stage provides insights into the friction evolution. Figure 3.4b corresponds to the scenario where debris forms without the intermediate mixed regime, the resulting stress σ_{xy} is minimal, indicating low friction. When a mixed regime precedes wear formation (Figure 3.4a), higher final stress levels are observed, suggesting a higher value of friction. Finally, in the case of a shear band (Figure 3.4c), the stress maintains the elastic peak value, indicating the highest friction among the three scenarios. This aligns with expectations: shear bands have the highest friction, followed by mixed regimes, and then debris rolling. It can be observed that the system's height does not appear to influence the stress (σ_{xy}) and, consequently, the friction within these three scenarios.

(a)

(b)

(c)
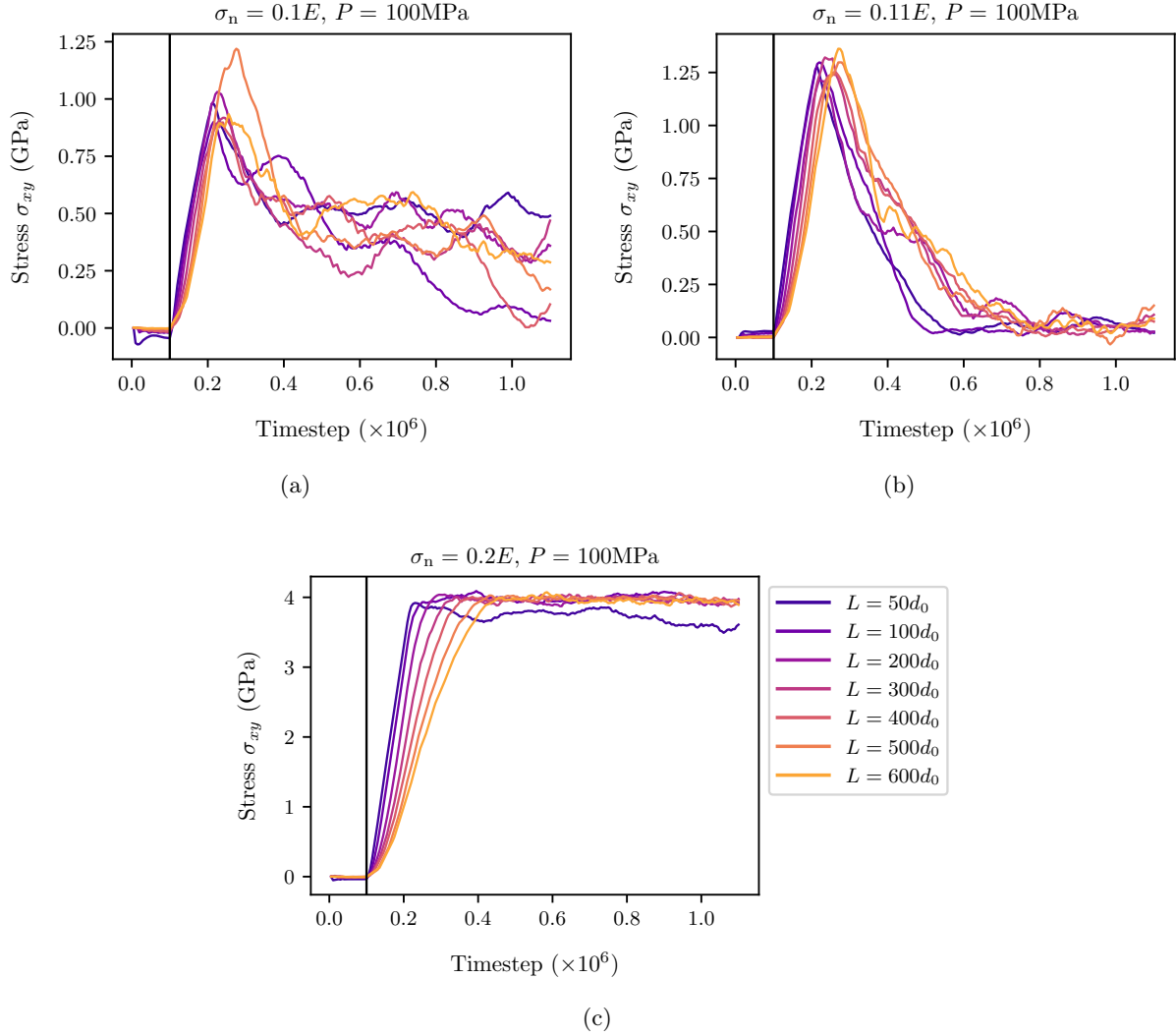
Figure 3.4: Evolution of the shear stress σ_{xy} under force control at an external pressure of 100MPa and different tensile strengths. (a) shows the evolution for a mixed regime at a tensile strength of $\sigma_{\mathrm{n}} = 0.1E$, (b) depicts the evolution for a debris rolling regime at a tensile strength of $\sigma_{\mathrm{n}} = 0.11E$, and (c) represents the evolution for a shear band regime at a tensile strength of $\sigma_{\mathrm{n}} = 0.2E$.

In Figures 3.5a, 3.5b, and 3.5c, are represented the third-body thickness evolution through time for tensile strengths of $0.1E$, $0.11E$, and $0.2E$ respectively. The time axis was shifted so that the initiation of the third-body growth is the origin, which compensates the distinct starting times associated with each DEM height. In Figure 3.5a, 3.5b the third-body thickness is evaluated using the *Density* based third-body measurement, while in Figure 3.5c the third-body thickness is evaluated using the *Migration* based measurement. In Figure 3.5a, 3.5b the third-body thickness evolves and grows over

time, however the system's height does not appear to influence the third-body thickness. In Figure 3.5c it can be observed that for the DEM height ranging from $100d_0$ to $600d_0$, the higher the DEM is, the lower the third-body thickness is. It should be noted that the smallest DEM $50d_0$ does not follow this trend. Thus, for a tensile strength of $0.2E$, the DEM height impacts the third-body thickness evolution.
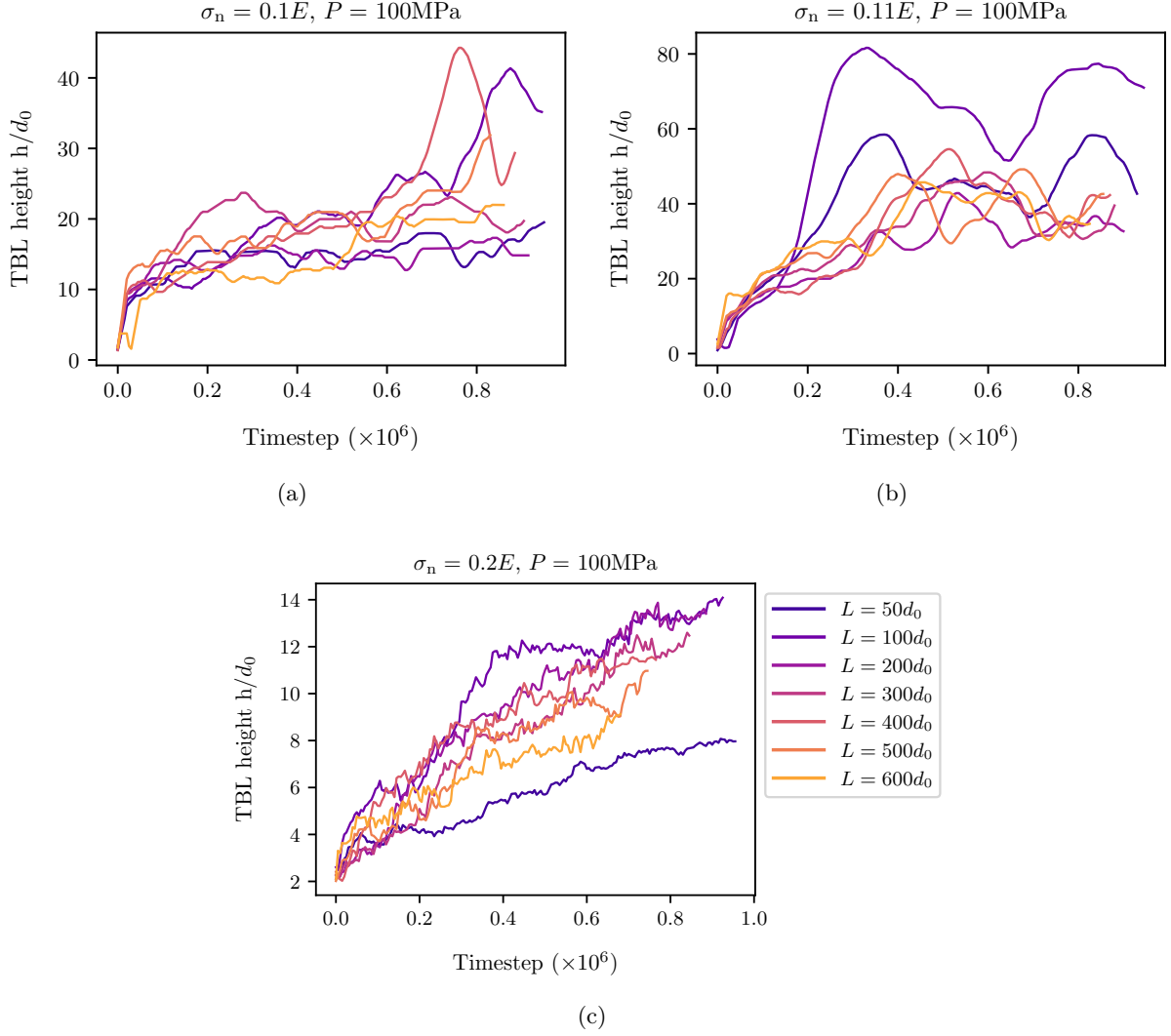
Figure 3.5: Third-body layer (TBL) thickness evolution under force control at an external pressure of 100MPa and different tensile strengths. Figure (a) shows the evolution for a mixed regime at a tensile strength of $\sigma_n = 0.1E$. Figure (b) depicts the evolution for a debris rolling regime at a tensile strength of $\sigma_n = 0.11E$, and Figure (c) represents the evolution for a shear band regime with a tensile strength of $\sigma_n = 0.2E$. For (a) and (b), the *Density* based approach is used, while for (c), the *Migration* based approach is employed.

3.3.1.2 Influence of external pressure at a given tensile strength

We will now consider different external pressures at a tensile strength of $0.1E$. We examine pressures of 100MPa (shown in Figure 3.7a), 200MPa, and 500MPa. Figures 3.6a and 3.6b show the stress σ_{xy} for pressures of 200MPa and 500MPa, while Figures 3.6c and 3.6d present the third-body thickness for the same pressures. In Figure 3.6c, the thickness of the third-body is computed using the *Density* based measurement, while in Figure 3.6d, it is evaluated using the *Migration* based measurement.

At 200MPa, we observe higher stress levels for larger boxes ($500d_0$, $600d_0$) compared to the smallest DEM heights ($50d_0$, $100d_0$). The stress pattern at the intermediate DEM heights does not align with an anticipated trend between the smallest and largest DEM heights. The contrast between the smallest and highest DEM heights reveals a distinction: a debris rolling formation occurs for the smallest DEM height, while a mixed regime is observed for the largest one. Concerning the third-body thickness, smaller boxes ($50d_0$, $100d_0$) exhibit larger thickness, while larger boxes ($500d_0$, $600d_0$) show smaller thickness.

At 500 MPa, we observe different trends for the DEM heights ranging from $50d_0$ to $300d_0$, and the highest one ($400d_0$, $500d_0$, $600d_0$). For the DEM heights ranging from $50d_0$ to $300d_0$, the stress remains constant after the peak before decreasing for $50d_0$ and $200d_0$ after 800,000 time steps. The plateau at $200d_0$ shows a smaller value compared to the other smallest and intermediate DEM heights. For the highest DEM heights, the stress decreases after the peak before increasing again. The DEM heights ranging from $50d_0$ to $300d_0$ reveal a shear band regime, while the highest DEM height leads to a mixed regime. Regarding the third-body thickness, we observe a clear dependence of the DEM height on its evolution. For DEMs with greater heights, the third-body thickness is higher compared to smaller DEM systems.

At a tensile strength of $0.1E$, our analysis indicates that the influence of DEM height on friction and the third-body regime is not clearly discernible at a pressure of 100MPa. However, at pressures of 200MPa and 500MPa, there appears to be a significant impact of DEM height on the third-body regime, height and friction. Therefore, under pressure-controlled conditions, the DEM height can influence the behavior of the third-body.
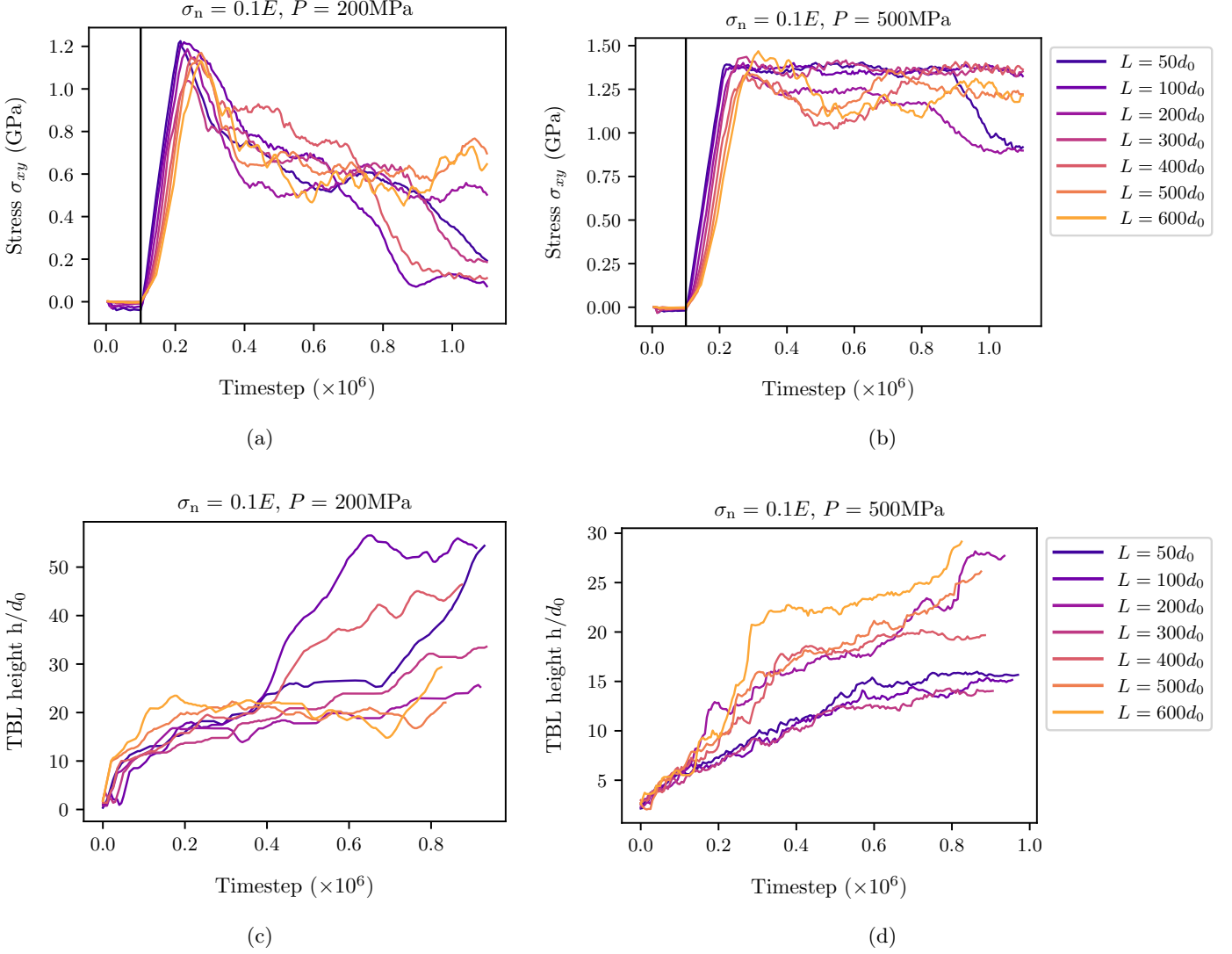
Figure 3.6: Third-body layer (TBL) evolution under force control at a tensile strength of $0.1E$ and different external pressures. (a) and (c) show the shear stress σ_{xy} and third-body thickness for an external pressure of 200 MPa, indicative of a debris-rolling or mixed regime depending on the DEM height. (b) and (d) illustrate the evolution of shear stress σ_{xy} and third-body thickness over time for a 500 MPa pressure, corresponding to a mixed or shear band regime, also dependent on DEM height.

3.3.2 Displacement control

Rollers were introduced during the shearing phase instead of maintaining a constant pressure on the top surface. Initially, the system underwent compression at a pressure of 100MPa. Similar to the pressure control scenario, we studied the third-body behavior at tensile strengths of $0.1E$, $0.11E$, and $2E$. At tensile strengths of $0.1E$ and $0.11E$,

a continuous mixed regime persisted until the end of the simulation. However, at a tensile strength of $0.2E$, adhesion led to the formation of a crack that extended to the boundaries, resulting in particles reaching the box size length L_x. This shows the limit of our simulation with a box length L_x under these specific conditions.

In Figures 3.7a and 3.7b, the stress σ_{xy} is depicted for tensile strengths of $0.1E$ and $0.11E$ respectively. Notably, both cases exhibit high friction due to their mixed regimes. Additionally, it can be observed that the height of the system affects the measured shear stress σ_{xy}, with larger systems resulting in lower shear stress as particles have more space to rearrange. The DEM configuration with a height of $500d_0$ exhibits a distinctive behavior not observed in other curves. At a tensile strength of $0.1E$, this configuration demonstrates zero friction. Due to the large size of the DEM, particles were able to rearrange, creating a void between the two blocks. Under displacement control, this void remains irreversible, unlike in a pressure-controlled scenario. Note that the random organization of particles may also be a factor, as it is observed for a length of $500d_0$.

In Figures 3.7c and 3.7d, the third-body thickness is depicted for tensile strengths of $0.1E$ and $0.11E$ respectively. In Figure 3.7d, the third-body thickness is determined using the *Density* based measurement, while in Figure 3.7d, the *Migration* based measurement is employed. In Figure 3.7c, there is no apparent dependence of the DEM height on third-body thickness, whereas in Figure 3.7c (excluding $500d_0$), a clear dependence of the DEM height on third-body thickness evolution is observed. Larger systems permit larger shear band formation.

Hence, under identical tensile strength, constant shearing velocity, and initial pressure conditions, we observe different behaviors in the third-body for pressure control versus displacement control cases. In the pressure control scenario, three distinct regimes were exclusively observed, while in the displacement control scenario, only the shear band and mixed regimes were present. In both cases, the DEM height significantly influences the shear stress/friction of the third-body and its thickness evolution.
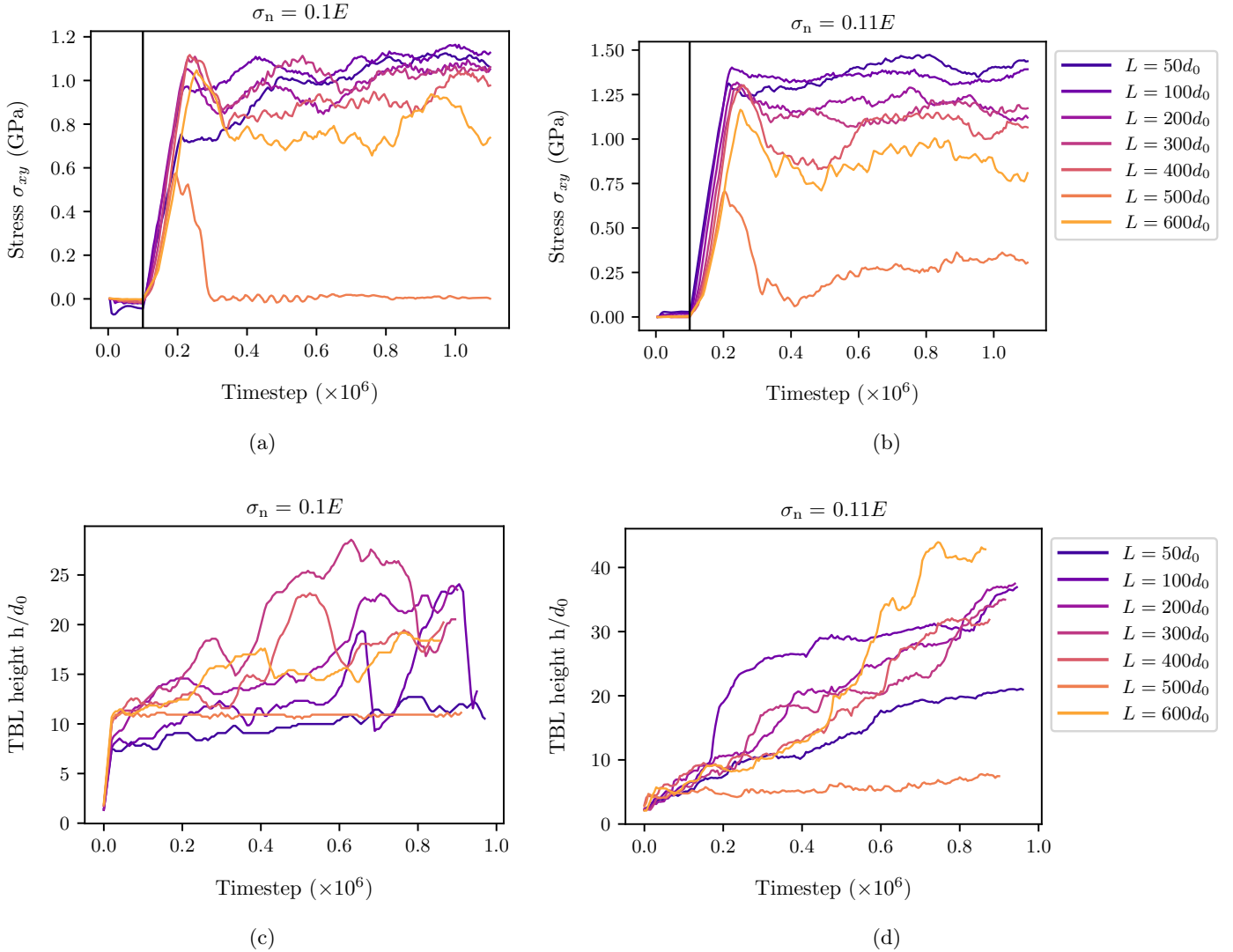
Figure 3.7: Evolution of the third-body layer (TBL) under displacement control with an initial compression of 100MPa and different tensile strengths. (a) and (c) represent the evolution of the shear stress (σ_{xy}) and the third-body thickness through time, at a tensile strength of $0.1E$ corresponding to a debris rolling or a mixed regime depending on the DEM height. (b) and (d) show the evolution of the shear stress (σ_{xy}) and the third-body thickness through time, at a tensile strength of $0.11E$ corresponding to a mixed or shear band regime depending on the DEM height.

3.3.3 Sub-system boundary conditions

When studying third-body formation, employing a larger system enables a more accurate representation of the materials undergoing abrasion. Yet, some researchers have opted for examining subsystems and applying the same boundary conditions as in larger

systems, as referenced [70, 75]. Thus, assessing the viability of maintaining identical boundary conditions in a subsystem is essential. We measured the displacement DY and the stress σ_{yy}, within a cross-section on the upper DEM block. This cross-section is positioned at a distance $40d_0$ from the interface. Because the DEM height of $50d_0$ does not meet the necessary dimensions for this specific cross-section, it has been excluded from our study. The cross-section represents the upper boundary of the studied subdomain. These measurements were conducted under a force control system with an external pressure of 100MPa and a displacement control system initially compressed at 100MPa. The tensile strength considered is $\sigma_n = 0.1E$.

Figure 3.8a and 3.8c show the evolution of the displacement and the stress σ_{yy} in the cross-section for the system under force control. Notably, both the stress σ_{yy} and the displacement DY exhibit irregular patterns in this cross-section. Consequently, for a system under pressure control, no clear interpretation of the subdomain boundary conditions can be provided. Therefore, applying either force control or displacement control boundary conditions to the subdomain would not be accurate.

Figures 3.8b and 3.8d depict the evolution of the displacement DY and the stress σ_{yy} in the cross-section for the system under displacement control. Both stress and displacement exhibit irregular patterns, similar to the previous case under force control. Thus, a similar interpretation can be made. Applying either force control or displacement control boundary conditions to the subdomain would lack accuracy.
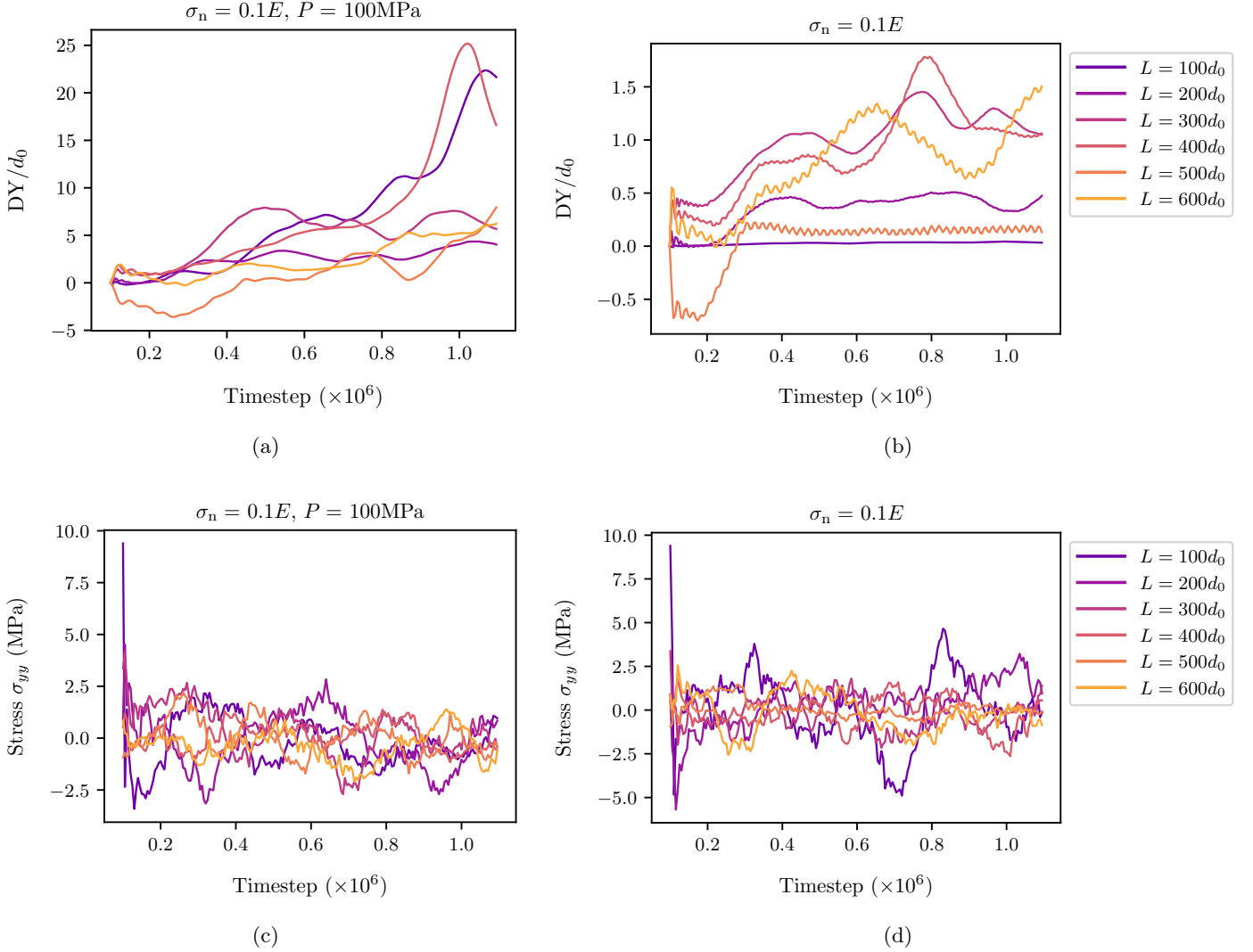
Figure 3.8: Evolution of a cross-section in the upper DEM block over time. (a) and (b) illustrate the evolution of the vertical displacement (DY) under force control and displacement control, respectively. (c) and (d) show the evolution of stress σ_{yy} under force control and displacement control, respectively.

3.4 Conclusion

In this exploratory study, we have demonstrated the impact of boundary conditions and DEM height on the evolution of the third-body.

In pressure control, adjusting the tensile strength for a system under a pressure of 100MPa allowed us to replicate the three distinct regimes observed in a third-body: a mixed regime ($\sigma_n = 0.1E$), debris rolling ($\sigma_n = 0.11E$), and a shear band ($\sigma_n = 0.12E$). By varying both tensile strength and applied pressure, we noted that the DEM height

had an impact on the shear stress/friction of the third-body, as well as its thickness.

In displacement control, with the system initially compressed at 100MPa, we replicated the mixed regime and the shear band regime, although the debris rolling regime was not reproduced. By varying the tensile strength, we observed an influence of the DEM height and the tensile strength of the third-body.

The third-body is a complex system, and it is evident that both boundary conditions and height play a role in influencing its evolution. However, determining the precise manner in which they affect the third-body evolution remains challenging.

Additionally, we analyzed the boundary conditions of a subdomain within a larger domain governed by either force or displacement control. We showed that applying force or displacement conditions to the subdomain, similarly to the large domain, would be inaccurate to represent the complexity happening in the subdomain.

Based on these results, modeling the entire system is essential to accurately capture the evolution of the third-body. This may involve modeling a large system with granular material to represent experiments, such as a pin-on-disc setup. Given the high computational cost associated with DEM, there is a need for an alternative approach that can model large domains in order to capture the complexity of third-body evolution while minimizing computational costs. The FEM-DEM bridging coupling, introduced in the next chapter, proves to be a promising solution in this regard.

Chapter 4

Bridging coupling: application to amorphous materials

Disclaimer

This chapter is in part reproduced from the article: Manon Voisin-Leprince, Joaquin Garcia-Suarez, Guillaume Anciaux, Jean-François Molinari, "Finite element method–discrete element method bridging coupling for the modeling of gouge" (2022), *International Journal for Numerical Methods in Engineering* [91]. All authors have granted their permission.

Contents

4.1 Introduction

In Chapter 3, we illustrated how the height of the tribo-system and the chosen boundary conditions affect the evolution of the third-body, including its regime, thickness, and frictional properties. This highlights the need to accurately represent the surrounding

regions for a correct third-body modeling. In the previous chapter, we employed the DEM to model both the third-body and the surrounding regions, which proved to be computationally expensive. To address this challenge and facilitate the modeling of large systems, we propose a FEM-DEM coupling method. In this approach, DEM is employed for modeling the third-body where discretization is necessary, while the FEM is applied to represent the surrounding regions as continuum domains, thereby reducing computational time. Unlike the previous chapter, this chapter considers a dry gouge without any cohesion, which has also significant applications in geomechanics models [1, 43, 46, 77, 93].

As introduced in Chapter 2, Section 2.2, several types of coupling approaches exist and have been extensively studied for coupling Molecular Dynamics (MD) with FEM. However, DEM/FEM coupling differs from MD/FEM coupling on several aspects and brings unique challenges. First, the targeted particles obey different interaction laws: atoms interact through energy potentials (leading to both attractive and repulsive forces that are function of the distance between particle centers), while discrete particles interact according to macroscopic contact laws (short range interactions), which require the consideration of rotational degrees of freedom. A local FEM formulation, which does not account for pointwise rotation and torques, cannot be coupled to a DEM that considers angular velocities. To do so, one would need to use other FEM formulations, such as the *Cosserat* [30]. For the sake of simplicity, this was not investigated in this chapter, where only small deformations are considered. Second, MD is more often than not used with a well-organized crystal structure, while DEM considers generally an amorphous structure, which leads to heterogeneous effective elastic properties. These differences make the extension of MD/FEM to DEM/FEM a far-from-trivial task. Several approaches have been put forward to couple continuum and discrete (DEM) domains, including overlapping [24, 25, 94, 98] and edge-to-edge methods [16, 47, 68].

In this chapter, we consider the FEM to be an extension of the gouge. In that case, the DEM and FEM have to behave similarly. An overlapping method allows achieving this, even with large finite element sizes, while an edge-to-edge cannot, as the random placement of the spheres leads to a variation of constitutive behaviors. Therefore, to couple FEM and DEM, we utilize the *bridging* method [97] (see Chapter 2.2.2). Studying a three-dimensional amorphous arrangement of DEM particles (e.g., a gouge) subjected to a confinement pressure remains a subject to explore. The confinement pressure has a destabilizing effect, which challenges the enforcement of Lagrange multipliers and results in *ghost forces* of a new kind, which have not been previously reported in the literature. In this chapter we demonstrate the emergence of these spurious effects, and provide a simple modification of the *bridging* method allowing to cancel all *ghost forces* both for a weak and a strong formulation of the constraints. As a by-product, this work also provides simple guidelines to the multiscale modeling of a gouge at depth.

Section 2.2.2 presents two FEM-DEM coupling methods. The first one enforces a strong coupling and is an extension of the *bridging* method [97] developed for MD/FEM

to DEM/FEM. The second one considers a weak formulation of the Lagrange constraint. In Section 4.2, the behavior of a granular material is studied to determine its effective elastic properties and help choose the finite-element mesh size at the DEM/FEM interface. Section 4.3 compares the coupling strategies in order to determine the most appropriate one for stability. Then, in Section 4.4, the passing through of pressure and shear waves is analyzed for different wave frequencies.

4.2   Granular medium and constitutive behavior

In order to test the presented coupling approaches, we consider a system where the continuum and discrete domains have a matching material behavior within the range of small (elastic) deformations. It is therefore necessary to determine the macroscopic elastic properties of the granular ensemble.

The granular medium represents a dry gouge, with no adhesion between the particles, and subjected to a specific confinement pressure coming from the surrounding medium. Several tri-periodic DEM box sizes, are generated to determine if the granular material can be considered as linear elastic, and to observe if the extracted material properties are converging when the sample size becomes large enough. The material properties of the FEM and the mesh size at the FEM-DEM interface will be chosen based on these single scale DEM results, with the ambition to avoid any mismatch in the material response between the coupled domains.

4.2.1   DEM sphere packing

Nine different box sizes, with periodic boundary conditions in the three directions, are considered. In order to account for variability due to the random particle distribution, twenty samples have been generated for each box size. The DEM simulations are run using LAMMPS software [89], with DEM grains parameters corresponding to glass bead values as described in Table 4.1. Glass beads are widely used as a model material in simulations [5, 43] and in experiments aiming to represent the behavior of granular materials [40, 60].

The grains interact through the Hertz-Mindlin contact law [57, 65] (details on the contact law are given in Section 2.1.1, Eq. 2.4). Two grain sizes were considered, with an average diameter $d_0 = 3$ mm. The dimensionless stiffness is defined as $\kappa = (E^*/\sigma_n)^{2/3}$ with $E^* = E/(1 - \nu^2)$ [3, 4] and is characterizing the equilibrium overlap between particles δ, i.e. $\delta/d_0 \simeq \kappa^{-1}$ [4]. To be in the so-called rigid limit, $\delta \ll d_0$, it is necessary to have $\delta/d_0 = \kappa^{-1} \ll 1$. In our case $\kappa = 495 \gg 1$, for which the granular assembly can be considered fairly stiff.

Note that a too high overburden pressure could lead to a non-elastic behavior. Agnolin and Roux [4] observed an elastic behavior until a pressure of 10 MPa. As we are considering an overburden pressure of $\sigma_n = 5$ MPa, it is safe to assume an elastic contact

behavior. The time step is chosen according to the criterion $\Delta t < 0.14\sqrt{m_{\min}/k_{\max}}$ [73], with $m_{\min}$ the minimum grain mass and $k_{\max}$ the maximum normal contact stiffness.

Young's modulus, E	50 GPa
Grain density, ρ	2500 kg/m^3
Poisson's ratio, μ	0.3
Overburden pressure, σ_{n}	5 MPa
Grain minimal diameter, $d_{\min}$	$2.5 \cdot 10^{-3}$ m
Grain maximal diameter, $d_{\max}$	$3.5 \cdot 10^{-3}$ m
Grain mean diameter, d_0	$3 \cdot 10^{-3}$ m
Friction between grains, μ_{g}	0.5
Normal stiffness, K_{n}	$3.663 \cdot 10^{10}$ N/m^2
Tangential stiffness, K_{t}	$4.5249 \cdot 10^{10}$ N/m^2
Normal viscoelastic damping constant, Γ_{n}	0.2 (m·s)$^{-1}$
Tangential viscoelastic damping constant, Γ_{t}	0.1 (m·s)$^{-1}$
Time step, dt	10^{-8} s

Table 4.1: DEM grain parameters. See Section 2.1.1 for the definitions of $K_{\mathrm{n}}, K_{\mathrm{t}}, \Gamma_{\mathrm{n}}$ and Γ_{t}. The damping coefficient Γ_t corresponds to the default value of LAMMPS ($\Gamma_{\mathrm{t}} = \frac{1}{2}\Gamma_{\mathrm{n}}$).

To generate the DEM samples, the initial boxes are first filled with particles such that they occupy a volume fraction of 60%. Then, the boxes are compressed in the three directions and relaxed, iteratively, until an overburden pressure of 5MPa is reached. During the process, the final equilibrium conditions are approached as the particles' excess kinetic energy is dissipated via viscous damping forces. For a box size of $12d_0$, approximately three million time steps are necessary to reach equilibrium at the desired overburden pressure.

4.2.2 Homogeneous elastic properties

The boxes containing the particles are then subjected to positive and negative displacements equivalent to particular strain states, where each component (ε_{xx}, ε_{yy}, ε_{zz}, γ_{xy}, γ_{xz}, γ_{yz}) is evaluated separately (see elastic examples of LAMMPS [89]). After each displacement, the boxes are relaxed, before measuring the overall stress. The 36 elastic tensor coefficients (C_{ij}) are computed with the corresponding applied strain direction (an average of positive and negative strains is performed to get a better accuracy). The Zener [99] anisotropy index $2C_{44}/(C_{11} - C_{12})$ can be extracted as a measure of anisotropy.

Figure 4.1a shows that this anisotropy coefficient is very close to unity for a box size larger than $6d_0$. This implies that for a large enough box, our granular samples can be considered isotropic. Figure 4.1b shows the elastic tensor of a box of length $12d_0$ for a specific realization. The structure of the elastic tensor confirms the isotropy of the granular medium.

(a)

(b)
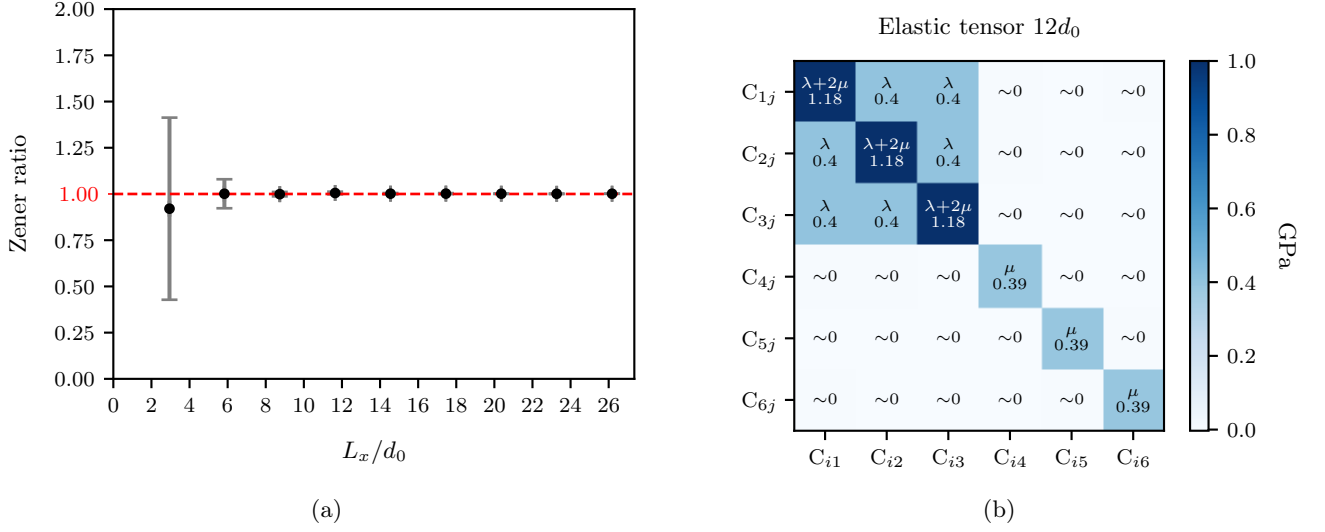
Figure 4.1: (a) represents the Zener anisotropy index in terms of the number of particles per box length L_x/d_0. (b) represents the elastic tensor of the box of length $12d_0$ at a specific realization. The vertical error bars represent the standard deviation due to the 20 box generations per box length.

The elastic properties (Young's modulus, bulk modulus, shear modulus and Poisson's ratio) are then determined. In Figure 4.2a, the Young's modulus is shown as a function of the number of particles per box length, and reaches a plateau for box sizes larger than $12d_0$. The shear modulus (Figure 4.3a) and the bulk modulus (Figure 4.3b) are also following the same trend, while the Poisson's ratio (Figure 4.2b) and density (Figure 4.3c) appear practically constant with respect to the box size. The tests conducted suggest a convergence of the elastic properties for box sizes larger than $12d_0$. Therefore, any linear-elastic continuum domain discretized using a characteristic mesh size equal or larger than $12d_0$ should display the same constitutive behavior (see Table 4.2 for numerical values) than the homogenized DEM samples.

Young's modulus, E	0.977 GPa
Density, ρ	1543 kg/m^3
Poisson's ratio, μ	0.255
Overburden pressure, σ_n	5 MPa

Table 4.2: Effective constitutive parameters for a granular domain. Such values will be employed as material properties for the FE simulations.

63

(a)

(b)
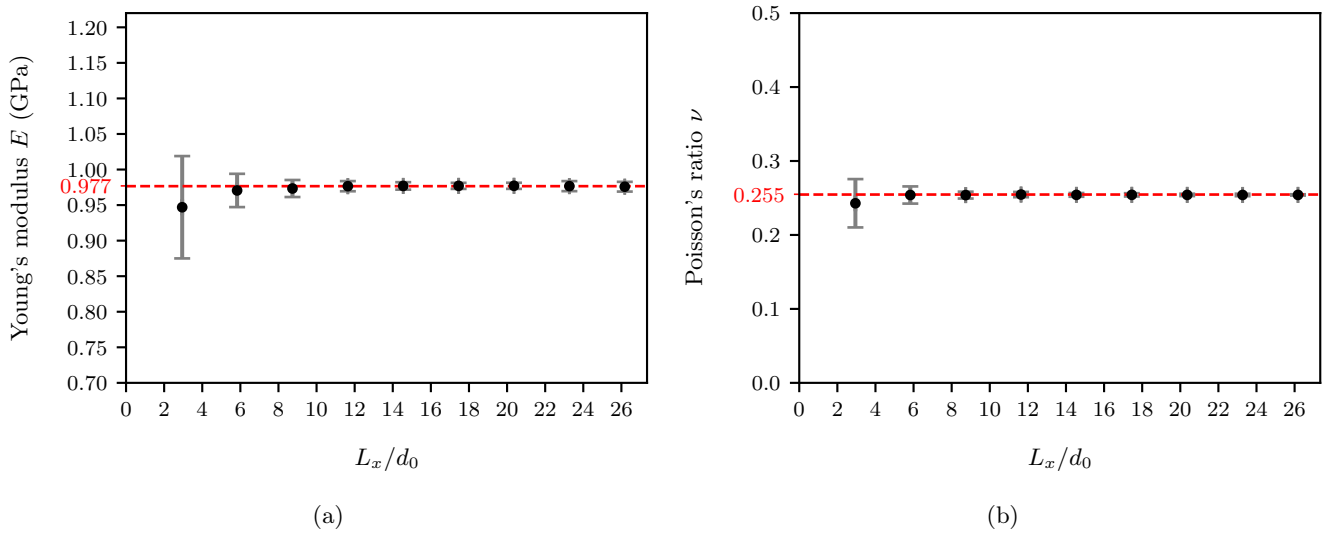
Figure 4.2: Convergence of elastic properties as the sample size becomes larger. (a) shows the Young's modulus in terms of the number of particles per box length L_x/d_0. (b) shows the Poisson's ratio in terms of the number of particles per box length L_x/d_0. The vertical error bars represent the standard deviation due to the 20 box generations per box length.

(a)

(b)

(c)

Figure 4.3: (a) represents two shear moduli in terms of the number of particles per box length L_x/d_0. The first shear modulus (in black/grey) is computed using the expression $\mu = C_{44}$ and the second one (in blue) using $\mu = (C_{11} - C_{12})/2$. (b) shows the Bulk modulus, in terms of the number of particles per box length L_x/d_0. (c) shows the density, in terms of the number of particles per box length L_x/d_0. The vertical error bars represent the standard deviation due to the 20 box generations per box length.

4.3   Simulations of coupled FEM-DEM

4.3.1   Geometry

The geometry considered in all the following coupled simulations is that of an elongated 3D bar of constant section, made of a DEM region surrounded by two finite-element

meshes, as presented in Figure 4.4. According to the results from the previous section, finite elements with a characteristic size $h \approx 12d_0$ have elastic properties matching with DEM granular packings. The DEM dimensions are chosen to ensure at least two elements, $\approx 24d_0$, in the section (x and z directions), a gouge thickness $\approx 20d_0$ (the unconstrained DEM), and two bridging regions covering the length of one element along the y direction. The FEM dimensions are chosen in such a way that the dimensions in x and z match the DEM region, while the length of each FEM meshes are $\approx 400d_0$. Such a long bar will allow studying the propagation of large wave lengths. Periodic boundary conditions are imposed to the system in the lateral directions (x and z). As previously stated, the DEM particles are packed with a hydrostatic confinement pressure, which needs to be balanced with the FEM subdomains. This is achieved with eigen-strains pre-stressing the FEM domains. The concurrent coupling will be in charge of exchanging forces between interface nodes and particles. As will be discussed below, the efficiency of the proposed coupling approaches differ notably.
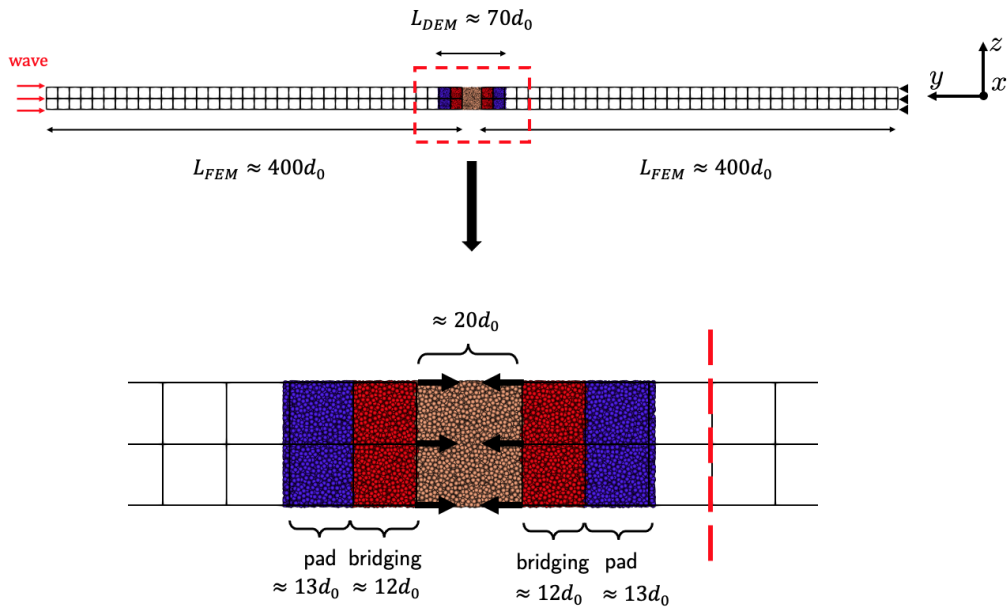
Figure 4.4: Schematic of the FEM-DEM coupling.

4.3.2 Strong/Weak coupling and ghost-force correction

The strong and weak coupling strategies (see section 2.2.2) have been implemented in the open-source LibMultiScale software [10–13].

To determine whether the strong or weak coupling is more appropriate, this coupled geometry is first considered with no added perturbation, and run over long simulation

times. Three different coupling set-ups, composed of three different DEM regions, have been tested t consider the effect of the amorphous structure. The displacement within a chosen cross-section in the FEM (indicated in red dashed line in Figure 4.4) is monitored in order to establish the performance of each coupling strategy. For the weak coupling, after a simulation time of $500,000$ time steps, a displacement noise is observed to be in the order of $10^{-5}\mathrm{m} \sim 10^{-2} \cdot d_0$ (Figure 4.5b), while it is in the order of $10^{-6}\mathrm{m} \sim 10^{-3} \cdot d_0$ (Figure 4.5d) for the strong coupling. Such spurious displacements will keep growing as a consequence of a lack of equilibrium in the coupling region, due to the imposed pre-stress. The applied eigen-strains, which induce forces on the free surface of the mesh where nodes should be associated with a vanishing energy weight, are at the origin of this issue. The approximations in the integration of the Lagrange constraint led to the equations presented in section 2.2.2, which precludes a null weight on the continuum interface. This becomes obvious when considering equations 2.28 and 2.32, where a division by the weighted mass ($\overline{M}$) is performed, forbidding a perfectly null weight. In Anciaux [11], it was shown that an adequate, non-zero, choice of the weight for these limiting nodes could also diminish wave reflections substantially, in the case of crystalline structures evolving around their ground state configuration. With the presented amorphous and pre-stressed configuration, the same coupling approach does not compensate well the interface forces, giving rise to *ghost forces*.

To balance these, a strategy similar to the one used by Shenoy et al. [84] has been employed: initial nodal forces were saved at the simulation onset, and then subtracted throughout the entire simulation. With this force correction, the weak coupling shows a diminished noise displacement in the order of $10^{-7}\mathrm{m} \sim 10^{-4} \cdot d_0$ (Figure 4.5a), and of the order $10^{-11}\mathrm{m} \sim 10^{-8} \cdot d_0$ (Figure 4.5c) for the strong coupling. Therefore, it appears that the strong coupling with ghost forces correction yields the most stable system, which will be used in the following section to study propagating waves through the coupling interface.
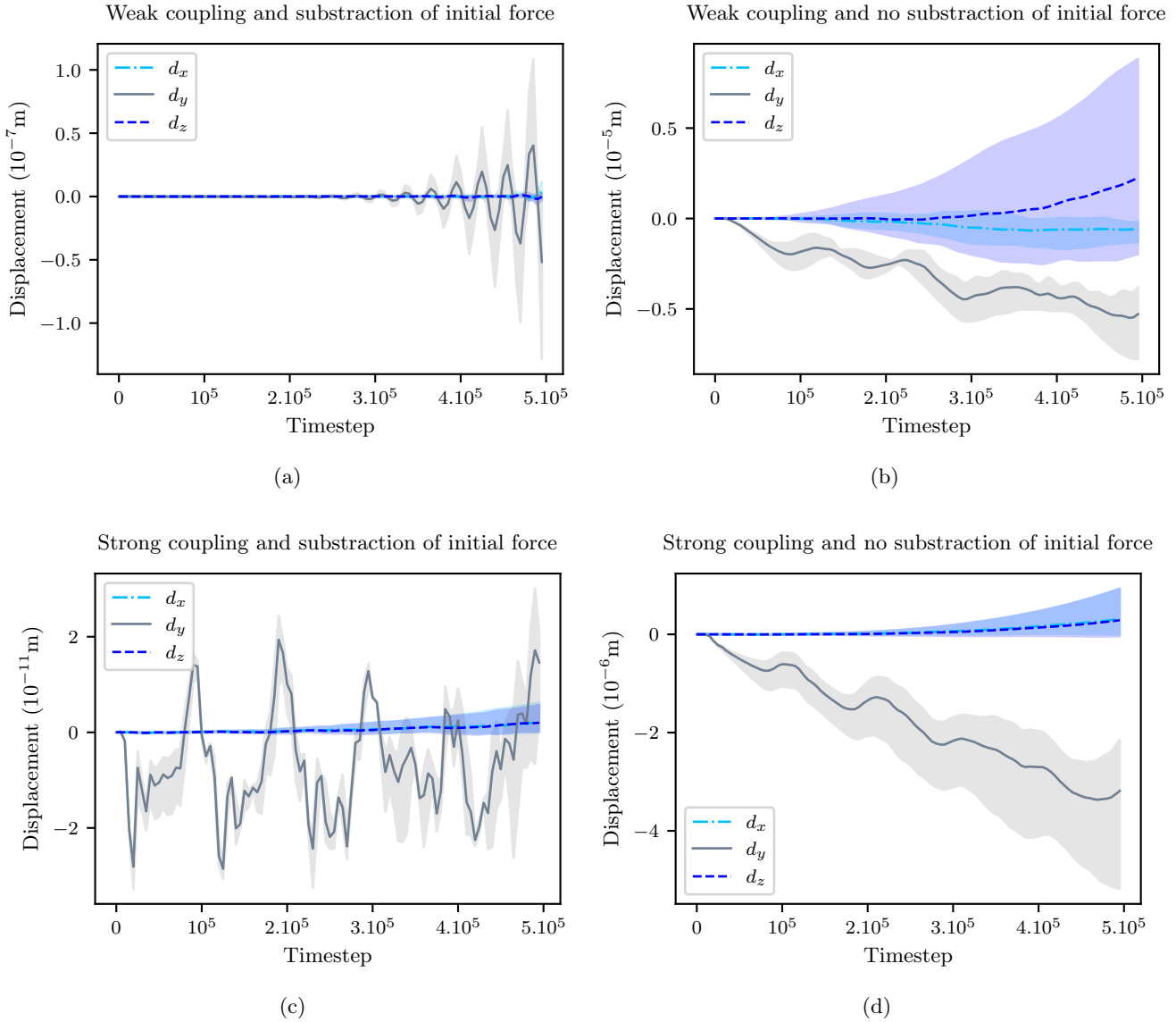
Figure 4.5: Testing different coupling strategies. (a, b) show the average displacement at a specific cross-section considering the weak coupling. (c, d) show the average displacement at a specific cross-section considering the strong coupling. (a, c) consider the subtraction of the initial force to correct ghost forces, while (b, d) do not. The shaded regions represent the minimum and maximum displacement values obtained through the three different simulations.

4.4   Waves passing through the coupling interface

4.4.1   Wave train characterization

Ricker [80] demonstrated that a seismogram can be decomposed into a succession of wavelets, which are nowadays called *Ricker wavelets*. To excite our coupled system and form a compressional wave propagating along the y direction, we impose through time a Gaussian displacement corresponding to a ricker wavelet:

$$u_y(t) = I \exp\left(-\frac{1}{2}\left(\frac{2\pi c(t - t_0)}{\lambda}\right)^2\right), \tag{4.1}$$

with c the velocity of the wave, λ its wavelength, I its intensity and $t_0 = \lambda/(2c)$.

The Fourier transform is used to analyze the spectrum of the wave:

$$\mathcal{F}[u_y(y)](k) = \frac{1}{\sqrt{2\pi}} \int_{-\infty}^{+\infty} u_y(y)e^{iky}\, dy \tag{4.2}$$

$$= \frac{1}{\sqrt{2\pi}} \int_{-\infty}^{+\infty} I \exp\left(-\frac{1}{2}\left(\frac{2\pi(y - ct_0)}{\lambda}\right)^2\right)e^{iky}\, dy \tag{4.3}$$

The Fourier transform has a Gaussian shape localized around the fundamental wavelength λ. If the fundamental wavelength λ is chosen to be much larger than the mean diameter of the particles d_0, all the harmonics of significant intensity that are contained in the spectrum will be much larger than the diameter of a particle d_0. Additionally, if a wavelength is larger than the mean diameter of the particles d_0, it will be experienced by the DEM grains as a smooth transition from one grain to its neighbors, and it will not trigger rearrangements of the fabric. Therefore, the DEM portion will undergo small deformations and will behave as a linear-elastic medium. Also, a large wavelength reduces numerical dispersion in the FEM.

Let us now derive a condition for a compressional wave to be considered low-amplitude. In what follows, let us note $\xi = \frac{2\pi}{\lambda}\left(y - c(t - t_0)\right)$. To quantify the maximum value of the strain, we apply the chain rule:

$$\varepsilon = \left|\frac{\partial u_y(y)}{\partial y}\right| = \left|\frac{\partial u_y(y)}{\partial \xi}\frac{\partial \xi}{\partial y}\right| \sim \frac{|u_{y,\xi}(y)|}{\lambda} \sim \frac{I}{\lambda}. \tag{4.4}$$

The condition for the continuum to remain linear and elastic is $\varepsilon \ll 1$ (small strains), which consequently leads to $I/\lambda \ll 1$. While this result was derived for compressional waves, a similar approach can be pursued for shear waves with identical conclusions.

4.4.2 Wave propagation

A wave propagation through the strong coupling system presented earlier (see Figure 4.4) will be monitored in order to characterize the artifacts produced by the coupling. A Ricker's wavelet is generated at the extremity of the left FEM portion, by applying the displacement given by Eq. 4.1 as a boundary condition. The propagation of the wave is studied for two different mesh sizes h: $12d_0$ and $3d_0$, for both compressional and shear Ricker waves. We consider two large wavelengths ($200d_0$, $400d_0$) and two small strains ($8.3 \cdot 10^{-4}$, $8.3 \cdot 10^{-5}$) for compressional and shearing waves. Table 4.3 summarizes the wavelengths, intensities, and strains of the generated waves. Considering the small intensities of the waves, the little friction occurring in the DEM does not influence the propagation. For all the conducted simulations, the displacement of the wave will be monitored within the cross-section at $y = 0.138$m. This cross-section is highlighted with a dashed red line in the Figure 4.4 in the case of element size $12d_0$.

Wavelength λ (m)	$200d_0$	$200d_0$	$400d_0$
Intensity I (m)	$5 \cdot 10^{-4}$	$5 \cdot 10^{-5}$	$1 \cdot 10^{-4}$
Strain ε	$8.3 \cdot 10^{-4}$	$8.3 \cdot 10^{-5}$	$8.3 \cdot 10^{-5}$

Table 4.3: Waves characteristics.
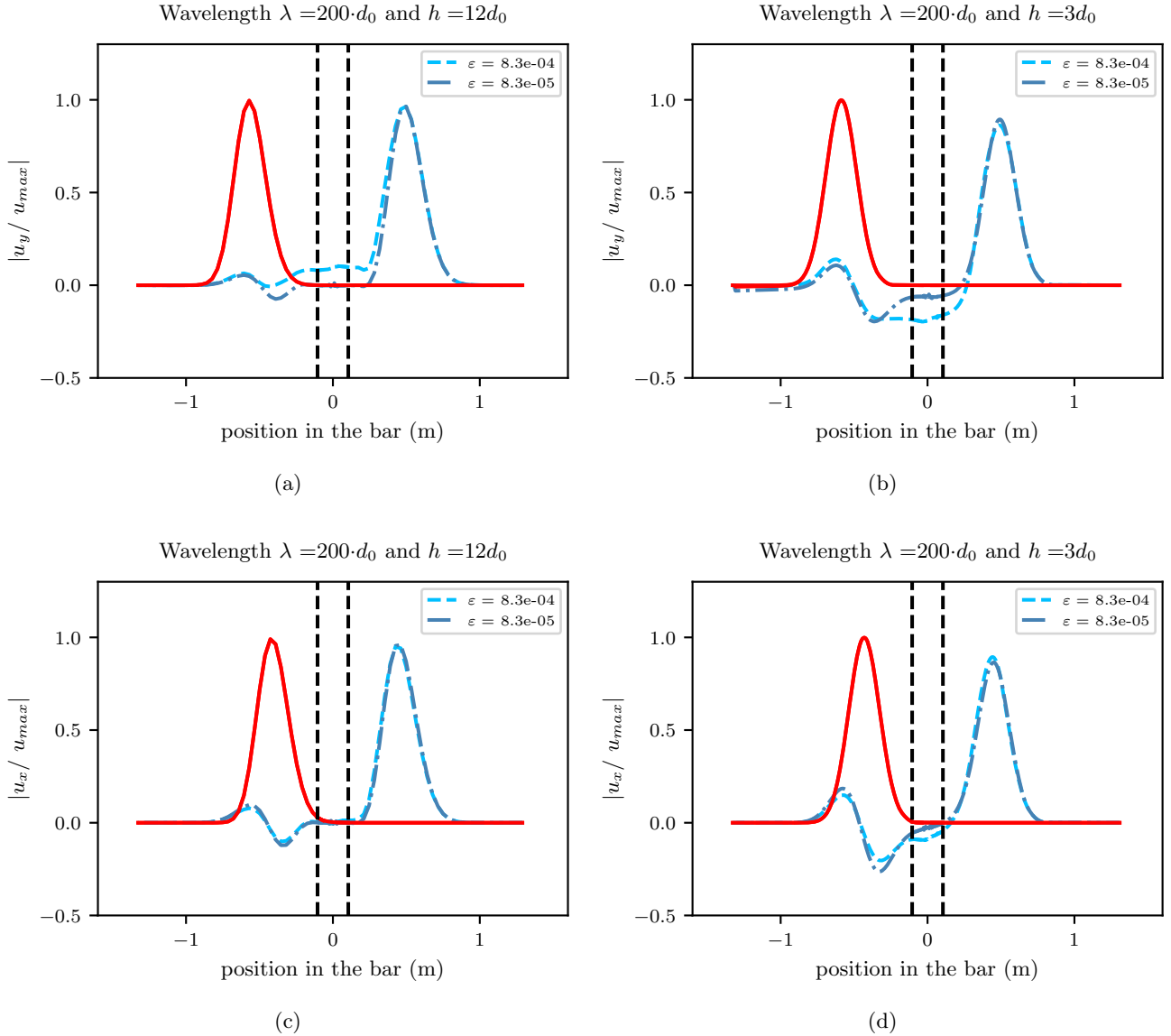
Figure 4.6: Waves passing through the coupling interface. (a, c) consider a characteristic mesh size of $12d_0$, while (b, d) consider a characteristic mesh size of $3d_0$. The top row figures (a, b) have been generated considering push waves, while the bottom row figures (c, d) have been generated considering shear waves. The red curves represent the waves before reaching the DEM, and the blue curves correspond to the waves after passing through the DEM. The dash vertical lines are visual guides for the location of the FEM-DEM interfaces.

In the case of compressional and shear waves for a large mesh size of $12d_0$, we observe that the intensity of the wave after passing the DEM is close to 1 for every strain (see Figure 4.6a, Figure 4.6c). This means that we have an almost-complete

transmission of the wave, regardless of its strain level. Contrariwise, for a mesh size of $3d_0$, we observe that the intensity of the transmitted wave is diminished by a small factor (~ 0.88), independently of the strain (see Figure 4.6b, Figure 4.6d). The less-accurate transmission of the wave in the case of the smallest mesh size $3d_0$ is due to the mismatch of material properties between FEM and DEM. In fact, it was shown in Section 4.2, that a mesh characteristic size greater than $12d_0$ is necessary to homogenize the elastic properties of the DEM. If this is not the case, the constitutive behavior varies among elements.

It can be observed that a reflected wave has been generated in all cases (see Figures 4.6a, 4.6b, 4.6c, 4.6d). In order to determine the origin of the reflected wave we pursue an analogy with MD/FEM coupling. It has already been observed in MD/FEM coupling [11] that a reflected wave emerges at the coupling interface. The dispersion relation that relates the wave frequency to its wavelength can differ between the MD and the FEM depending on the FE mesh size (Figure 2.8 in [11]). If the mesh size is equal to the distance between atoms, the dispersion relation will be the same. However, when the mesh size increases, MD and FEM domains admit different wave velocities for the same harmonic. This difference of propagation velocities (dispersion) creates the impedance contrast that is at the origin of the reflected wave. The same mechanism is at the origin of the reflected wave that is observed in our DEM/FEM simulations, the main difference being that the dispersion relation of the granular medium is much more convoluted than the simple 1D atomic chain that is used in the illustrative example of [11]. The intensity of the reflected wave can be reduced by increasing the wavelength, as the dispersion relation in both domains will be similar in the long-wavelength limit if the material properties of the homogenized granular medium are assigned to the continuum. By increasing the wavelength compared to the mesh size, we reduce the difference of wave speeds between the two domains and therefore reduce the intensity of the reflected wave.

In order to validate our discussion as to the origin of the reflected wave in the DEM/FEM coupled system, we study the propagation of two compressional waves, each with the small strain $8.3 \cdot 10^{-5}$, but with different wavelengths $(200d_0, 400d_0)$. The considered discretization used characteristic element sizes $12d_0$. Figure 4.7 shows the displacement of these two compressional waves in the system. In both cases, a reflected wave is created during the propagation through the coupling and DEM regions. Though, a higher reflected intensity is observed for $\lambda = 200d_0$, than for a wavelength $\lambda = 400d_0$. This indicates that the reflected wave is due to dispersion happening at the FEM-DEM interface, which is strongly dependent on the wavelength.

Intensity $I = 5.0\text{e-}05\text{(m)}$
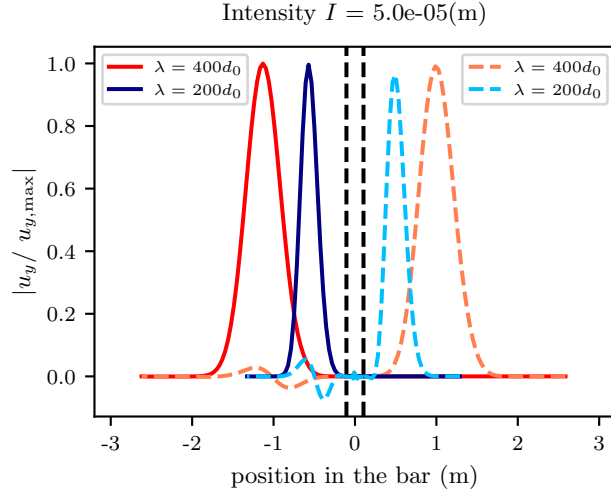
Figure 4.7: Transmission through the coupling interface of two compressional waves with $\lambda = 400d_0$ (red and light-dashed red for before and after the interface) and $\lambda = 200d_0$ (blue and dashed-light blue for before and after the interface). The dash vertical lines are visual guides for the location of the FEM-DEM interfaces.

To strengthen our analysis, we plot the *ct* diagrams for $\lambda = 200d_0$. Figure 4.8 shows the results for a large mesh size $12d_0$ and Figure 4.9 for a small mesh size $3d_0$. These *ct* diagrams show a better transmission of the compressional and shear waves for a large mesh size. One can nonetheless observe reflected waves in all cases.

Note that a residual displacement at the unconstrained DEM region is observed for a large mesh size $12d_0$, in the case of a compressional wave of strain $8.0 \cdot 10^{-4}$. For the smallest mesh size $3d_0$, a residual displacement is observed independently of the strain, with higher values for compressional waves than for shear waves.

Overall, the propagation of compressional and shear waves confirms that a mesh size of at least $12d_0$ is necessary to avoid a mismatch of material properties between FEM and DEM. It also confirms the ability of our numerical framework to satisfactorily transmit waves of different kinds yet only for small strains, which is a standard assumption of concurrent coupling methods.
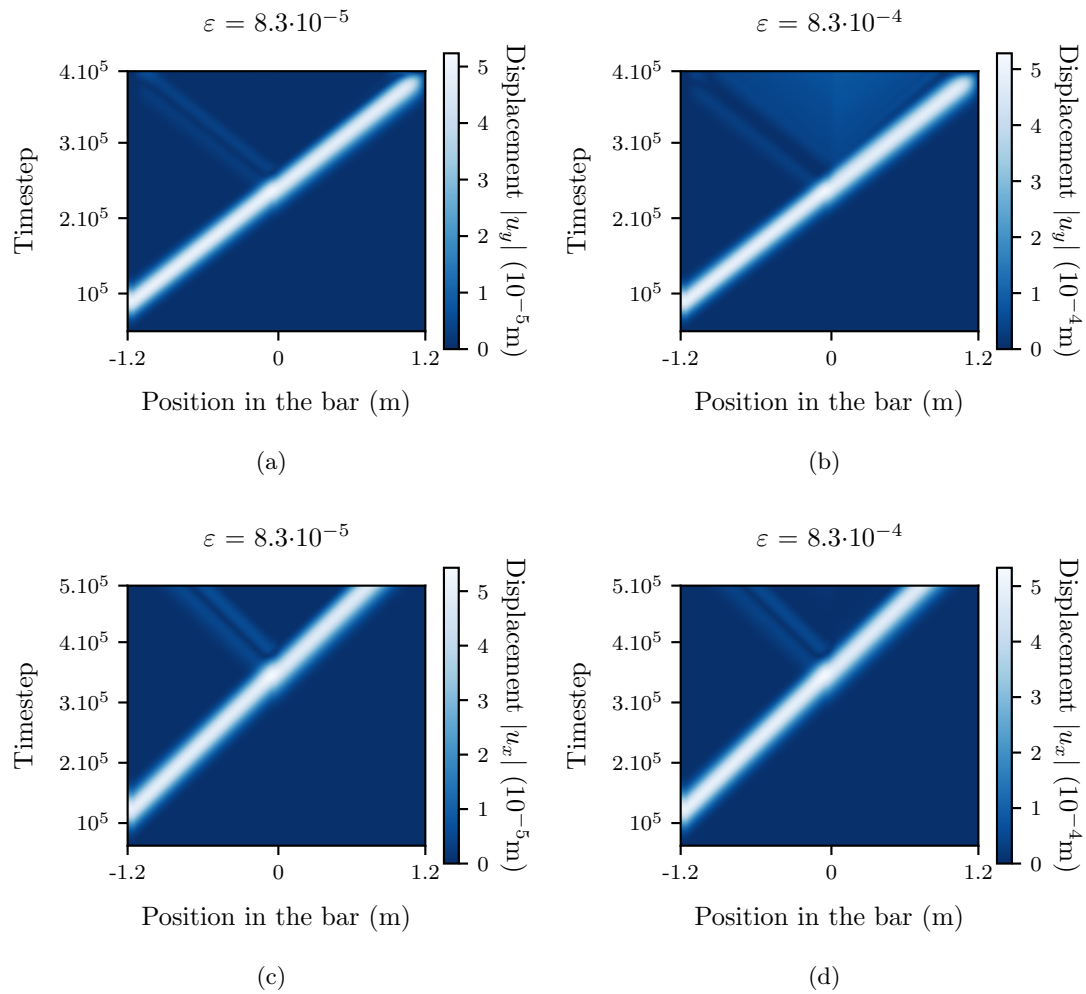
Figure 4.8: Wave transmission through the coupling interface for a mesh size of $12d_0$ and $\lambda = 200d_0$. (a, b) represent the ct diagrams of compressional waves at different strains. (c, d) represent the ct diagrams of shear waves at different strains.
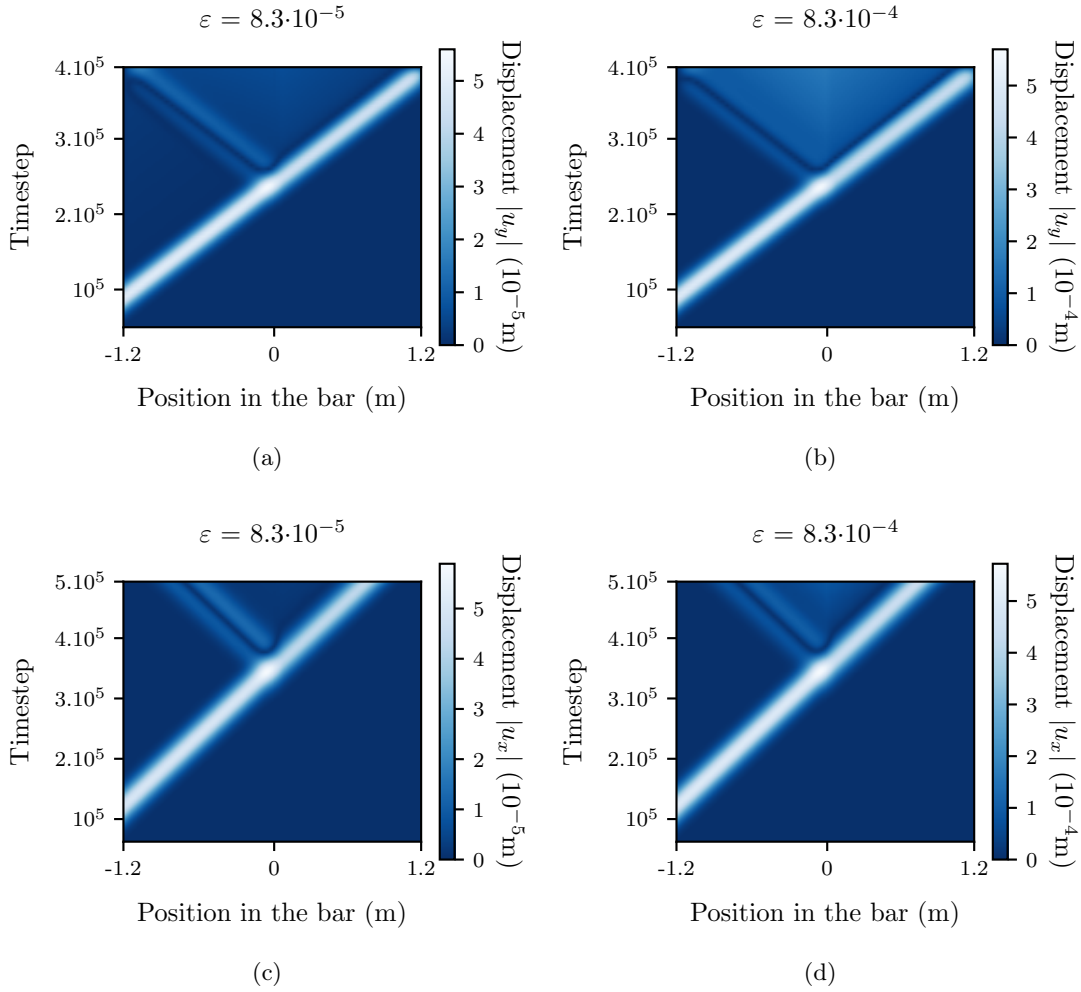
Figure 4.9: Wave transmission through the coupling interface for a mesh size of $3d_0$ and $\lambda = 200d_0$. (a, b) represent the ct diagrams of compressive waves at different strains. (c, d) represent the ct diagrams of shear waves at different strains.

4.5   Conclusions

We have investigated the transmission of elastic compression and shear waves through a DEM/FEM interface. Two different coupling strategies have been proposed with regard to the formulation of the kinematic constraints, termed "strong coupling" and "weak coupling". The effect of subtracting the initial force at the FEM interface has also been studied.

For verification purposes, we devised a simulation set-up in which both DEM and FEM are meant to represent the same material when deforming in small strain conditions. We first determined that our granular samples can be considered as homogeneous,

linear-elastic and isotropic for sample sizes larger than 12 times the representative grain size. This size constrains the minimum finite-element mesh size to be used in order to match elastic properties between the continuum and the discrete domains.

Next, we developed a test to determine the most stable approach (in the sense of introducing the least noise in the system). We observed that the "strong" version of the coupling (e.g., constraints defined exactly at each grain that overlaps with FEs) outperforms the "weak" one (which weights the constraints differently depending on the relative position of the grains with respect to the nodes of the element that engulfs it). Additionally, correcting the spurious forces induced by pre-stressed FEs was proved remarkably beneficial when it comes to stabilize the DEM/FEM overlapping region. We concluded that the strong coupling considering the subtraction of initial force is the proper choice for the problem at hand.

Finally, longitudinal and shear waves were sent through coupled DEM/FEM model. The results reveal the presence of a reflected wave, due to the dispersion happening at the FEM-DEM interface, whose amplitude decreases as the wavelength increases. Additionally, the propagation of waves confirms that a mesh size of at least 12_0 is necessary to avoid a mismatch of material properties between FEM and DEM. Overall, the results confirm the aptitude of our numerical framework in the LibMultiScale software to satisfactorily transmit small-strain waves of different kinds (compressional/shear) between the two domains.

As mentioned in Section 2.1.3, in the context of a third-body evolving over time, it is interesting to model wear formation and crack propagation in discrete regions by adding adhesion between particles. Therefore, in the next chapter, we will use the FEM-DEM coupling approach to model these types of material failure.

Chapter 5

Two-scale concurrent simulations for crack propagation using FEM-DEM bridging coupling

Disclaimer

This chapter is in part reproduced from the article: Manon Voisin-Leprince, Joaquin Garcia-Suarez, Guillaume Anciaux, Jean-François Molinari, "Two-scale concurrent simulations for crack propagation using FEM-DEM bridging coupling", *Submitted.* All authors have granted their permission.

Contents

5.1   Introduction

In Chapter 4, we introduced a FEM-DEM bridging coupling method to model large systems, where the same material is represented in both FEM and DEM. In this study, the FEM and DEM were connected using an overlapping method also known as the *bridging* method [97], which involves a "reconciliation zone" where the discrete and

continuum domains coexist and where their deformation is harmonized. Various forms of the overlapping method, including weak and strong formulations, were considered. The study employed Hertz contact between the particles and focused on the transmission of small-amplitude waves. Both formulations were demonstrated to be effective, with the strong formulation exhibiting superior stability. Additionally, the effect of incorporating a "force subtraction" method at the FEM-DEM interface to mitigate the influence of ghost forces was investigated [84].

In this chapter, the previously described coupling method is employed to computationally investigate two material failure events in a quasi 2D simulation box: the first case involves mode I crack propagation, while the second case involves wear leading to debris formation. We employ the discrete element method to capture both crack propagation and wear, and utilize the finite element method to save computational resources in modeling the regions that remain linear and elastic. Both DEM and FEM represent the third-body layer and therefore are modeled with matching material properties. To model the material portion that undergoes failure, we use the coarse-grained discrete element technique developed by Pham-Ba and Molinari [76] (see Section 2.1.2). The FEM-DEM coupling is realized using the FEM-DEM bridging coupling developed by Voisin-Leprince et al [91]. Section 5.2 presents the method used in this paper, including the coarse-grained discrete element model, the FEM-DEM bridging coupling, and the geometry of the simulations. Section 5.3 shows the result obtained for the two investigated cases. Section 5.4 provides closing remarks.

5.2   Method

Based on the results from chapter 4, we employ in the next chapter a strong formulation and a force subtraction method at the FEM-DEM interface.

5.2.1   Discrete domain

To model crack propagation and wear formation in the discrete domain, we employ the coarse-grained approach developed by Pham-Ba and Molinari [76] (see Section 2.1.2), which enables detachment and reattachment of particles thanks to appropriate adhesive forces. The parameters of the interaction forces between particles are determined such that the assembly of several particles exhibits certain mechanical properties. Therefore, employing this contact law enables controlling the macroscopic material properties exhibited by the DEM. Similarly to Pham-Ba and Molinari, we considered the macroscopic material properties of SiO_2 (see Table 5.1) for the DEM and FEM. The critical particle size required by the contact law to achieve an accurate match of macroscopic material properties is $d_c = 1.7$ nm (see Eq. 2.16 in Section 2.1.2). The minimum particle size determined by computational constraints is $d_{min} = 0.37$ nm (see Eq. 2.17 in Section 2.1.2). If a particle is smaller than this value, it will interact with more particles than its

closest neighbors, increasing the computational cost. Based on these values, we chose a log normal distribution of particle sizes with a mean grain diameter of $d_0 = 1.3$ nm, a maximum grain diameter of $d_{\max} = 1.2d_0$, a minimum grain diameter of $d_{\min} = 0.8d_0$, and a variance of $\sigma_{\mathrm{p}} = 0.2(d_{\max} - d_{\min})$nm.

Table 5.1: Amorphous silica properties (SiO$_2$) and particle size parameters.

SiO$_2$	
Young's modulus, E	73 GPa
Grain density, ρ	2200 kg/m^3
Poisson's ratio, μ	0.17
Tensile strength, σ_{n}	16 GPa
Shear strength, σ_{t}	9 GPa
Surface energy, γ	1.5 N/m
Restitution coefficient, η	0.9
Mean grain diameter, d_0	1.3 nm
Maximimum diameter, $d_{\max}$	$1.2d_0$ nm
Minimimum diameter, $d_{\min}$	$0.8d_0$ nm
Variance, σ_{p}	$0.2(d_{\max} - d_{\min})$ nm

Considering that a DEM particle is an order of magnitude larger than the bond lengths between atoms in silica (Si-O: 0.16nm, O-O: 0.26nm, Si-Si:0.31nm) [90], Pham-Ba and Molinari [76] already show a significant reduction in computational time by using their DEM contact law compared to MD. To further reduce computational costs and enable modeling of larger domains, a FEM-DEM bridging coupling approach is deemed necessary. The coupled simulations in this chapter were performed using LibMultiScale software [10–13], and visualized with ParaView software [6].

5.3 Results

The geometries of the simulated system are shown in Figure 5.1. The left side illustrates the geometry of the mode I crack propagation simulation, while the right side shows the geometry of the shearing system that leads to wear debris formation. Both cases share common geometry parameters. The systems are quasi-2D, with a thickness in the z direction of $3d_0$. The FEM elements have a characteristic size in the x and y directions of $h_{\mathrm{e}} = 20d_0$. The height of the bridging region (indicated in red in Figure 5.1) is chosen to be equal to the height of one FEM element, $h_{\mathrm{e}} = 20d_0$. The pad region, indicated in purple in Figure 5.1, serves as boundary conditions for the DEM particles by constraining all contained particles to the FEM displacement field. The height of the pad region is set to $h_{\mathrm{pad}} = 3d_0$. Periodic boundary conditions are applied in the x and z directions for both simulation setups.
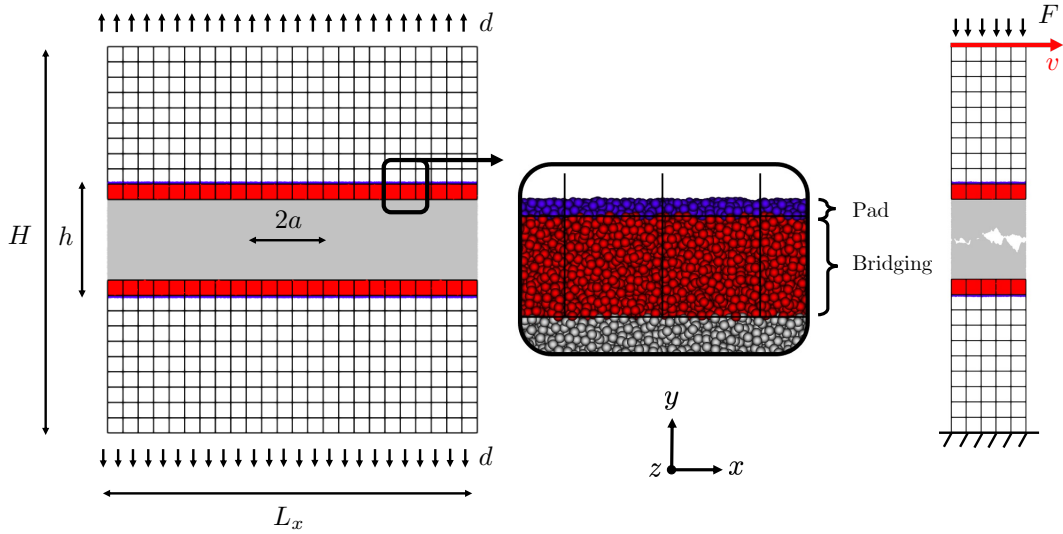
Figure 5.1: Left: scheme of the mode I crack propagation. Right: geometry of the shearing system. Middle: illustration of the overlapping zone of the coupling method, in red the bridging region where the coupling occurs, and in purple the pad region which serves as boundary for the DEM particles.

5.3.1 Mode I crack propagation

The mode I crack simulations were conducted on three coupled systems with a total height of $500d_0$, each having different DEM heights: small ($110d_0$), medium ($150d_0$), and large ($190d_0$). These DEM heights include the bridging and pad regions. Studying multiple DEM heights allows to assess whether the location of the coupling region/FEM region has any influence on the DEM behavior. To ensure a fair comparison of the coupling results, a pure DEM simulation of size $500d_0$ was also performed. For these simulations, a total length of $L_x = 400d_0$ is considered. An imposed vertical displacement induces an opening of width $2a$ where the bonds between opposed particles in the upper and lower lips are disabled.

To assess the consistency of the coupling results in mode I crack propagation, the kinetic energy per particle is evaluated. For each simulation, the kinetic energy is evaluated within the same region corresponding to the smallest DEM portion ($110d_0$), excluding the bridging and pad regions (refer to Figure 5.2).
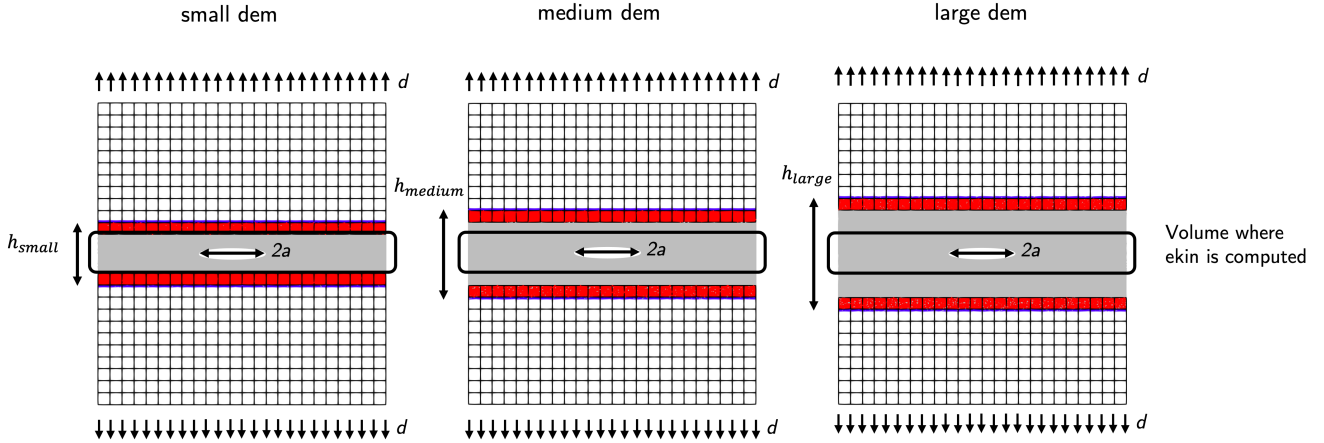
Figure 5.2: Schematic that illustrates the three DEM cases: small DEM ($h_{\text{small}} = 110d_0$), medium DEM ($h_{\text{medium}} = 150d_0$), and large DEM ($h_{\text{large}} = 190d_0$). The region where the kinetic energy is computed in each case is indicated by a black rectangle.

The mode I crack propagation simulation is characterized by two stages. The first stage corresponds to the opening of the crack lips in the DEM region. Then, there is a second stage corresponding to the propagation of the crack. The kinetic energy during these two phases is represented in Figure 5.3. It can be observed that the kinetic energy of the three coupled systems and the pure DEM simulation are in close agreement during both the opening phase and the crack propagation phase. Note that a perfect match cannot be obtained for an amorphous material due to a random organization of particles in parts of the simulation domain. This confirms that the crack initiation occurs at a similar time in each simulation. The similar results between the coupled systems and the pure DEM simulation validate the accuracy of the coupled systems in reproducing the crack propagation kinetics observed in the pure DEM simulation. Additionally, it shows that the location of the FEM region does not influence the DEM behavior.

Figure 5.3: Kinetic energy per particle for the three coupled systems with initial DEM heights: $110d_0$, $150d_0$, $190d_0$ and for the pure DEM simulation $500d_0$. Total height of each simulation is $500d_0$.

To showcase the precision of the FEM-DEM coupling in mode I crack propagation, we visualized the velocity field. Figure 5.4a shows the velocity field for the medium DEM size case. In Figure 5.4a, we observe a precise connection of the contour lines between the DEM and FEM, indicating a continuity of the velocity field from one domain to the other. In the supplementary material, several time steps are provided to display the evolution of the crack.

While studying crack propagation, stress concentration is a key aspect. In the FEM, the Cauchy stress tensor $\boldsymbol{\sigma}_{\mathrm{FEM}}$ is computed using the constitutive relation $\boldsymbol{\sigma}_{\mathrm{FEM}} = \boldsymbol{C} : \boldsymbol{\varepsilon}$, with $\boldsymbol{\varepsilon}$ the infinitesimal strain tensors and $\boldsymbol{C}$ the elastic modulus tensor. Whereas in the DEM, the stress $\boldsymbol{\sigma}_{\mathrm{DEM}}$ is computed using the virial stress (see LAMMPS documentation [29]). DEM stresses are averaged over a spherical volume, considering spherical radii of: $r = 3d_0$, $r = 6d_0$, $r = 8d_0$, and $r = 10d_0$. The largest radius considered leads to a diameter similar to the size of the FEM element. For a radius of $r = 3d_0$, the stress is not averaged over a sufficiently large region, resulting in noisy results (see Figure 5.5a). On the other hand, for a radius of $r = 8d_0$ and $r = 10d_0$, the stress is averaged over a region that is too extensive, leading to smoother results but blurring the stress concentration at the crack tips (see Figure 5.5b which depicts the stress for a radius of $r = 8d_0$; results for a radius of $r = 10d_0$ are not shown because they are very similar to $r = 8d_0$). Therefore, for representing the stress, we have chosen a radius of $r = 6d_0$, which provides a notable continuity of the isolines between the FEM and DEM domains (see Figure 5.4b). Thus, averaging the DEM stress over a properly chosen region leads to comparable results in FEM and DEM. Consequently, our approach can be used for a comprehensive study of crack propagation.
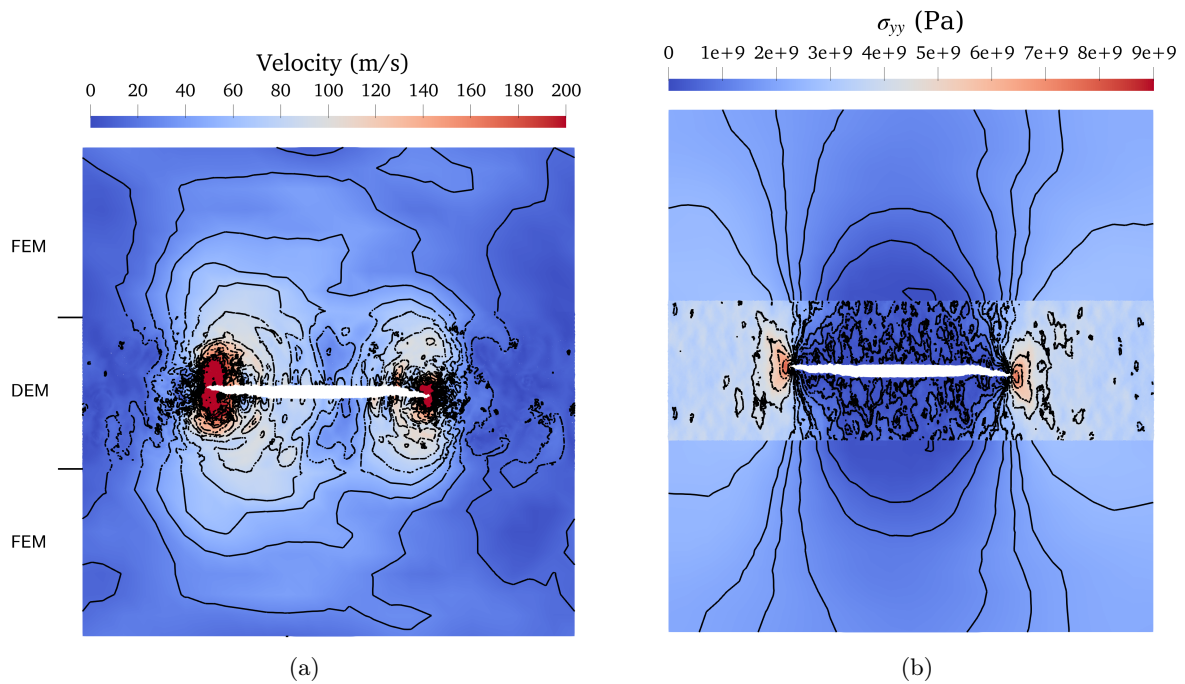
Figure 5.4: (a) Illustrates the velocity field, while (b) shows the stress field σ_{yy} for the coupled system composed of the medium DEM ($150d_0$). The stress field is averaged within the DEM over a spherical volume with a radius of $r = 6d_0$. Isolines for each field are represented in black. In (a), the top and bottom line elements have been omitted to enhance the visualization of crack propagation over the boundary limits. Furthermore, in (a), vertical black lines indicate the boundary between the top of the DEM and the FEM.
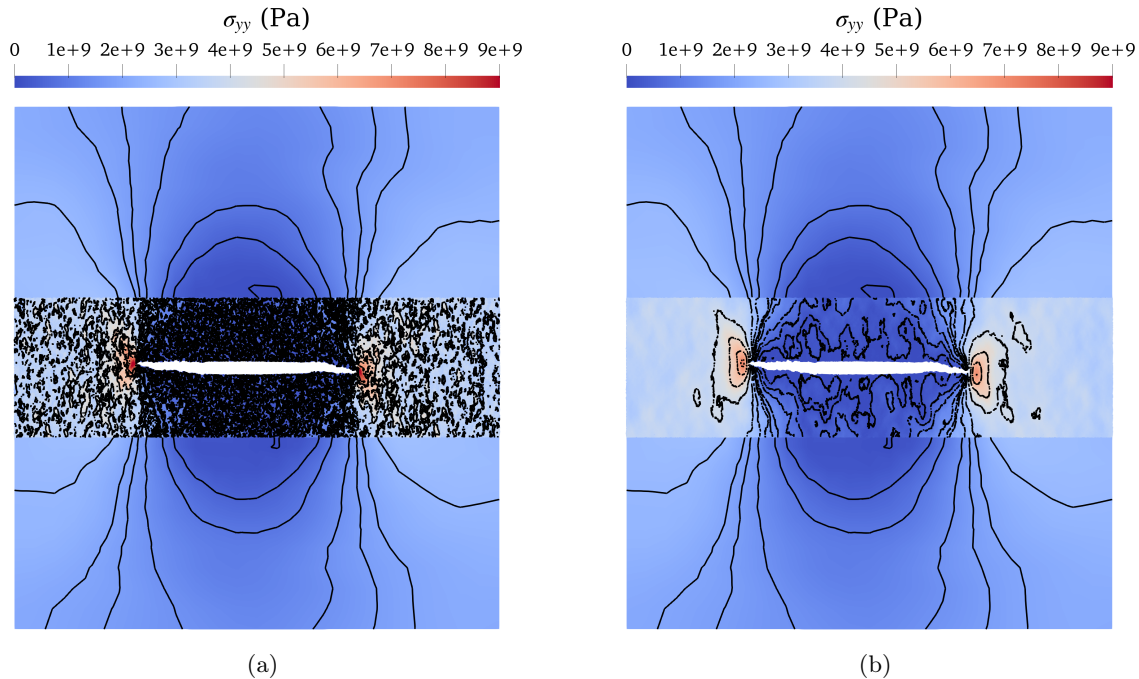
Figure 5.5: (a) and (b) represents the stress field σ_{yy} for the coupled system composed of the medium DEM ($150d_0$). In (a), the stress field is averaged over a spherical volume of radius $r = 3d_0$ within the DEM, while in (b), the stress field is averaged over a spherical volume of radius $r = 8d_0$. The isolines of the stress field are depicted in black.

Table 5.2 presents the time duration for each simulation time step Δt in the three coupled simulations (DEM height: $110d_0$, $150d_0$, $190d_0$) and the pure DEM simulation (DEM height: $500d_0$). The computation of the time per time step was performed using the serial version of LibMultiScale and LAMMPS. As expected, it can be observed that the time per time step is smaller in the coupled simulations compared to the pure DEM simulation. Additionally, the time per time step increases with the number of particles N. Therefore, the FEM-DEM coupling accurately represents the behavior expected from a pure DEM simulation, while significantly reducing computational time.

Table 5.2: Time per simulation time step for the mode I crack propagation simulations. N is the number of particles and, Δt the time step.

DEM height	N	Time per Δt
$110d_0$	229120	1.71s
$150d_0$	312360	2.14s
$190d_0$	395800	2.57s
$500d_0$	1243050	10.23s

5.3.2   Surface wear during relative sliding

For the shearing systems, a total length of $L_x = 100d_0$ is considered, and rough surfaces are introduced in the DEM. The roughness is characterized by two main parameters: the Hurst exponent $\mathcal{H}$ and the arithmetical mean deviation of heights S_a, with chosen values for this study being $\mathcal{H} = 0.8$ [63] and $S_a = 5d_0$. The choice of S_a is based on the critical junction size d^* which represents the size at which two surfaces in shear motion begin to detach and form wear particles [2]. Previous research by Pham-Ba and Molinari [76] has demonstrated that, based on their contact law and the material properties of SiO_2, d^* falls within the range of 10nm to 20nm. Thus, to facilitate wear formation using d^* as a reference, we select an arithmetical mean deviation of $S_a = 5d_0$, resulting in a DEM junction at the start of the simulation of size d^*. The DEM is carved to the desired roughness using Tamaas code [45]. In the simulation, the system is blocked at the bottom boundary. The top nodes of the FEM are subjected to a constant normal pressure of 100MPa and a constant shearing velocity of $v_s = 0.01\sqrt{E/\rho}$.

To study the formation of wear particles, we considered three coupled systems, each with a total height of $500d_0$, and different DEM heights: $110d_0$, $150d_0$, $190d_0$. These DEM heights account for both the bridging and pad regions. To make a proper comparison of the results obtained from the coupling, a pure DEM simulation of size $500d_0$ was also performed. Similarly to the mode I crack propagation, the kinetic energy for each case was computed within the same specific region characterized by the smallest DEM height, excluding the bridging and pad regions.
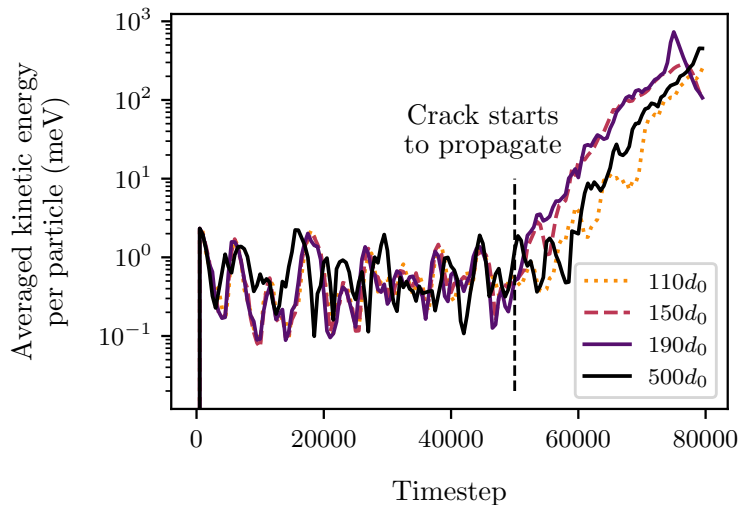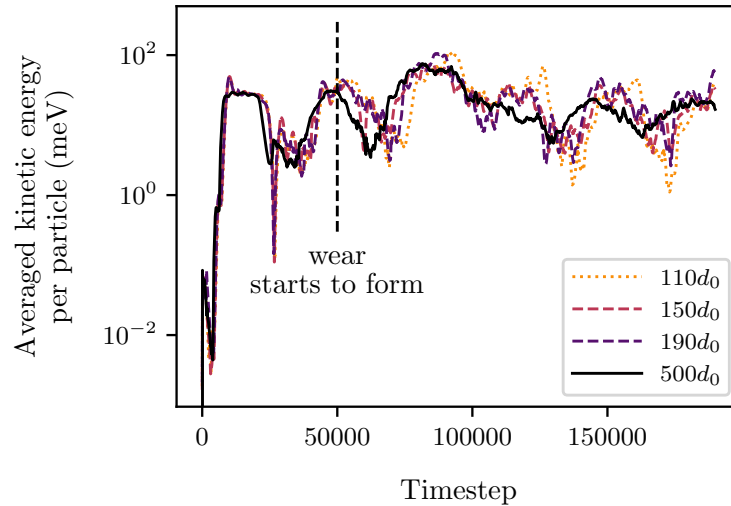

Figure 5.6: Kinetic energy per particle for the five coupled systems with initial DEM heights: $110d_0$, $150d_0$, $190d_0$, and for the pure DEM simulation $500d_0$. Total height of each simulation is $500d_0$.

The coupling simulations can be divided into three stages: uniform deformation be-

fore crack formation, debris formation, and subsequent rolling wear. Figure 5.6 shows the kinetic energy evolution of the coupled and pure DEM systems. It can be observed that the kinetic energy maintains a consistent level throughout the simulation. Additionally, both the coupled system's kinetic energy and that of the pure DEM simulation closely align. This confirms that the coupled system accurately captures the velocity field, regardless of the location of the coupling/FEM region.

To confirm that the coupling is accurately representing the expected physics of the pure DEM, we examined the evolution of the whole domain thickness over time. Figure 5.7 shows this evolution, with $\Delta h = h_t - h_0$ the change in the domain thickness through time, h_t being the total domain thickness at time t, and h_0 the total domain thickness at the initial time step. The evolution of the domain thickness, over time, can be interpreted as the size of the created wear debris. Figure 5.7 demonstrates that both the coupled systems and the pure DEM simulation initiate debris formation at a similar time (at around $50,000$ time steps), with the debris reaching a comparable size of approximately $15d_0$. Thus, the coupling approach effectively captures the wear debris physics of the pure DEM simulation. Furthermore, the location of the FEM region does not affect wear formation. In other words, launching the simulation with the smallest DEM coupled system is sufficient to represent the wear debris physics of the pure DEM simulation while reducing computational cost.
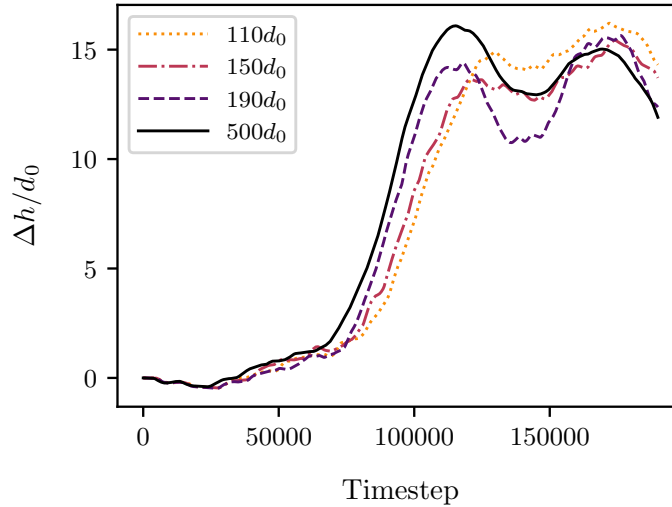
Figure 5.7: Evolution of the domain thickness Δh over time, normalized by the mean grain diameter d_0. The evolution of the domain thickness was computed for the five coupled systems with initial DEM heights: $110d_0$, $150d_0$, $190d_0$ and for the pure DEM simulation $500d_0$. Total height of each simulation is $500d_0$.

To illustrate the precision of the coupling in the case of third-body creation, we visualized the velocity field for an initial DEM height of $150d_0$ (Figure 5.8). The wear formation process introduces perturbations in the velocity field, which can be observed

in Figure 5.8. Importantly, we observe a precise connection of the velocity field and contour lines between the DEM and FEM, indicating that the velocity is accurately transmitted from one domain to the other. This confirms the high level of precision achieved by the coupling. In the supplementary material, two different time steps are presented to illustrate the evolution of debris formation. Furthermore, we analyzed the stress field to visualize the crack propagation during the wear formation process (see Figure ref 5.9). Similar to the mode I crack simulation, we calculated the average stress of particles within a sphere of radius $6d_0$.
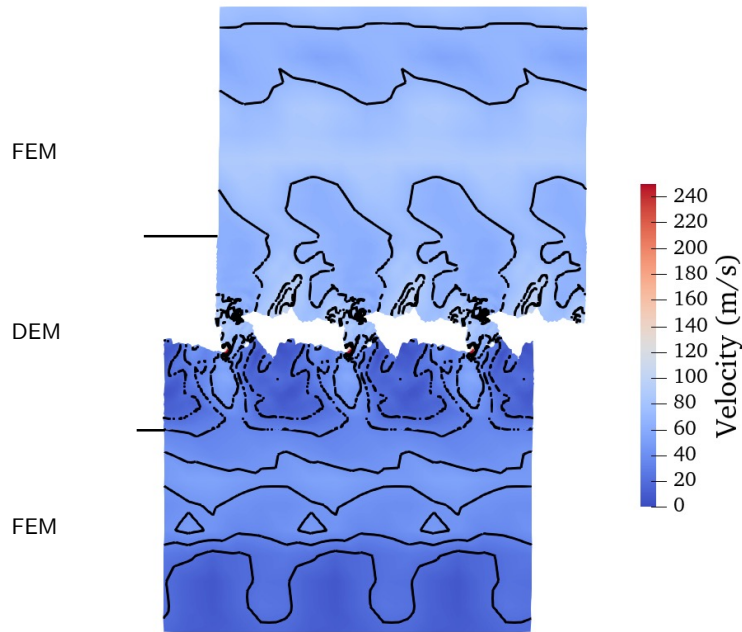
Figure 5.8: Representation of the velocity field for the coupled system with a DEM height of $150d_0$. The isolines of the velocity field are indicated in black. Vertical black lines denote the boundary between the top of the DEM and the FEM. The bottom-line element is omitted to prioritize the visualization of wear debris formation over the boundary limit.
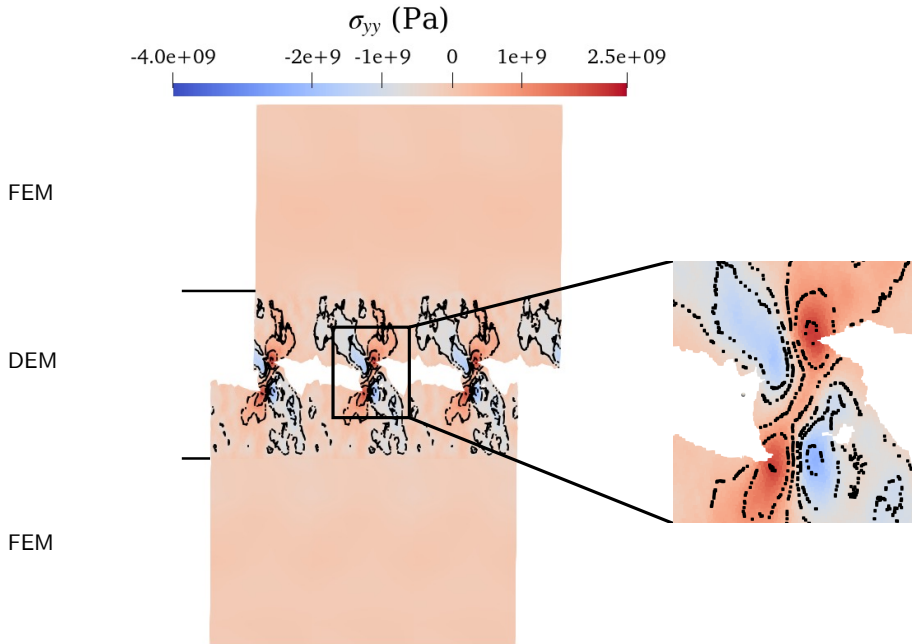
Figure 5.9: Representation of the stress field σ_{yy} for the coupled system with a DEM height of $150d_0$. The isolines of the stress field are indicated in black. Vertical black lines denote the boundary between the top of the DEM and the FEM. On the right, a zoomed-in view of the wear debris is presented.

Table 5.3 presents the time duration for each simulation time step Δt in the five coupled simulations (DEM height: $110d_0$, $150d_0$, $190d_0$) and the pure DEM simulation (DEM height: $500d_0$). Similar to the mode I simulations, the time per time step was computed using the serial version of LibMultiScale and LAMMPS. Consistent with the mode I results, the time per time step is smaller in the coupled simulations compared to the pure DEM simulation, and it increases with the number of particles N.

Table 5.3: Time per simulation time step for the wear formation simulations. N is the number of particles and, Δt is the time step.

DEM height	N	Time per Δt
$110d_0$	42039	0.17s
$150d_0$	58687	0.22s
$190d_0$	75375	0.28s
$500d_0$	206481	0.55s

5.4   Conclusion

In this exploratory study, we have demonstrated the effectiveness of the FEM-DEM bridging coupling [91] (Chapter 4) in simulating discontinuous events involving material failure. We investigated two scenarios: mode I crack propagation and wear debris creation during the contact between sliding rough surfaces.

For mode I crack propagation, we observed that crack initiation occurred simultaneously in both the coupled system and the pure DEM system. Furthermore, by exploring multiple DEM heights in the coupled simulations, we confirmed that the location of the coupling/FEM region does not influence crack propagation.

In the case of wear simulations, we observed that wear initiation and the resulting debris size were similar for both the coupled systems and the pure DEM system. Similarly to mode I crack propagation, studying various DEM heights in the coupled simulations shows that the location of the coupling/FEM region has no impact on wear formation.

In summary, we have effectively demonstrated that the coupling approach accurately captures the crack propagation and wear formation physics of the pure DEM. It is worth noting that the coupling region was intentionally positioned at a sufficient distance from the DEM region undergoing large deformation to prevent undesired crack propagation into the bridging region. Given that it is challenging for the FEM to precisely model the inelastic deformation of the DEM, such an arrangement would lead to a physically inaccurate representation. Hence, to facilitate the evolution of the discrete region without being constrained by the FEM, an adaptive coupling approach should be implemented.

5.5   Supplementary materials
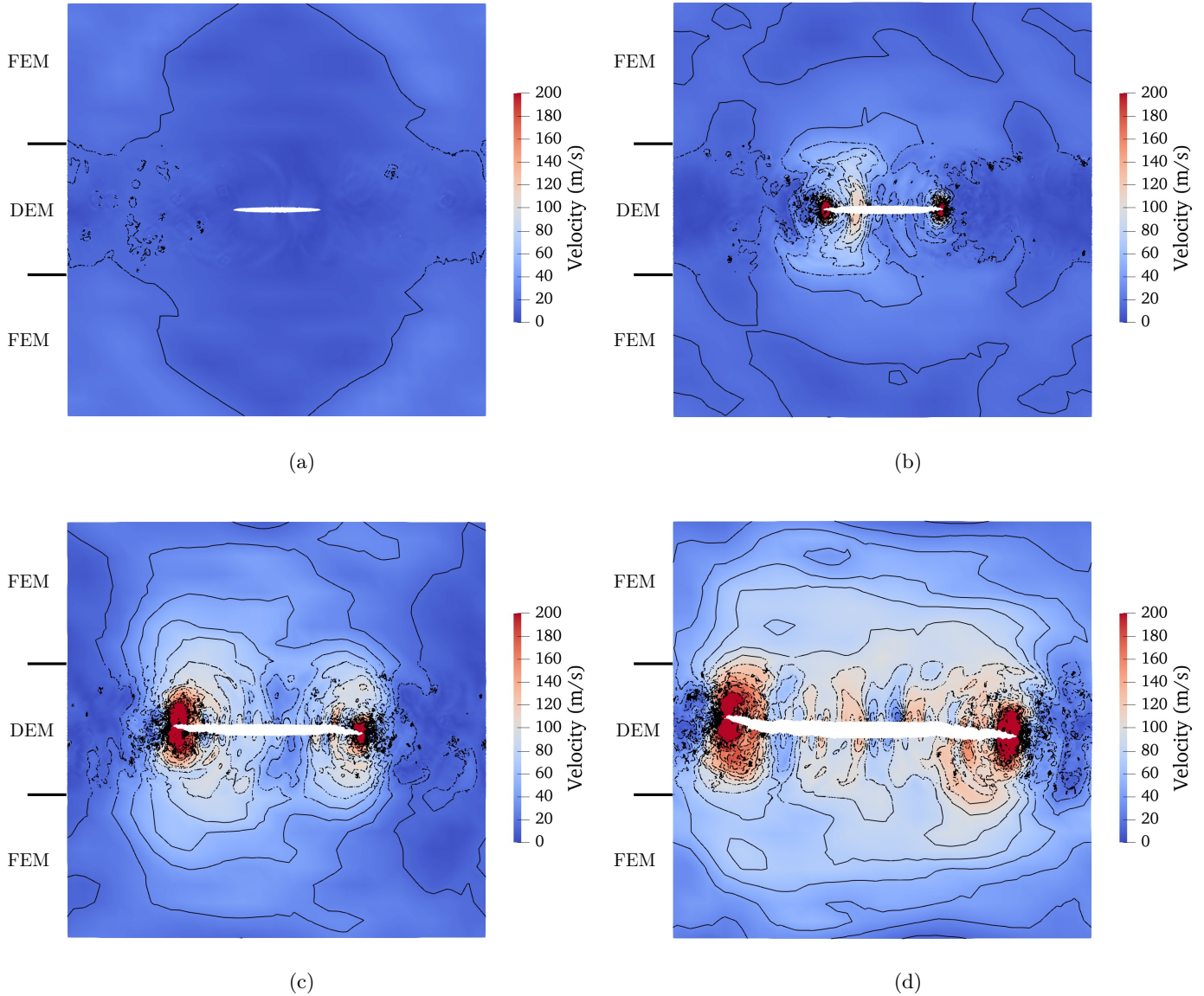
Figure 5.10: Representation of the velocity field for the mode I coupled system, composed of the medium DEM ($150d_0$). Isolines for the velocity field are shown in black. To enhance the visualization of crack propagation over the boundary limits, the top and bottom line elements have been omitted. (a) shows the system before crack propagation at time step 100, while (b), (c), and (d) represent the system at the respective time steps 120, 130, and 140, once the crack propagates.

(a)

(b)
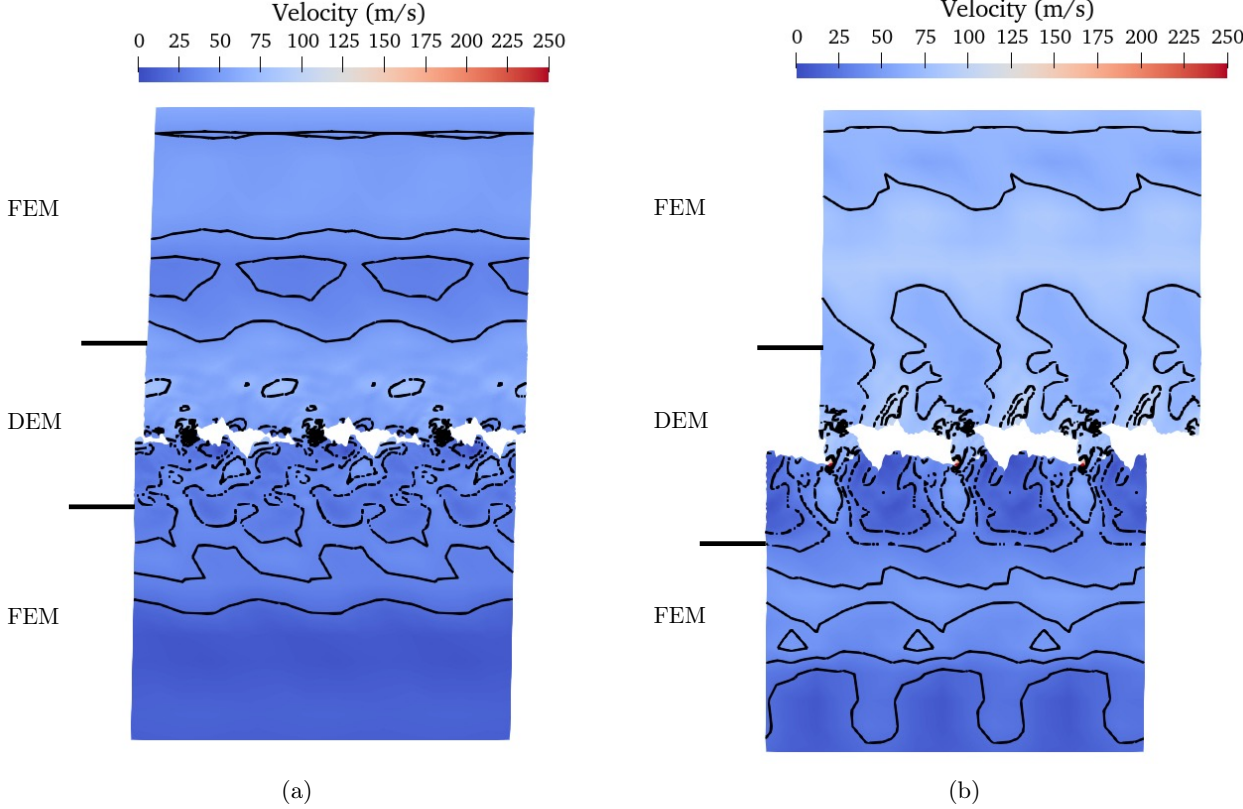
Figure 5.11: Representation of the velocity field for the sliding coupled system composed of the medium DEM ($150d_0$). Isolines for the velocity field are shown in black. To enhance the visualization of wear debris formation over the boundary limits, the bottom line elements have been omitted. (a) depicts the system prior to wear formation at time step 430, while figures (b) shows the system at time step 1000, after the formation of wear debris.

Chapter 6

Adaptive FEM-DEM bridging coupling

Contents

6.1 Introduction

In Chapter 3, it was shown that the evolution of the third-body is affected by both the boundary conditions and the system dimensions. Additionally, it was demonstrated that when using a truncated subsystem, neither force nor displacement controlled boundary conditions permits to recover the behavior of the original, i.e. larger, system. Thus, precisely capturing the third-body evolution requires an as large as possible system, in order to avoid artifacts created by the presence of boundaries. Given the numerous discrete particles present in a large system, a FEM-DEM coupling allows to substantially decrease the computational costs. In such a case, the third-body is modeled with

DEM particles, while the matching boundary conditions are provided by the connected continuum-FEM regions, thus delivering the appropriate compliance.

In Chapter 4, we introduced the bridging method, a FEM-DEM coupling approach allowing a material sample to be modeled with continuum and discrete domains simultaneously: the two domains coexist and are coupled within an overlapping region. In Chapter 5 the coupling has been used to model crack propagation and wear formation in material. However, in such models, the growth of the third-body is constrained by the size of the discrete region, necessitating the development of an adaptive coupling approach.

Adaptive coupling implies moving the coupling region. Determining when to extend the discrete domain needs a specific criterion. For instance, Chen et al. [25] employed an adaptive overlapping coupling between a continuum domain modeled with the Material Point Method (MPM) and a discrete domain modeled with the DEM. In this study, they started with a single continuum domain subject to shearing. To determine when the continuum domain must be replaced by the discrete domain, they identify the formation of shear band in the continuum domain through the detection of high strain rate gradient. Another example, at the nanoscale and considering crystalline materials, stands in the Quasicontinuum Method [64] which defines a criterion based on a measure of the deformation gradient, which determines when a continuum region should be replaced with a discretized molecular dynamics/statics model.

In what follows, the criteria will be computed within the discrete region, which will allow capturing when a complex deformation approaches the continuum. This shall prevent spurious forces to be generated by the continuum region (indeed, it cannot accommodate for non-smooth deformations). However, computing a deformation tensor from a discrete set of particles is not straightforward, as it necessitates to project discrete displacements to an equivalent continuum manifold. Extracting the deformation tensor field needs a projection-interpolation procedure which turns out to be computationally expensive, since it relies on Voronoi tessellation and/or Delaunay triangulation [41, 42, 72, 100]. The present chapter will establish simpler and less costly methods to establish when to adapt the coupling region.

A system made of two FEM blocks surrounding a central DEM/MD body, globally subjected to loading, is considered in all the cases presented in this chapter. The previously introduced coupling method couples the discrete and continuum domains (see Chapters 4 and 5). In the following, Section 6.2 introduces the adaptive coupling method - in particular the employed detecting strategy and criterion - while Section 6.3 presents several validation tests for both an amorphous structure and for a regular crystalline lattice. Finally, Section 6.4 examines how elliptical rigid bodies placed at the contact interface can influence the third-body thickness and friction evolution.

6.2 Method: Adaptive coupling

6.2.1 Evolution criterion

In Figure 6.1, the discrete domain is depicted with circular particles, while the continuum domain is made visible as a black grid mesh. In total, three regions are necessary to achieve adaptive coupling: the usual bridging and boundary regions are complemented with a detection region where the criterion for the discrete domain's evolution is evaluated. The bridging region is displayed in red, the boundary region in purple, and the detection region in blue. The coupling is realized considering a strong formulation (see Chapter 4).

Figure 6.1: Schematic of the adaptive coupling regions.The discrete domain is represented by circular particles, while the continuum domain is depicted with a black mesh. The boundary region of the discrete domain is marked in purple, the bridging region in red, and the detection region in blue.

An appropriate criterion triggering an extension of the discrete region should capture when inelastic deformations of the particles occur near the bridging region. This is to ensure that strong deformations remain distant from the bridging region, which is important as a proper coupling is guaranteed only under assumptions of regularity of the strain/displacement fields and of linear elastic behavior.

Thus to quantify the inelastic deformation of the particles, we evaluate the average change of neighbors per particle. For each particle in the detection region, the list of nearest neighbors is identified within a given radius R. Neighbor changes are detected by comparing the current list of neighbors to a reference list. The reference list, first established at the start of the simulation, is updated after each adaptation. Then, for each particle i, the spatial average of the number of neighbor changes within a radius R_{mean} is calculated and denoted by $n_{i,\mathrm{mean}}$ (refer to Figure 6.2).

95
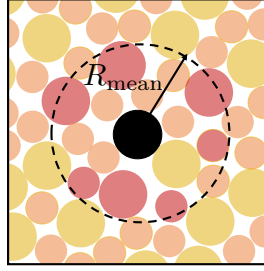
Figure 6.2: Schematic of the spatial average of the change of neighbors over a radius R_{mean}.

We denote N_{total}, the total number of particles within the detection region. The percentage of particles exhibiting a number of neighbor changes greater than or equal to a specified value, $n_{i,\mathrm{mean}} \geq \alpha$, is calculated. If this percentage exceeds the threshold, ε, the criterion for expanding the discrete domain is met:

$$\varepsilon \leq \left(\frac{\sum_{i=1}^{N_{\mathrm{total}}} H\left(n_{i,\mathrm{mean}} - \alpha\right)}{N_{\mathrm{total}}} \right) \times 100. \tag{6.1}$$

Here H is the Heaviside step function. The selection of ε depends on the scale of the detection region, as it is influenced by N_{total}. For future studies on larger systems, it could be advantageous to assess neighbor changes within subdomains smaller than the detection region currently used. These subdomains could, for instance, be on the scale of an FE element.

6.2.2 Expansion of the discrete domain

Once decided, the discrete domain needs to be expanded. The size of the expansion is equal to the size of the current bridging region, which for the setup used in this thesis turns out to also be the characteristic height of an element. To expand the discrete region, several steps must be followed, as illustrated in Figure 6.3.

The first step consists in shifting the boundary, bridging, and detection regions by a distance equal to the original height of a FE element. Consequently, the second step introduces new particles in the empty region (Step 2 in Figure 6.3). These new particles are taken from a periodic (in the x, y, and z directions) DEM/MD sample, having the same size distribution and material properties as those in the original and pristine discrete domain. They are placed in a geometry matching the undeformed bridging region.

In a third step, the coupling is re-initialized with these updated geometries (Step 3 in Figure 6.3). Then, the FEM displacement field is projected onto the new particles, in order to account for the continuum deformations (Step 2 in Figure 6.3). Next, the displacement of FE elements in the area transitioning from the bridging region to a

purely discrete region is adjusted. The FEM nodes have to be constrained to the discrete domain's displacements, which is done by solving a least-square problem as described by Equation 2.24. Additionally, the elements are visually disabled (Step 3 in Figure 6.3).

Finally, a relaxation process is carried out using velocity damping to stabilize the particles that are now in the bridging, and detection regions. Throughout this relaxation, all the other particles are fixed, i.e. those not in the new detection and bridging regions. To capture the system's dynamics, the velocity field of the FEM is then projected onto the bridging and detection regions. The adaptive coupling approach has been implemented in the open-source LibMultiScale software [10], and visualized with ParaView software [6].
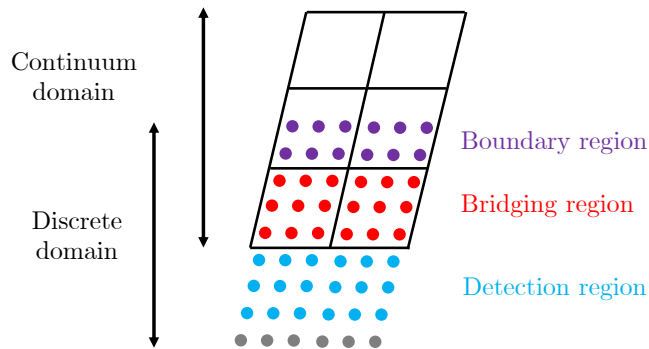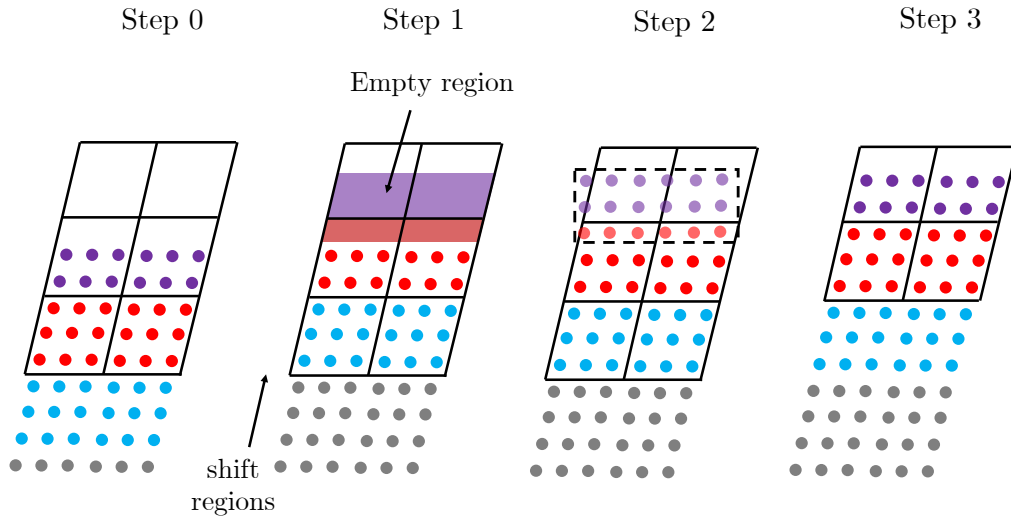

Figure 6.3: Schematic of the adaptive coupling process. The discrete region is depicted with circular particles, while the continuum domain is shown as a black mesh. The bridging region, where the coupling occurs, is shown in red; the boundary region, where the particles are slaved to the continuum domain, is in purple; and finally, the detection region is depicted in blue. Step 0 illustrates the system prior to adaptation. Step 1 shows the shifting of geometries, Step 2 the addition of new particles, and Step 3 the system's final configuration.

6.3 Validation

6.3.1 Adaptive FEM-DEM coupling

6.3.1.1 Geometry

To model the discrete domain, the coarse-grained contact law developed by Pham-Ba and Molinari [76] and summarized in section 2.1.2 is employed. For reminder, this law replicates key wear mechanisms observed in molecular dynamics, while reducing computational costs by considering larger, and therefore fewer particles. It also enables to choose the material macroscopic properties delivered by the DEM assembly. Hence, we consider the material properties of SiO_2, similarly to Pham-Ba and Molinari [76] and as described in Chapter 5. The particle size distribution is Gaussian. All material constants are detailed in Table 5.1.

We consider a system characterized by a length $L_x = 100d_0$, a total height $L_y = 200d_0$, and a thickness $L_z = 3d_0$. Periodic boundary conditions are considered in the x and z directions. The FEM element characteristic sizes are selected to be $10d_0$ in the x and y directions. The thickness in the z direction is spanned by two elements. As mentioned previously, the bridging height is chosen as one FEM element's height, corresponding to $10d_0$, the boundary region height is set to $3d_0$, and the detection region height is chosen to be $7d_0$. A constant normal pressure of 100MPa is applied to the top FEM boundary surface. This upper FEM surface is also constrained to a constant shearing velocity of $v = 0.1c$, where c is the push-wave celerity. The bottom FEM surface boundary is fixed. An initial junction of size of $30d_0$ is constructed in the central DEM region to facilitate the creation of a debris. Figure 6.4 depicts the geometry of the system being considered. The change of neighbors is computed considering the six closest atoms within a radius $R = 2d_0$, and averaged over a radius $R_{mean} = 5d_0$. If more than 2% of the particles have an average change of neighbors greater than or equal to $\alpha = 3$, then the criterion is satisfied.
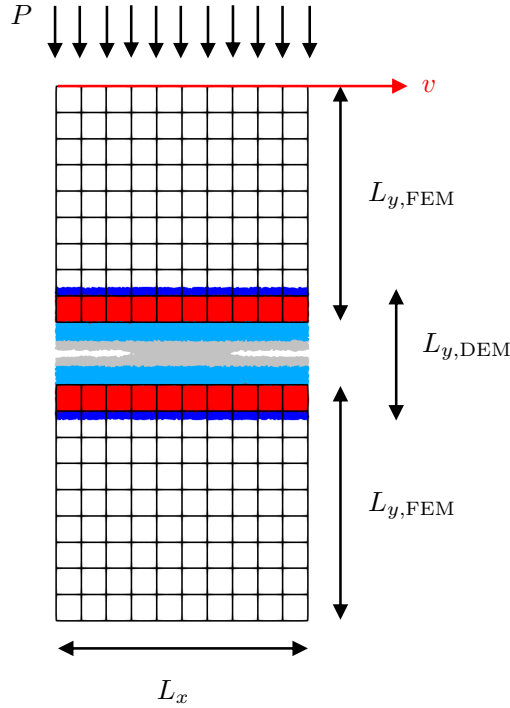
Figure 6.4: Schematic of the FEM-DEM validation setup. The bridging region is depicted in red, the detection region in light blue, and the boundary DEM region in dark blue.

Three cases will be considered in order to make in-depth comparison and to validate the usefulness of coupling adaptation. The first case is a non-adaptive coupled system with a DEM height of $50d_0$ (small DEM). The second case has the same initial DEM height but employs an adaptive coupling, and the last case has an initially larger DEM region, with height $70d_0$, and with an adaptive coupling which is nevertheless used.

6.3.1.2   Results

In Figure 6.5, the averaged change of neighbors for each particle is represented within the detection regions considering an initial junction size of $20d_0$. A significant change of neighbors is observed at the crack tip, where the cracks propagate to form the debris. This confirms that the average change of neighbors accurately characterizes DEM inelastic deformation, making it a reliable measure to determine the discrete domain expansion.

(a)
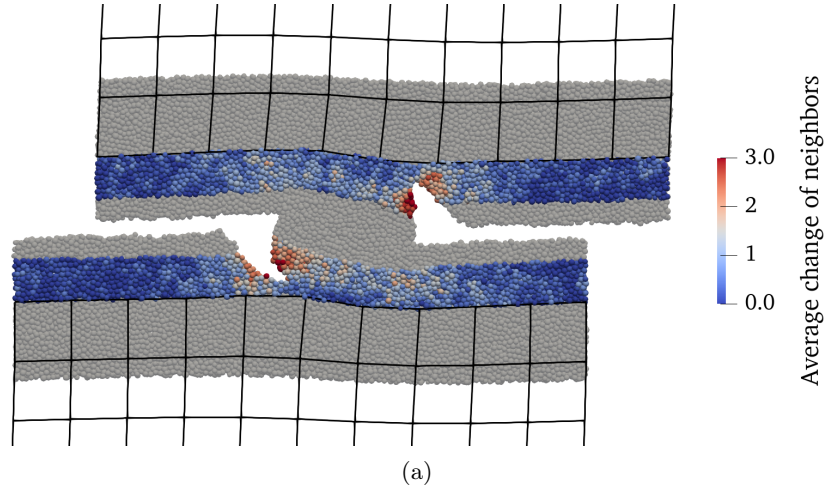
Figure 6.5: Average change of neighbors per particle. The DEM domain is depicted using circular/spherical particles, and the continuum is illustrated with a black mesh. Changes in neighbors are only observed within the detection regions.

In Figure 6.6, the displacement of the DEM in the three previously described cases is depicted from left to right. The top illustrations represent the cases before any adaptivity of the coupled regions, while at the bottom are shown the later situations, which is when adaptivity was triggered if adaptive coupling was employed. At the beginning of the simulation (top of Figure 6.6), we observe similar initiations of cracks and debris, as expected. However, later adaptivity changes that observation (bottom of Figure 6.6). In the first case with non-adaptive DEM, cracks propagate until the bridging regions, causing significant FEM deformations. The generated elastic forces are opposing the crack's propagation, which is inaccurate and should be avoided. In the case of the initially small DEM, but with adaptive coupling, the crack follows a path similar to the larger DEM case (which did not trigger any adaptation), showing the usefulness of adaptivity.

Figure 6.7 monitors the thickness of the third-body over time, somehow reflecting the evolution of debris' size. More precisely, the third-body thickness is here defined as the height measure of the area where a perceivable porosity forms as a result of wear and fracture. Therefore, the density of particles is computed in the DEM region, and areas where it falls below 5% are considered as part of the third-body. The thickness of the third-body is obtained by taking the highest and lowest points showing a density drop. All the adaptive cases, small and large, show similar third-body and debris sizes. On the contrary, the small non-adaptive coupling results in a different pattern: the thickness first begins to grow but later decreases (closing). This difference is believed to be due to the crack propagating in the bridging as previously mentioned. Thus, avoiding crack propagation in the bridging region is crucial, which highlights the need for an adaptive coupling.
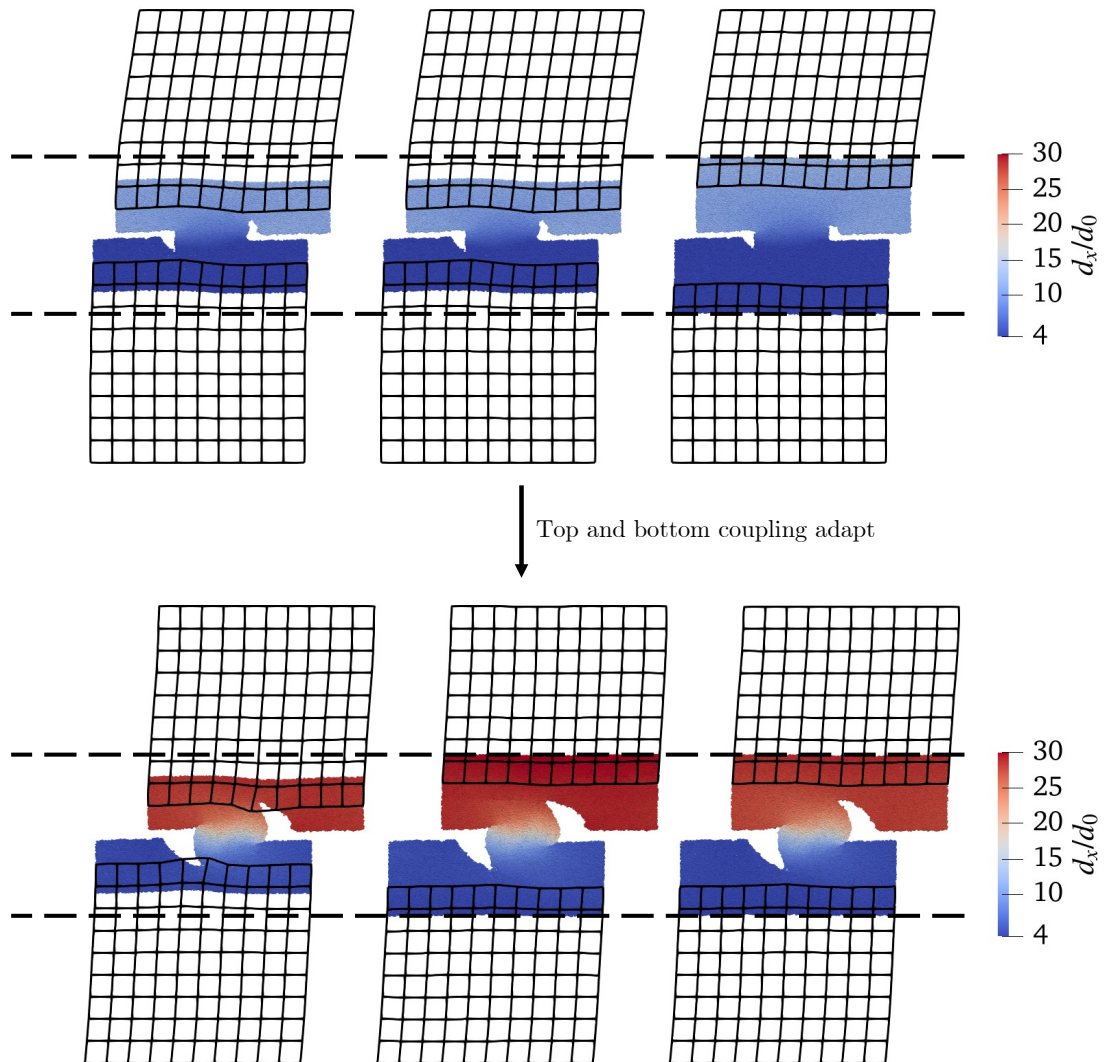
(a)

Figure 6.6: On the left, a non-adaptive coupled system is shown with a DEM height of $50d_0$. In the middle, an adaptive coupling system with the same DEM height of $50d_0$ is depicted. On the right, a larger adaptive coupling system with a DEM height of $70d_0$ is presented. Among these, only the middle system experiences a top and bottom coupling adaptation. On the top, the systems are illustrated before any expansion of the discrete region for the middle system, while the bottom shows the systems after the discrete region has been expanded. The horizontal dashed black line marks the largest discrete domain upper and lower limits, showing how the top and bottom coupling regions adapted.
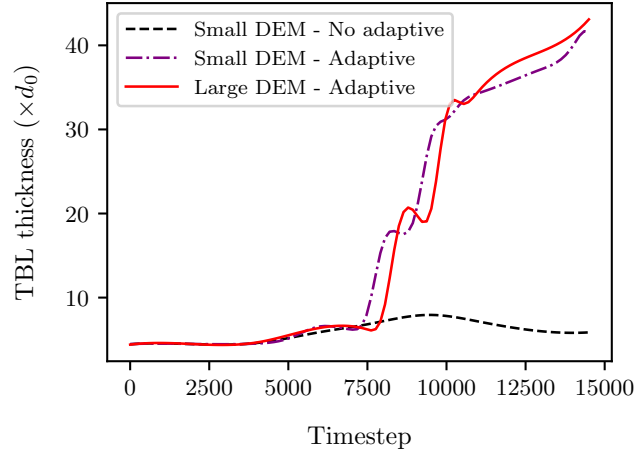
(a)

Figure 6.7: Third-body thickness evolution for an initial junction size of $30d_0$. Three scenarios are analyzed: a small DEM ($50d_0$) with a non-adaptive coupling, an initially small DEM ($50d_0$) with an adaptive coupling, and a large DEM ($70d_0$) with an adaptive coupling.

Although the adaptive coupling cases exhibit similar behavior, they are not perfectly identical. This is expected to result from the amorphous arrangement of DEM particles.

6.3.2 Adaptive FEM-MD coupling

6.3.2.1 Geometry

The adaptive coupling is now further studied with a three-dimensional MD-FEM setup. A face-centered cubic aluminum crystal is assembled with primitive lattice vectors given by $a_x = \sqrt{2}a$, $a_y = \sqrt{3}a$, $a_z = \sqrt{6}a$, where $a = 4.045$ $\mathring{A}$ is the lattice length characteristic of ground state aluminum. Each atom within the crystal has a mass of 26.981 g/mol. The used inter-atomic potential is the classical generalized EAM potential from Finnis and Sinclair [44]. The MD region is characterized by a length of $L_x = 20a_x$, a height of $L_{y,\text{MD}} = 100a_y$, and a thickness of $L_z = 2a_z$. The top and bottom FEM regions have a height of $L_{y,\text{FEM}} = 150a_y$, with 8 elements in x direction, 9 elements in the y direction, and 2 elements in the z direction. The height of the bridging and boundary MD regions are chosen to be equal to the height of an element: $2a_y$, and the height of the detection region is set to $4a_y$. A void is created at the center of the MD region by removing a square region of atoms. Similarly to previous (amorphous) simulations, compressive forces are then applied to the FEM top surface, while the bottom surface is maintained fixed. Figure 6.8 shows a schematic of the simulated system. Two simulations are compared, one with adaptive coupling and the other without.

The change of neighbors is now computed slightly differently in the MD case. The

change of neighbors is evaluated considering the twelve closest atoms within a radius $R = a\sqrt{2}$, without averaging this value. The criterion is met, if more than 1% of the particles have an average change of neighbors of at least $\alpha = 3$.
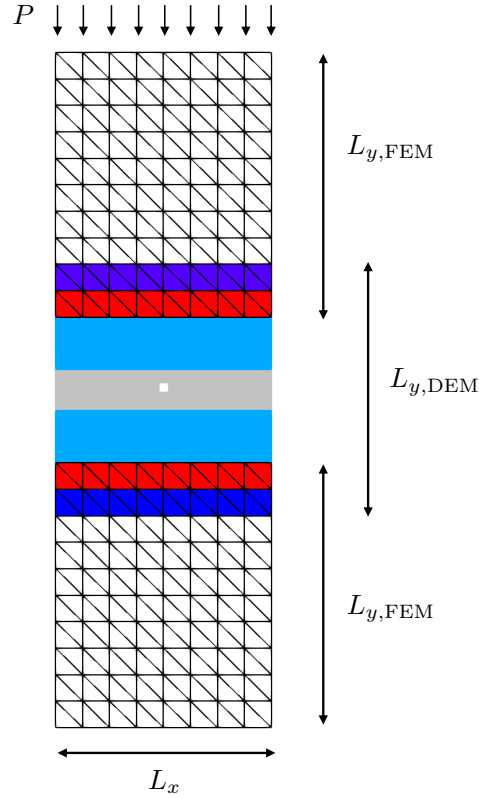
Figure 6.8: Schematic of the MD-FEM validation setup.

6.3.2.2   Results

A dislocation can be detected by examining potential energy. In the top of Figure 6.9, the per-atom potential energy is depicted for the non-adaptive case, while on the bottom the equivalent measure is shown for adaptive coupling. Three timesteps are displayed, time progressing from left to right, to show the evolution of dislocation positions and the interaction with the bridging region. In the non-adaptive coupling case, the dislocation joins the bridging region and then gets stuck within it. On the other end, having an adaptive coupling method allows the atomic region to expand, which let the dislocation propagate further without ever reaching the bridging region. Figure 6.10 summarizes this observation, by representing the vertical position of dislocations (where the potential energy is the largest) over time.
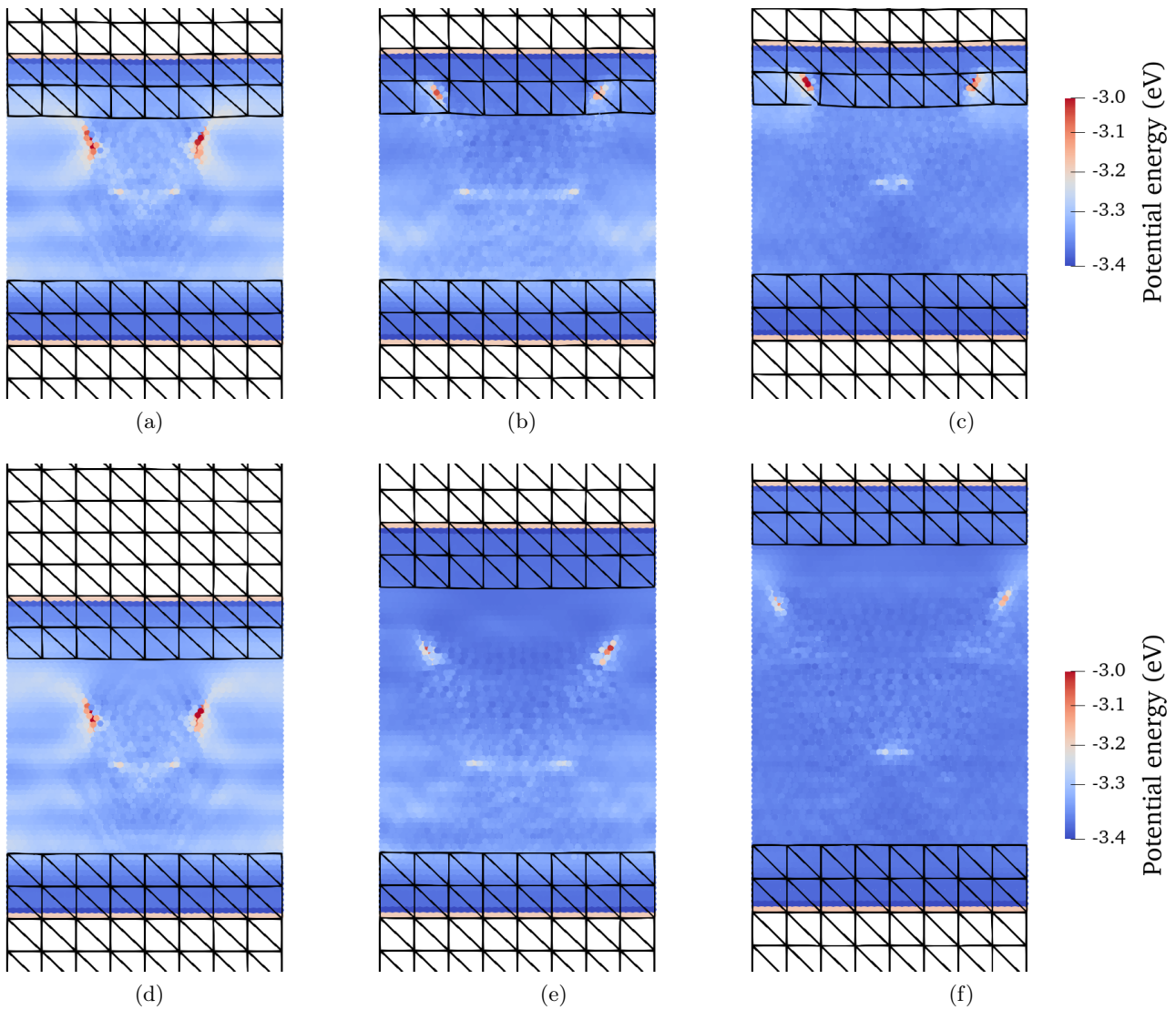
Figure 6.9: Potential energy in the MD, highlighting dislocation propagation. At the top, the non-adaptive coupling is represented, while at the bottom, the adaptive coupling is represented. In both cases, three timesteps are displayed: on the left, the 50th timestep; in the middle, the 60th timestep; and on the right, the 70th timestep.
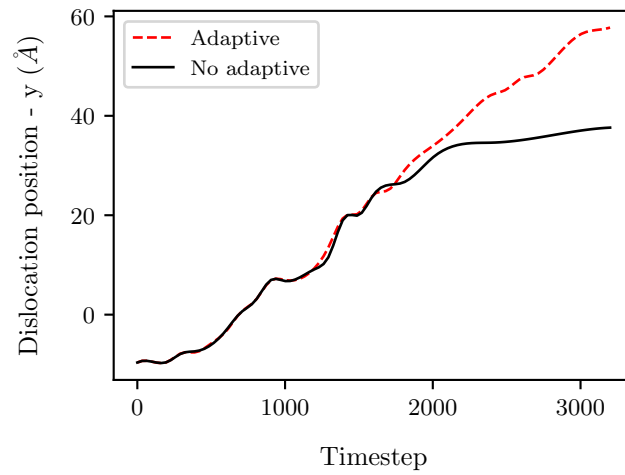
Figure 6.10: Dislocation position in the y direction for adaptive and non-adaptive coupling.

This improvement is made possible because of the capability of the detection criterion, based on the average change of neighbors, to accurately capture the trace of the dislocations within the detection region. To illustrate this, the measure of neighbor change is displayed for a non-adaptive coupling in Figure 6.11. Clearly, the dislocation traces can be extracted with atomic precision, allowing to let the detection band trigger adaptation at the right instant.

(a)
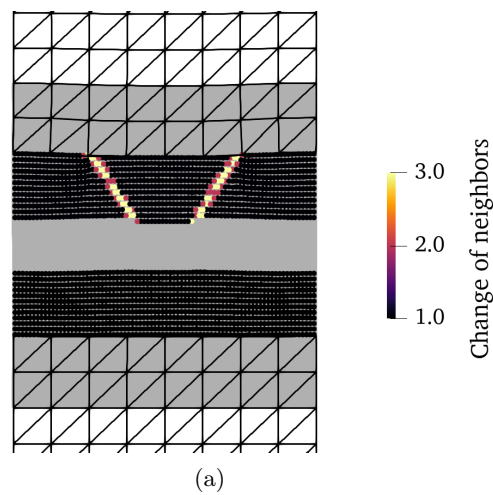
Figure 6.11: Change of neighbors in an MD-FEM non-adaptive coupling. The MD domain is in full gray, the continuum is shown with a black mesh, and the detection regions are marked by points.

6.4 Application: Third-body abrasive wear with lubricating elliptic rigid bodies

6.4.1 Model

Experimentally, it has been demonstrated that solid particles can influence abrasive wear [95]. In this section, we aim to explore the effects of introducing solid elliptical particles serving as lubricant between two sliding bodies. A system with a length of $L_x = 200d_0$, a thickness of $L_z = 3d_0$, and a height of $L_y = 200d_0$, employing periodic conditions in the x and z directions, is considered. FEM elements sizes are $10d_0$ in both x and y directions, with two elements along the z axis. The heights for the bridging and boundary regions are chosen to be equal to the height of a FE element. The initial DEM height is $70d_0$ including bridging and boundary regions. The top of the system is subject to a normal pressure of 500MPa and a constant shearing velocity $v = 0.03c$, while the bottom of the system is fixed. The setup of the system is depicted in Figure 6.12.

The discrete domain is modeled using the coarse-grained DEM law of Pham-Ba and Molinari [76] (refer to Section 2.1.2). Material properties are selected in line with Chapter 3, Section 3.2, featuring a Young's modulus E, a density ρ, and a restitution coefficient η typical for SiO_2. The Poisson's ratio ν is fixed at 0.25, which restricts the interaction forces to the normal direction (see Eq 2.9). The critical length scale d^*, i.e. the junction size where debris begins to form, is $10d_0$. The tensile strength σ_n will be varied in this section in order to create different gouge regimes, similarly to [75] and Chapter 3. Strengths of $0.14E$, $0.16E$, and $0.18E$ are considered, with such changes also affecting surface energies as $\gamma = \frac{d^* \sigma_n^2}{32E}$. Finally, the particle sizes follow a Gaussian distribution with the parameters given in Table 3.1

In our model, elliptic bodies are assigned a Young's modulus of $E_2 = 5E$, making them significantly more rigid than the surrounding regions. Therefore, in the remainder of this text we will refer to them as rigid bodies. Adhesion between elliptical rigid bodies and the surrounding particles is null, leading to the treatment of these rigid bodies as friction-less. The ellipsoids are equally spaced, with a major axis of $10d_0$ and a minor axis of $5d_0$. The influence of the number of ellipses n will be studied. In Figure 6.12, top DEM particles are displayed in gray (particle type: 1), bottom DEM particles are shown in blue (particle type: 2), and elliptic rigid bodies are depicted in red (particle type: 3). An initial spacing of $d_0/2$ is introduced between the top and bottom DEM particles. No gravity is considered.
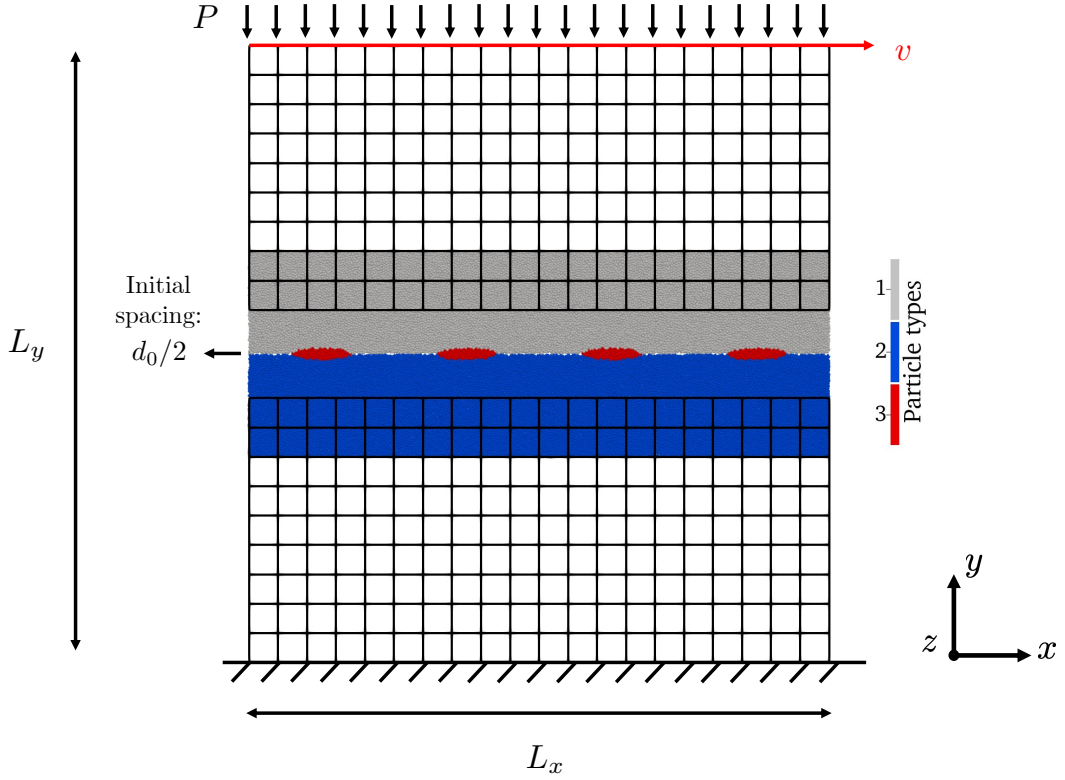
Figure 6.12: Schematic of elliptic rigid bodies in the adaptive FEM-DEM coupling. The top particles are shown in gray (particle type: 1), bottom particles in blue (particle type: 2), and elliptical rigid bodies in red (particle type: 3).

6.4.2 Results

To assess the influence of elliptic particles on the third-body, we analyze the shear stress σ_{xy} which is measured at the top of the FEM. The third-body thickness evolution will also be measured as it was done previously.

Figure 6.13b shows the shear stress σ_{xy} for different tensile strengths and numbers of rigid bodies. It can be observed that for four rigid bodies, a higher tensile strength, implying greater adhesion according to $\gamma = \frac{d^* \sigma_n^2}{32E}$, leads to more friction, which was expected. This same idea applies when considering two rigid bodies. Figure 6.13b also demonstrates that, more rigid bodies always results in reduced friction, which shows the expected lubrication effect provided by adding friction-less rigid body particles.

In Figure 6.13a, the third-body thickness evolution is shown. For all tensile strengths, the number of rigid bodies influence the gouge thickness. When considering four rigid bodies, the gouge thickness is smaller than for two rigid bodies, due to the lubricant effect. For tensile strengths of $0.14E$ and $0.16E$, with two rigid bodies, the gouge thickness shows a moderate increase, indicating a mixed regime where particles agglomerate

without forming complete wear debris, as observed in Figures 6.14a and 6.14c. However, when four rigid bodies are considered, the gouge thickness remains relatively small, corresponding to a more lubricated regime, as seen in Figures 6.14b and 6.14d.

In the case with the highest tensile strength ($0.18E$) and two ellipses, there is a noticeable increase in third-body thickness. At the same tensile strength with four rigid bodies, the third body exhibits a smaller thickness due to the formation of a lubricant regime, as depicted in Figure 6.14f. In reality, when only two rigid bodies are placed with the largest adhesion, the conditions are met to initial a crack propagation which would lead to a debris formation. This is then perceived as the important growth of the gouge thickness visible in Figure 6.14e.

Thus, the number of rigid bodies and the material's tensile strength both influence the thickness of the third-body as well as the friction resistance. In Figure 6.15, the velocity field for the higher tensile strength $0.18E$ with four rigid bodies is shown in the final configuration which allows highlighting the continuity of inertial exchanges through the discrete-continuum coupling interfaces.

(a)

(b)
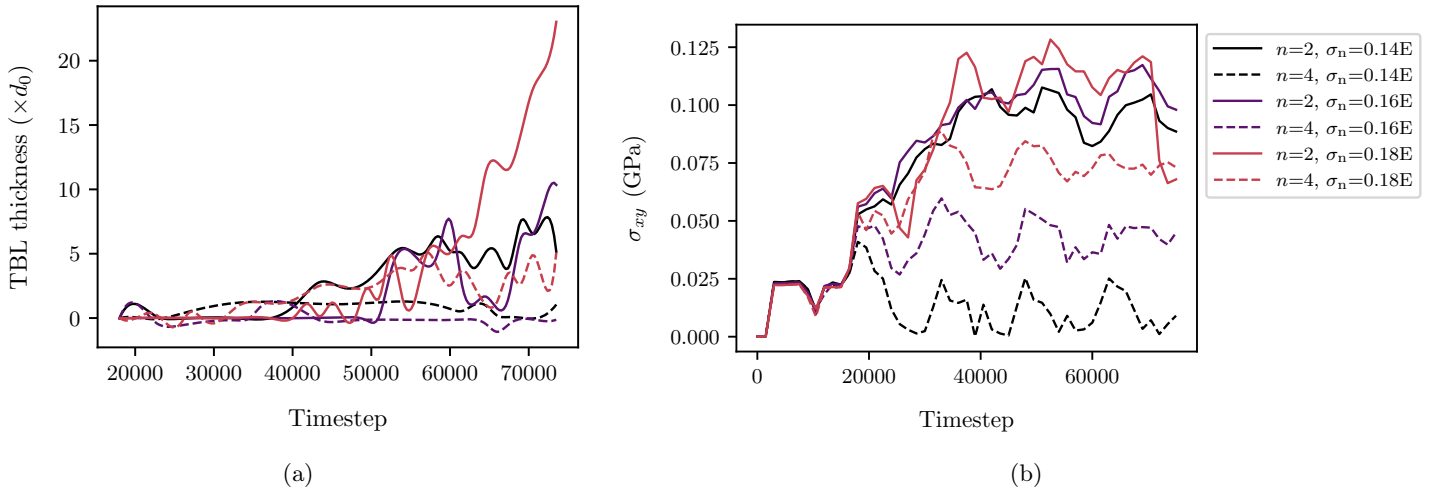
Figure 6.13: (a) represents the evolution of third-body layer (TBL) thickness, while (b) shows the evolution of shear stress σ_{xy}. Several tensile strengths are considered: $0.14E$, $0.16E$, and $0.18E$, along with either two or four elliptic rigid bodies.
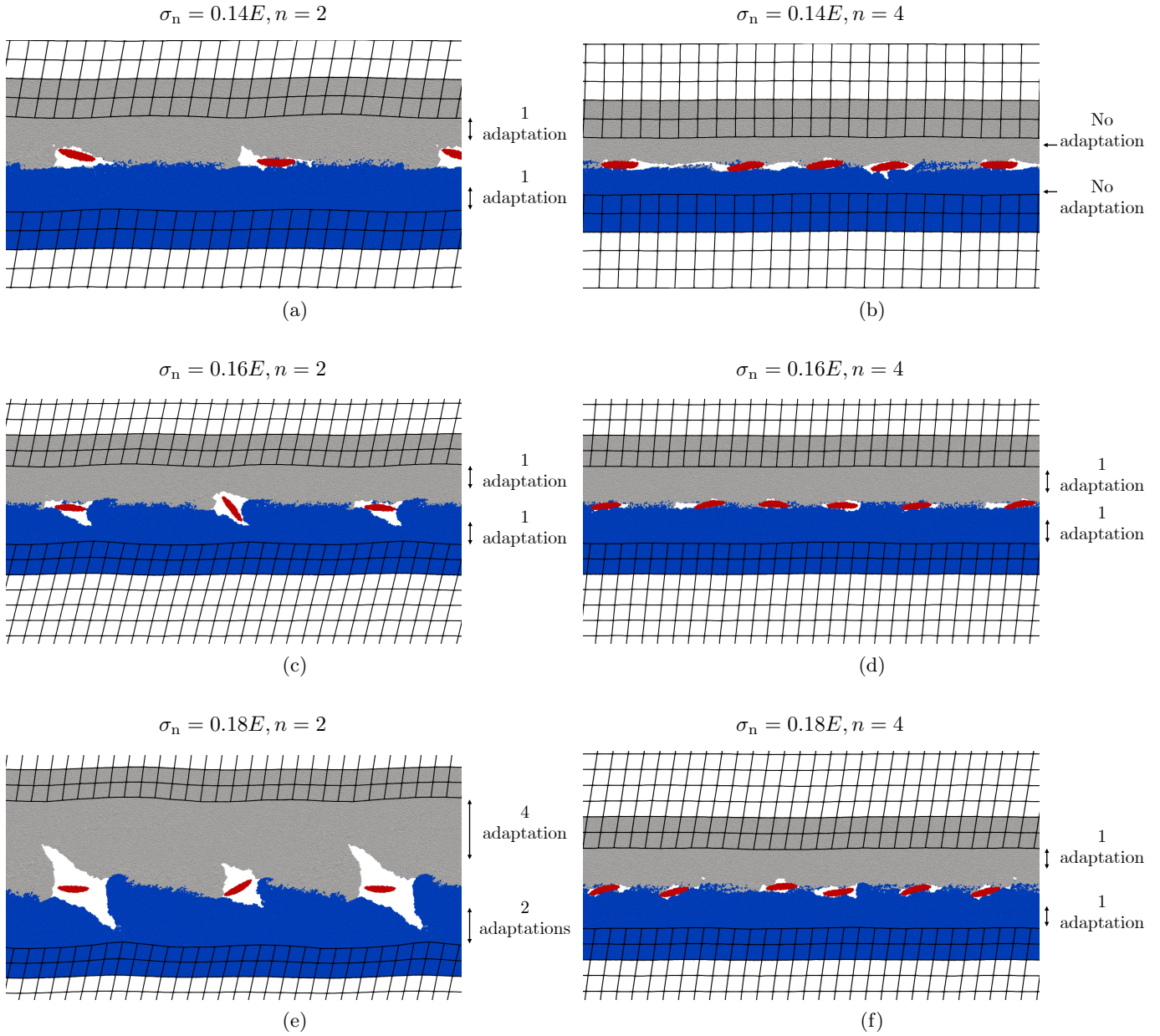
Figure 6.14: Final timestep of the coupled FEM-DEM system with elliptical rigid bodies at the interface. Continuum regions are displayed with a black grid. Top DEM particles are in gray, bottom DEM particles in blue, and elliptic rigid bodies are shown in red. Periodicity is replicated in the x direction for visualization purposes. (a) and (b) feature a tensile strength of $14E$, (c) and (d) exhibit a tensile strength of $16E$, while (e) and (f) present a tensile strength of $18E$. Configurations with two rigid bodies are depicted on the left, and those with four rigid bodies are shown on the right.

$$\sigma_{\mathrm{n}} = 0.18E, n = 4$$

(a)
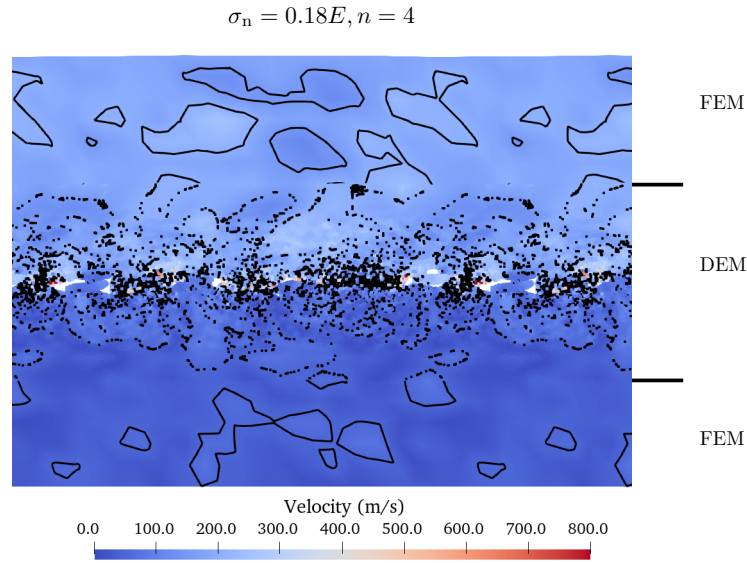
Figure 6.15: Velocity field at the final timestep of the coupled FEM-DEM simulation with elliptical rigid bodies at the interface, with a tensile strength of $0.18E$ and four rigid bodies. Black isolines depict the velocity field, while vertical black lines mark the distinction between continuum and discrete regions. To enhance visualization, periodicity is replicated in the x direction.

6.5   Conclusion

We developed an adaptive Finite Element Method-Discrete Element Method (FEM-DEM) coupling approach that enables the discrete region to dynamically expand in response to third-body deformation. This coupling employs the bridging method, initially designed for regular lattices and extended to amorphous materials as detailed in Chapters 4 and 5. Expansion of the discrete region occurs when severe deformation happens near the bridging zone. To determine whether the discrete region should be expanded, a criterion based on the changes of the per-particle neighborhood is computed within a detection zone placed ahead of the bridging region.

If the criterion is met, the boundary, bridging, and detection regions shift by a distance equal to the size of an FE element. Following this, new particles are introduced from a predefined DEM/MD box. In a next step, the coupling is re-initialized with these updated geometries. The FEM's displacement is then projected onto the newly inserted particles to account for the continuum deformation. FE elements transitioning to the discrete state are visually disabled, and their displacement is constrained by the discrete region. Subsequently, a relaxation process is carried out for the particles in the

new detection and bridging regions. Finally, the FEM's velocity is projected onto the particles in the new detection and bridging regions.

This adaptive coupling approach has been tested on an amorphous material (DEM) with an initial junction introduced to facilitate wear formation. Three cases were studied: a non-adaptive coupling with a small DEM, an adaptive coupling with an initially small DEM, and an adaptive coupling with an initially large DEM. In non-adaptive coupling, cracks were arrested in the bridging region, leading to invalid mechanical behavior. This demonstrated the necessity and accuracy of the proposed adaptive coupling approach. Additionally, the adaptive coupling was tested while coupling an aluminum crystal in classical MD. But using a different adaptation criterion it was possible to follow dislocation propagations.

Finally, the study considering the introduction of elliptic rigid bodies at the DEM interface reveals that both the number of rigid bodies and the material's tensile strength impact the evolution of third-body thickness and friction. As expected, the friction was lower for four rigid bodies than for two.

Chapter 7

Conclusion

7.1 Summary

The objective of this thesis was to develop a numerical tool to model the evolution of the third-body, including crack propagation and wear formation.

In chapter 3 we examined how boundary conditions and their proximity to the contact interface influence the evolution of the third-body. Pure Discrete Element Method (DEM) simulations were conducted, considering both force and displacement control boundary conditions. By adjusting the material properties of the DEM, we modeled various gouge regimes to explore their evolution in response to different boundary conditions and system heights. We demonstrated that both the boundary conditions and their proximity to the contact interface affect the third-body evolution. We also examined the displacement and stress at the border of a smaller domain within a larger one. Our findings indicated that applying the boundary conditions of the larger domain to the smaller domain does not adequately capture the complexity observed at the border. Thus, based on chapter 3 results, we concluded that there is a need to model the regions surrounding the third-body.

In chapter 4, we investigated the use of a FEM-DEM coupling to reduce computational costs: The DEM is utilized to model regions requiring particle discretization, while the surrounding areas, which remain linearly elastic, are modeled as a continuum using FEM. We extended the bridging method, originally developed for Molecular Dynamics (MD), to granular materials. While the original bridging method employed a strong formulation for coupling, we investigated both strong and weak formulations for granular materials. In all chapters of this thesis that discuss coupling, both the FEM and DEM domains represent the same material. A non-cohesive granular material was considered, with Hertzian contact between particles. We determined the minimum DEM sample size that ensure constant macroscopic properties. This establishes the minimum mesh size and the properties to be used in the FEM to ensure a match in material properties between the continuum and the discrete domains. Because the DEM has no cohesion, pre-stress needs to be introduced into the FE elements, resulting in spurious

113

forces. Correcting for these spurious forces improves the coupling stability. Hence, it was demonstrated that a strong coupling with subtraction of initial forces at the interface, exhibits superior stability. This coupling approach was validated via simulations featuring smooth wave propagation. While these setups can have many applications in geomechanics, where such particles are considered, modeling complex third-body evolution requires the inclusion of cohesion between particles. In a third part, we validated our coupling approach for modeling complex events such as crack propagation and wear formation, incorporating cohesion between particles. Coupled simulations were compared to pure DEM simulations, showing similar results but at a faster computational pace.

While this coupling method is efficient in many situations, it has a drawback: the evolution of the third-body is limited by the size of the discrete domain. To address this challenge, the last part of the thesis introduces an adaptive coupling method that allows the discrete domain to dynamically expand based on its deformation. This expansion happens when significant deformation occurs near the bridging region. To decide when to expand the domain, a criterion based on the average change of neighbors for each particle is implemented, in a detection region located ahead of the coupling region. A challenging aspect of this adaptive approach is the introduction of new particles.

The approach was tested using three models: a first model considering a small DEM region with a non-adaptive coupling, a second model considering a small DEM region with an adaptive coupling, and a third model featuring a large DEM region with an adaptive coupling. In the case of a small DEM domain with a non-adaptive coupling, a crack propagated in the bridging region, leading to unrealistic results, and emphasizing the importance of adaptivity. Additionally, the model with a small DEM domain and an adaptive coupling performs similarly to the one with a large DEM domain and an adaptive coupling, validating our adaptive strategy. This adaptive method was also applied to a Molecular Dynamics (MD) domain. Finally, this approach was used to investigate the impact of elliptical rigid bodies on the evolution of third-body thickness and frictional properties. As expected, if enough rigid bodies are introduced at the interface, they behave as solid lubricant.

7.2 Perspectives

The main goal of this thesis was to develop an adaptive FEM-DEM coupling to model the evolution of third bodies. The following discussion centers on future work and perspectives.

While the code operates in three dimensions, the evolution of the third-body has primarily been studied in quasi-2D, with a minimal dimension along the third axis (only Chapter 4 addresses a true three-dimensional system). To enable modeling of larger domains, especially for a three-dimensional system, the code's parallelization needs to be implemented. The code LibMultiScale (LM) [10] realizes the coupling between the

discrete and continuum domains, using LAMMPS [89] for discrete domain calculations and Akantu [7] for the continuum domain calculations. Given that both LAMMPS and Akantu are already parallelized, making LM's parallelization functional should be achievable.

Brink et al. [22] demonstrated through MD simulations that the third-body evolves in unique ways in three dimensions. They showed how quasi-spherical particles grow from material detaching from the surfaces, leading to the formation of cylinders, that later bridge together.

Hence, one of the primary applications of our approach could be to investigate the evolution of the third-body in three dimensions. This exploration would allow us to understand how frictional properties and the third-body regime vary between 2D and 3D settings, and to determine if specific particle formations occur in 3D. Additionally, a parametric study could be conducted to explore variations in parameters, including the material properties of the third-body.

Several industrial applications can benefit from this methodology, such as machining. In machining, an important aspect is the cutting of the surface while sliding. The evolution of the microstructure of the surface, caused by sliding and cutting, has been studied using MD [103]; however, due to the high computational cost of MD, only small-scale studies are feasible. Using our FEM-DEM coupling, larger systems can be modeled with accurate boundary conditions that more closely resemble actual industrial processes. Additionally, the adaptivity of the method would allow crack propagation to be accurately captured and at a lower computational cost. Other applications, including the insertion of solid lubricants at the contact interface, could further extend the work presented in Chapter 6. Exploring various shapes and sizes of solid lubricants could be part of this investigation. Finally, applications relevant to the geomechanics community, such as gouge response to stick slip events, could be explored with specific loading conditions and material properties.

Chapter 7 – Conclusion

Bibliography

[1] S. Abe and K. Mair. "Effects of gouge fragment shape on fault friction: New 3D modelling results". In: *Geophysical Research Letters* (2009). DOI: `10.1029/2009GL040684`.

[2] R. Aghababaei, D. H. Warner, and J.-F. Molinari. "Critical length scale controls adhesive wear mechanisms". In: *Nature Communications* (2016). DOI: `10.1038/ncomms11816`.

[3] I. Agnolin and J.-N. Roux. "Internal states of model isotropic granular packings. I. Assembling process, geometry, and contact networks". In: *Physical Review E* (2007). DOI: `10.1103/PhysRevE.76.061302`.

[4] I. Agnolin and J.-N. Roux. "Internal states of model isotropic granular packings. II. Compression and pressure cycles". In: *Physical Review E* (2007). DOI: `10.1103/PhysRevE.76.061303`.

[5] I. Agnolin and J.-N. Roux. "Internal states of model isotropic granular packings. III. Elastic properties". In: *Physical Review E* (2007). DOI: `10.1103/PhysRevE.76.061304`.

[6] J. Ahrens, B. Geveci, and C. Law. *An End-User Tool for Large Data Visualization, Visualization Handbook*. Elsevier, 2005.

[7] *Akantu*. `https://gitlab.com/akantu/akantu`.

[8] M. P. Allen and D. J. Tildesley. *Computer Simulation of Liquids*. Oxford University Press, 2017.

[9] G. Amontons. "De la résistance causée dans les machines, tant par les frottemens des parties qui les composent, que par la roideur des cordes qu'on y emploie, et la manière de calculer l'un et l'autre". In: (1699).

[10] G. Anciaux. *LibMultiScale*. `https://gitlab.com/libmultiscale/libmultiscale`.

[11] G. Anciaux. "Simulation multi-échelles des solides par une approche couplée dynamique moléculaire/éléments finis. De la modélisation à la simulation haute performance." PhD thesis. Université Sciences et Technologies - Bordeaux I, 2007.

BIBLIOGRAPHY

[12] G. Anciaux and J.-F. Molinari. "Contact mechanics at the nanoscale, a 3D multi-scale approach". In: *International Journal for Numerical Methods in Engineering* (2009). DOI: `10.1002/nme.2590`.

[13] G. Anciaux, S. B. Ramisetti, and J. F. Molinari. "A finite temperature bridging domain method for MD-FE coupling and application to a contact problem". In: *Computer Methods in Applied Mechanics and Engineering* (2012). DOI: `10.1016/j.cma.2011.01.012`.

[14] G. Anciaux et al. "The Coupled Atomistic/Discrete-Dislocation method in 3d part I: Concept and algorithms". In: *Journal of the Mechanics and Physics of Solids* (2018-09). DOI: `10.1016/j.jmps.2018.05.004`.

[15] J. F. Archard. "Contact and Rubbing of Flat Surfaces". In: *Journal of Applied Physics* (1953). DOI: `10.1063/1.1721448`.

[16] B. Avci and P. Wriggers. "A DEM-FEM Coupling Approach for the Direct Numerical Simulation of 3D Particulate Flows". In: *Journal of Applied Mechanics* (2012). DOI: `10.1115/1.4005093`.

[17] T. Belytshcko and S. P. Xiao. "Coupling Methods for Continuum Model with Molecular Model". In: *International Journal for Multiscale Computational Engineering* (2003). DOI: `10.1615/IntJMultCompEng.v1.i1.100`.

[18] Y. Berthier. "Maurice Godet's Third Body". In: *Tribology Series*. Elsevier, 1996. DOI: `10.1016/S0167-8922(08)70766-1`.

[19] R. L. Biegel, C. G. Sammis, and J. H. Dieterich. "The frictional properties of a simulated gouge having a fractal particle distribution". In: *Journal of Structural Geology* (1989). DOI: `10.1016/0191-8141(89)90101-6`.

[20] O. Bouillanne et al. *Wear in Progress: How Third Body Flow Controls Surface Damage*. preprint. 2024. DOI: `10.21203/rs.3.rs-3890447/v1`.

[21] F. P. Bowden and D. Tabor. "The area of contact between stationary and moving surfaces". In: *Proceedings of the Royal Society of London. Series A. Mathematical and Physical Sciences* (19397). DOI: `10.1098/rspa.1939.0005`.

[22] T. Brink, L. Frérot, and J.-F. Molinari. "A parameter-free mechanistic model of the adhesive wear process of rough surfaces in sliding contact". In: *Journal of the Mechanics and Physics of Solids* (2021), p. 104238. DOI: `10.1016/j.jmps.2020.104238`.

[23] J. Q. Broughton et al. "Concurrent coupling of length scales: Methodology and application". In: *Physical Review B* (1999). DOI: `10.1103/PhysRevB.60.2391`.

[24] M. A. Chaudry et al. "A multiscale DEM–FEM coupled approach for the investigation of granules as crash-absorber in ship building". In: *Computational Particle Mechanics* (2022). DOI: `10.1007/s40571-021-00401-5`.

[25] P. Y. Chen et al. "Hybrid discrete-continuum modeling of shear localization in granular media". In: *Journal of the Mechanics and Physics of Solids* (2021). DOI: `10.1016/j.jmps.2021.104404`.

[26] H. Cheng et al. "Elastic wave propagation in dry granular media: Effects of probing characteristics and stress history". In: *International Journal of Solids and Structures* (2020-03). DOI: `10.1016/j.ijsolstr.2019.03.030`.

[27] J. Cho et al. "The coupled atomistic/discrete-dislocation method in 3d. Part III: Dynamics of hybrid dislocations". In: *Journal of the Mechanics and Physics of Solids* (2018). DOI: `10.1016/j.jmps.2018.05.005`.

[28] European Commission. "In-depth analysis in support on the commission communication COM(2018) 773". In: (2018).

[29] *compute stress/atom command — LAMMPS documentation*. URL: `https://docs.lammps.org/compute_stress_atom.html`.

[30] E. Cosserat and F. Cosserat. *Théorie des Corps Déformables*. Librairie Scientifique A. Hermann et Fils, 1909.

[31] C. A. Coulomb. "Théorie des machines simples, en ayant égard de leurs parties et de la roideur des cordages". In: (1785).

[32] P. A. Cundall and O. D. L. Strack. "A discrete numerical model for granular assemblies". In: *Géotechnique* (1979). DOI: `10.1680/geot.1979.29.1.47`.

[33] B.V Derjaguin, V.M Muller, and Yu.P Toporov. "Effect of contact deformations on the adhesion of particles". In: *Journal of Colloid and Interface Science* (1975). DOI: `10.1016/0021-9797(75)90018-1`.

[34] H. B. Dhia and G. Rateau. "The Arlequin method as a flexible engineering design tool". In: *International Journal for Numerical Methods in Engineering* (2005).

[35] J. Dieterich. "A constitutive law for rate of earthquake production and its application to earthquake clustering". In: *Journal of Geophysical Research: Solid Earth* (1994-02-10). DOI: `10.1029/93JB02581`.

[36] J. H. Dieterich. "Constitutive Properties of Faults With Simulated Gouge". In: *Geophysical Monograph Series*. American Geophysical Union, 1981. DOI: `10.1029/GM024p0103`.

[37] J. H. Dieterich. "Modeling of rock friction: 1. Experimental results and constitutive equations". In: *Journal of Geophysical Research: Solid Earth* (1979). DOI: `10.1029/JB084iB05p02161`.

[38] J. H. Dieterich. "Time-dependent friction and the mechanics of stick-slip". In: *Pure and applied geophysics* (1978). DOI: `10.1007/BF00876539`.

[39] P. J. Digby. "The Effective Elastic Moduli of Porous Granular Rocks". In: *Journal of Applied Mechanics* (1981-12-01). DOI: `10.1115/1.3157738`.

[40] S. N. Domenico. "Elastic properties of unconsolidated porous sand reservoirs".
      In: *Geophysics* (1977). DOI: 10.1190/1.1440797.

[41] O. Durán, N. P. Kruyt, and S. Luding. "Analysis of three-dimensional micro-
      mechanical strain formulations for granular materials: Evaluation of accuracy".
      In: *International Journal of Solids and Structures* (2010). DOI: 10.1016/j.
      ijsolstr.2009.09.035.

[42] O. Durán, N. P. Kruyt, and S. Luding. "Micro-mechanical analysis of deformation
      characteristics of three-dimensional granular materials". In: *International Journal
      of Solids and Structures* (2010). DOI: 10.1016/j.ijsolstr.2010.04.014.

[43] B. Ferdowsi and A. M. Rubin. "A Granular Physics-Based View of Fault Friction
      Experiments". In: *Journal of Geophysical Research: Solid Earth* (2020). DOI: 10.
      1029/2019JB019016.

[44] M. W. Finnis and J. E. Sinclair. "A simple empirical N-body potential for transi-
      tion metals". In: *Philosophical Magazine A* (1984). DOI: 10.1080/01418618408244210.

[45] L. Frérot et al. "Tamaas: a library for elastic-plastic contact of periodic rough
      surfaces". In: *Journal of Open Source Software* (2020). DOI: 10.21105/joss.
      02121.

[46] K. M. Frye and C. Marone. "The effect of particle dimensionality on Granular
      friction in laboratory shear zones". In: *Geophysical Research Letters* (2002). DOI:
      10.1029/2002GL015709.

[47] K. Gao et al. "Modeling of Stick-Slip Behavior in Sheared Granular Fault Gouge
      Using the Combined Finite-Discrete Element Method". In: *Journal of Geophysi-
      cal Research: Solid Earth* (2018). DOI: 10.1029/2018JB015668.

[48] M. Godet. "The third-body approach: A mechanical view of wear". In: *Wear*
      (1984). DOI: 10.1016/0043-1648(84)90025-5.

[49] M. Godet. "Third-bodies in tribology". In: *Wear* (1990). DOI: 10.1016/0043-
      1648(90)90070-Q.

[50] A. A. Griffith. "VI. The phenomena of rupture and flow in solids". In: *Philosoph-
      ical Transactions of the Royal Society of London. Series A, Containing Papers of
      a Mathematical or Physical Character* (1921). DOI: 10.1098/rsta.1921.0006.

[51] M. Hodapp et al. "Coupled atomistic/discrete dislocation method in 3D Part II:
      Validation of the method". In: *Journal of the Mechanics and Physics of Solids*
      (2018). DOI: 10.1016/j.jmps.2018.05.003.

[52] K. Holmberg and A. Erdemir. "Influence of tribology on global energy consump-
      tion, costs and emissions". In: *Friction* (2017). DOI: 10.1007/s40544-017-0183-
      5.

[53] I. M. Hutchings. "Leonardo da Vinci's studies of friction". In: *Wear* (2016). DOI:
      10.1016/j.wear.2016.04.019.

[54]   Y. Ida. "Cohesive force across the tip of a longitudinal-shear crack and Griffith's specific surface energy". In: *Journal of Geophysical Research* (1972-07-10). DOI: `10.1029/JB077i020p03796`.

[55]   I. Iordanoff et al. "A Review of Recent Approaches for Modeling Solid Third Bodies". In: *Journal of Tribology* (2002). DOI: `10.1115/1.1467632`.

[56]   R. Itoh and T. Hatano. "Geological implication of grain-size segregation in dense granular matter". In: *Philosophical Transactions of the Royal Society A: Mathematical, Physical and Engineering Sciences* (2019). DOI: `10.1098/rsta.2017.0390`.

[57]   K. L. Johnson. *Contact Mechanics*. Cambridge University Press, (1985). DOI: `10.1017/CBO9781139171731`.

[58]   K. L. Johnson, K. Kendall, and A. D. Robert. "Surface energy and the contact of elastic solids". In: *Proceedings of the Royal Society of London. A. Mathematical and Physical Sciences* (1971). DOI: `10.1098/rspa.1971.0141`.

[59]   H. P. Jost. "Tribology — Origin and future". In: *Wear* (1990). DOI: `10.1016/0043-1648(90)90068-L`.

[60]   H. A. Makse et al. "Granular packings: Nonlinear elasticity, sound propagation, and collective relaxation dynamics". In: *Physical Review E* (2004). DOI: `10.1103/PhysRevE.70.061302`.

[61]   H. A. Makse et al. "Why Effective Medium Theory Fails in Granular Materials". In: *Physical Review Letters* (1999). DOI: `10.1103/PhysRevLett.83.5070`.

[62]   C. Marone. "Laboratory-Derived Friction Laws and Their Application to Seismic Faulting". In: *Annual Review of Earth and Planetary Sciences* (1998). DOI: `10.1146/annurev.earth.26.1.643`.

[63]   E. Milanese et al. "Emergence of self-affine surfaces during adhesive wear". In: *Nature Communications* (2019). DOI: `10.1038/s41467-019-09127-8`.

[64]   R. E. Miller and E.B. Tadmor. "The Quasicontinuum Method: Overview, applications and current directions". In: *Journal of Computer-Aided Materials Design* (2002). DOI: `10.1023/A:1026098010127`.

[65]   R. D. Mindlin. "Compliance of Elastic Bodies in Contact". In: *Journal of Applied Mechanics* (1949). DOI: `10.1115/1.4009973`.

[66]   K. Mizoguchi et al. "Reconstruction of seismic faulting by high-velocity friction experiments: An example of the 1995 Kobe earthquake". In: *Geophysical Research Letters* (2007). DOI: `10.1029/2006GL027931`.

[67]   G. Mollon. "A multibody meshfree strategy for the simulation of highly deformable granular materials". In: *International Journal for Numerical Methods in Engineering* (2016). DOI: `10.1002/nme.5258`.

[68] G. Mollon. "A unified numerical framework for rigid and compliant granular materials". In: *Computational Particle Mechanics* (2018). DOI: 10.1007/s40571-018-0187-6.

[69] G. Mollon. "Mixtures of hard and soft grains: micromechanical behavior at large strains". In: *Granular Matter* (2018). DOI: 10.1007/s10035-018-0812-3.

[70] G. Mollon. "Solid Flow Regimes Within Dry Sliding Contacts". In: *Tribology Letters* (2019). DOI: 10.1007/s11249-019-1233-0.

[71] G. Mollon. "The soft discrete element method". In: *Granular Matter* (2021). DOI: 10.1007/s10035-021-01172-9.

[72] N. H.T. Nguyen, H. H. Bui, and G. D. Nguyen. "An approach to calculating large strain accumulation for discrete element simulations of granular media". In: *International Journal for Numerical and Analytical Methods in Geomechanics* (2020). DOI: 10.1002/nag.3076.

[73] M. Otsubo, C. O'Sullivan, and T. Shire. "Empirical assessment of the critical time increment in explicit particulate discrete element method simulations". In: *Computers and Geotechnics* (2017). DOI: 10.1016/j.compgeo.2016.12.022.

[74] S. Pham-Ba and J.-F. Molinari. "Creation and evolution of roughness on silica under unlubricated wear". In: *Wear* (2021). DOI: 10.1016/j.wear.2021.203648.

[75] S. Pham-Ba and J.-F. Molinari. "Role of Minimum Adhesive Wear Particle Size in Third-Body Layer Properties". In: *Tribology Letters* (2023). DOI: 10.1007/s11249-023-01772-x.

[76] S. Pham-Ba and J.F. Molinari. "Adhesive wear with a coarse-grained discrete element model". In: *Computer Methods in Applied Mechanics and Engineering* (2022). DOI: 10.1016/j.cma.2022.115124.

[77] M. Pica Ciamarra et al. "Statistics of slipping event sizes in granular seismic fault models". In: *Europhysics Letters* (2011). DOI: 10.1209/0295-5075/95/54002.

[78] E. Rabinowicz. "The least wear". In: *Wear* (). DOI: 10.1016/0043-1648(84)90031-0.

[79] E. Rabinowicz. "The Nature of the Static and Kinetic Coefficients of Friction". In: *Journal of Applied Physics* (1951-11-01). DOI: 10.1063/1.1699869.

[80] N. Ricker. "The form and nature of seismic waves and the structure of seismograms". In: *Geophysics* (1940). DOI: 10.1190/1.1441816.

[81] R. E. Rudd and J. Q. Broughton. "Coarse-grained molecular dynamics and the atomic limit of finite elements". In: *Physical Review B* (1998). DOI: 10.1103/PhysRevB.58.R5893.

[82] A.y Ruina. "Slip instability and state variable friction laws". In: *Journal of Geophysical Research: Solid Earth* (1983). DOI: 10.1029/JB088iB12p10359.

[83] M. P.J. Schöpfer et al. "The impact of porosity and crack density on the elasticity, strength and friction of cohesive granular materials: Insights from DEM modelling". In: *International Journal of Rock Mechanics and Mining Sciences* (2009). DOI: `10.1016/j.ijrmms.2008.03.009`.

[84] V. B. Shenoy et al. "An adaptive finite element approach to atomic-scale mechanics—the quasicontinuum method". In: *Journal of the Mechanics and Physics of Solids* (1999). DOI: `10.1016/S0022-5096(98)00051-9`.

[85] L.E. Shilkrot, R. E. Miller, and W. A. Curtin. "Multiscale plasticity modeling: coupled atomistics and discrete dislocation mechanics". In: (2004-04). DOI: `10.1016/j.jmps.2003.09.023`.

[86] E. Somfai et al. "Elastic wave propagation in confined granular systems". In: *Physical Review E* (2005-08-03). DOI: `10.1103/PhysRevE.72.021301`.

[87] A. Stukowski. "Visualization and analysis of atomistic simulation data with OVITO–the Open Visualization Tool". In: *Modelling and Simulation in Materials Science and Engineering* (2010). DOI: `10.1088/0965-0393/18/1/015012`.

[88] E. B. Tadmor, M. Ortiz, and R. Phillips. "Quasicontinuum analysis of defects in solids". In: *Philosophical Magazine A* (1996). DOI: `10.1080/01418619608243000`.

[89] A. P. Thompson et al. "LAMMPS - a flexible simulation tool for particle-based materials modeling at the atomic, meso, and continuum scales". In: *Computer Physics Communications* (2022). DOI: `10.1016/j.cpc.2021.108171`.

[90] P. Vashishta et al. "Interaction potential for SiO_2: A molecular-dynamics study of structural correlations". In: *Physical Review B* (1990). DOI: `10.1103/PhysRevB.41.12197`.

[91] M. Voisin-Leprince et al. "Finite element method–discrete element method bridging coupling for the modeling of gouge". In: *International Journal for Numerical Methods in Engineering* (2022). DOI: `10.1002/nme.7171`.

[92] K. Walton. "The effective elastic moduli of a random packing of spheres". In: *Journal of the Mechanics and Physics of Solids* (1987). DOI: `10.1016/0022-5096(87)90036-6`.

[93] C. Wang, D. Elsworth, and Y. Fang. "Ensemble Shear Strength, Stability, and Permeability of Mixed Mineralogy Fault Gouge Recovered From 3D Granular Models". In: *Journal of Geophysical Research: Solid Earth* (2019). DOI: `10.1029/2018JB016066`.

[94] C. Wellmann and P. Wriggers. "A two-scale model of granular materials". In: *Computer Methods in Applied Mechanics and Engineering* (2012). DOI: `10.1016/j.cma.2010.12.023`.

[95] M. Woldman et al. "Investigating the influence of sand particle properties on abrasive wear behaviour". In: *Wear* (). DOI: `10.1016/j.wear.2012.07.017`.

[96] J. Woodhouse, T. Putelat, and A. McKay. "Are there reliable constitutive laws for dynamic friction?" In: *Philosophical Transactions of the Royal Society A: Mathematical, Physical and Engineering Sciences* (2015-09-28). DOI: `10.1098/rsta.2014.0401`.

[97] S. P. Xiao and T. Belytschko. "A bridging domain method for coupling continua with molecular dynamics". In: *Computer Methods in Applied Mechanics and Engineering* (2004). DOI: `10.1016/j.cma.2003.12.053`.

[98] Y. Yue et al. "Hybrid grains: adaptive coupling of discrete and continuum simulations of granular media". In: *ACM Transactions on Graphics* (2019). DOI: `10.1145/3272127.3275095`.

[99] C. M. Zener. *Elasticity and anelasticity of metals*. Chicago: University of Chicago Press, 1948.

[100] B. Zhang and R. A. Regueiro. "On large deformation granular strain measures for generating stress–strain relations based upon three-dimensional discrete element simulations". In: *International Journal of Solids and Structures* (2015). DOI: `10.1016/j.ijsolstr.2015.04.012`.

[101] H. P. Zhang and H. A. Makse. "Jamming transition in emulsions and granular materials". In: *Physical Review E* (2005). DOI: `10.1103/PhysRevE.72.011301`.

[102] Y. Zhang, G. Mollon, and S. Descartes. "Significance of third body rheology in friction at a dry sliding interface observed by a multibody meshfree model: Influence of cohesion between particles". In: *Tribology International* (2020). DOI: `10.1016/j.triboint.2020.106188`.

[103] W. Zheng, J. Airao, and R. Aghababaei. "Phase transformation and incidental effects of metastable crystalline TiAlN on the material removal mechanism". In: *Mechanics of Materials* (2024), p. 104845. DOI: `10.1016/j.mechmat.2023.104845`.

Manon Voisin-Leprince

Curriculum Vitae

Computational Solid Mechanics Laboratory
Civil and Environmental Engineering
École Polytechnique Fédérale de Lausanne
CH-1015 Lausanne, Switzerland
voisinleprincemanon@gmail.com

EDUCATION

2019 – 2024 **Doctor of Philosophy (Ph.D.)**,
École Polytechnique Fédérale de Lausanne, Switzerland
Doctoral program in civil and environemental Engineering
Thesis: "Modeling friction and wear in granular media using an adaptive discrete-continuum bridging coupling"
Supervisor: Prof. Jean-François Molinari
Co-supervisor: Dr. Guillaume Anciaux

2018 – 2019 **Master of Science in Structural Engineering**
Northwestern University, Evanston IL, USA
Master thesis: "Elastic waves isolation in auxetic-honeycomb lattice: Tunable Mechanical Filter"
Supervisor: Oluwaseyi Balogun

2016 – 2019 **Master of Science in Civil Engineering**
École Spéciale des Travaux Publics, Paris, France

2014 – 2016 **Intensive Preparatory Scientific Classes for Engineering School**
Lycée Saint-Louis, Paris, France
Lycée Fénelon, Paris, France

RESEARCH EXPERIENCES

2019 – 2024 **Doctoral Assistant**
École Polytechnique Fédérale de Lausanne, Switzerland
- Studied friction and wear between interfaces
- Active developer of LibMultiscale, a C++ code for coupling discrete and continuum domains
- Numerically modeled third-body evolution through adaptive discrete-continuum coupling

2018 – 2019 **Master graduate student research**
Northwestern University, Evanston IL, USA
- Studied the behavior of auxetic materials to create a tunable mechanical filter

PUBLICATIONS

2024 **Two-scale concurrent simulations for crack propagation using FEM-DEM bridging coupling**
Manon Voisin-Leprince, Joaquin Garcia-Suarez, Guillaume Anciaux, Jean-François Molinari
Under Review

2022 **Finite element method–discrete element method bridging coupling for the modeling of gouge**
Manon Voisin-Leprince, Joaquin Garcia-Suarez, Guillaume Anciaux, Jean-François Molinari
International Journal for Numerical Methods in Engineering

CONFERENCES

2023   **U.S. National Congress on Computational Mechanics**, Albuquerque, USA
Talk: *Adaptive FEM-DEM Bridging Coupling*
<u>Manon Voisin-Leprince</u>, Guillaume Anciaux, Jean-François Molinari

2023   **European Geosciences Union**, Vienna, Austria
Talk: *Crack propagation and wear formation using a FEM/DEM bridging coupling*
<u>Manon Voisin-Leprince</u>, Joaquin Garcia-Suarez, Guillaume Anciaux, Jean-François Molinari

2022   **French Mechanical Congress - Congrès Français de Mécanique**, Nantes, France
Talk: *FEM/DEM coupling of gouge rock material*
Conference proceeding: *FEM/DEM coupling of gouge rock material*
<u>Manon Voisin-Leprince</u>, Joaquin Garcia-Suarez, Guillaume Anciaux, Jean-François Molinari

2022   **CMIS Symposium**, Chexbres, Switzerland
Attending

2021   **Particles 2021**, Hamburg, Germany
Talk: *FEM/DEM coupling of gouge rock material*
<u>Manon Voisin-Leprince</u>, Joaquin Garcia-Suarez, Guillaume Anciaux, Jean-François Molinari

Poster presentation

2024   **Doctoral Program in Civil and Environmental Engineering (EDCE) research day**, EPFL, Switzerland
Poster: *Boundary distance impact on third-body evolution using adaptive FEM-DEM bridging coupling*
<u>Manon Voisin-Leprince</u>, Jean-François Molinari, Guillaume Anciaux

Teaching Experiences

Fall 2021, 2022   **Scientific Programming for Engineers**, by *Dr. Guillaume Anciaux*
Teacher Assistant - Doctoral level class
- 14 weeks, responsible for 2 hours/week of exercise sessions and projects supervision, grading

Spring 2020, 2021, 2022   **Numerical Modeling of Solids and Structures**, by *Prof. Jean-François Molinari*
Teacher Assistant - Bachelor level class
- Introduction class to Finite Element Method
- 14 weeks, responsible for 2 hours/week of exercise sessions, project and, grading

Fall 2020   **Continuum Mechanics**, by *Prof. Jean-François Molinari*
Teacher Assistant - Bachelor level class
- 14 weeks, responsible for 2 hours/week of exercise sessions, grading

Supervised projects

2022   **Discrete Element Method (DEM) study of the interaction between a solid body and granular medium**
Master student: Noémie Riez - Semester project

2022   **Extension of granular material using machine learning**
Master student: Majoor Colin - Semester project

2022   **Classification of granular material**
Bachelor student: Felber Arnaud - Semester project

2022   **Development of a DEM simulation of the interaction between a shoe and soil**
Master student: Louis Jaques - Semester project

2020   **Dynamic fragmentation of a fragile ring**
Bachelor student: Zélie Beuchat - Semester project

2020   **Two-dimensional granular shear model**
Bachelor student: Jean Naftalski - Semester project